



DIPLOMARBEIT

3D-printed Mammography Image Quality Phantoms with Structured Backgrounds

Ausgeführt am

**Zentrum für Medizinische Physik und Biomedizinische Technik der
Medizinischen Universität Wien**

und am

Atominstitut der Technischen Universität Wien

Unter der Anleitung von

Ao. Univ.-Prof. Dipl.-Ing. Dr. Peter Homolka

durch

Aram Nikolaus Summhammer, BSc.

Matrikelnummer: 00852266

Wien, 06.02.2025

Unterschrift

Unterschrift des Betreuers

Erklärung zur Verfassung der Arbeit

Aram Nikolaus Summhammer

„Hiermit erkläre ich, dass ich diese Arbeit selbständig verfasst habe, dass ich die verwendeten Quellen und Hilfsmittel vollständig angegeben habe und dass ich die Stellen der Arbeit – einschließlich Tabellen, Karten und Abbildungen – die anderen Werken oder dem Internet im Wortlaut oder dem Sinn nach entnommen sind, auf jeden Fall unter Angabe der Quelle als Entlehnung kenntlich gemacht habe.“

Wien, 06.02.2025

Acknowledgment

An dieser Stelle möchte ich meinem Betreuer, Ao.Univ.-Prof. Dipl.-Ing. Peter Homolka für die freundliche Unterstützung im Rahmen der gesamten Diplomarbeit danken. Er half mir dabei die wesentlichen physikalischen Zusammenhänge und Prinzipien für den grundsätzlichen Entwurf und die Umsetzung von Design zu finalisiertem Druck im Rahmen meiner Arbeit zu verstehen. Weiters möchte ich meinen Kollegen Lukas Zalka MSc., sowie Thomas Hofmann BSc. für die tatkräftige Unterstützung bei meinen Experimenten, insbesondere beim 3D-Druck, danken. Sie gaben mir gute Ratschläge und waren immer zu Stelle, wenn ich eine helfende Hand benötigte.

Ebenso möchte ich meinem guten Freund Martin Hatlak danken, welcher mir mit seiner chemischen Expertise und kreativen Einfällen den einen oder anderen Denkanstoß gab.

Zu guter Letzt möchte ich meiner Familie danken, welche mir durch Liebe und Zuspruch während meiner Odyssee immer den Rücken stärkte.

Contents

Motivation	7
1 Introduction	9
1.1 Medical applications of 3D printing	9
1.2 Phantoms in diagnostic imaging	12
1.3 X-ray imaging of the breast	17
1.3.1 2D Mammography	20
1.3.2 Digital Breast Tomosynthesis (DBT)	21
1.3.3 Contrast Enhanced Dual Energy Mammography (CEDEM)	22
1.3.4 Clinical Relevance	22
1.4 Mammography phantoms	23
1.4.1 Commercially available phantoms for breast imaging	23
1.4.2 Recent developments and state of the art in mammography phantom research	25
2 Materials and Methods	34
2.1 Phantom designs	34
2.1.1 Three component basic model - CBM	34
2.1.2 Phantom 45	42
2.1.3 Phantom 45 Dual Extrusion Alternative Design	49
2.2 3D printers and printing materials	50
2.2.1 Ultimaker S3	52
2.2.2 FLSUN V400	52
2.2.3 Saturn 4 Ultra by Elegoo	53
2.2.4 3D Printing & Slab Filling Materials	53
2.2.5 FDM Printing Parameters and Instructions	56
2.2.6 SLA Printing Parameters	63

2.3	Filling process	63
2.4	Visualisation and Projection tools	65
2.5	Imaging systems and settings.....	66
3	Results.....	68
3.1	Printing & Filling Results	68
3.1.1	CBM Phantom Slabs	68
3.1.2	Phantom 45 Slabs	70
3.2	Design & Imaging Results.....	73
3.2.1	CBM Phantom Images.....	73
3.2.1	Phantom 45 Images	82
4	Discussion.....	89
5	References	99

Abstract

In this technical feasibility thesis, two concept designs of 3D-printed mammography phantoms for Full Field Digital Mammography (FFDM) and Digital Breast Tomosynthesis (DBT) are presented. Each assembled phantom consists of individual anthropomorphic plates that simulate anatomic noise during imaging. Both phantoms were designed with the CAD software Fusion by Autodesk [1] and Blender 4.2 [2], and realized via Fused Deposition Modelling (FDM). Concept #1, the *three component basic model* (CBM), consists of three equally thick plates, printed with Poly-Lactic-Acid (PLA) filament. When assembled they resemble a compressed breast during mammography. Each of the plates holds a complicated 3D finely branched tubular inside structure that is supposed to imitate the glandular ducts in the parenchymal tissue. The intermediate space is filled with an adipose-tissue imitating material (coconut oil), that has a linear attenuation for X-rays at the common mammography spectra similar to adipose tissue. The CBM phantom is applicable for FFDM and DBT. Concept #2, *Phantom 45*, simulating a 45mm thick compressed breast, is based on an 8bit orthographic projection of an artificial duct system. The pixel values of the orthographic projection image were used to elevate individual elements of a 101x101 mesh plane in Blender, resulting in a height profile, that resembles the artificial duct system when imaged in 2D Mammography. Phantom 45 was printed with Polyethylen-terephthalat-glycol (PETG). The intermediate space material is pure paraffin wax, also imitating adipose tissue at the common mammography spectra. Phantom 45 is applicable for FFDM only. Both assembled phantoms and the individual plates have been imaged at 27kVp (CBM), and 28kVp (Phantom45) on a Siemens Healthcare [3] Mammomat Revelation (W/Rh). Further a DBT was conducted on the CBM Phantom at 28kVp. The resulting 2D mammography images and reconstructed DBT slices were visually compared to the CAD design renderings and their respective orthographic projection, with focus on pattern-matching and contrast distinction between the used materials. The inside structures of all individual plates were clearly identifiable, including fine features. The assembled CBM FFDM and DBT images could not be compared visually due to the complex anthropomorphic inside structure, and need to be evaluated further with Imaging Software.

Phantom 45 showed some printing-related plate issues with PETG, but was overall also of high quality in terms of pattern matching and contrast distinction. In conclusion both design concepts, and the realization via FDM, represent a combination of existing 3D-printed imaging phantom approaches and new implementation ideas for even more realistic phantoms.

Motivation

During routine examinations as part of breast cancer screenings, mammography machines need to acquire very small and fine details in terms of both, small density differences as well as fine structures like microcalcifications in the female breast tissue. For this reason, the imaging capabilities of the mammography machines have to be checked constantly to assure a proper image quality considering spatial resolution, contrast, Contrast-Noise-Ratio (CNR) and several other imaging parameters. Quality analysis is an essential part of assuring a high detection rate of potential malignancies at an early stage.

Scope

The initial project idea for this thesis was to create a 3D-printed Contrast Enhanced Dual Energy Mammography (CEDEM) phantom with interchangeable anthropomorphic plates, by which one can vary the phantom thickness and hence also alter the resulting anatomic noise. Additionally, a central structure plate, with mounted iodinated platelets of different concentrations, could be inserted at an arbitrary height between the anthropomorphic plates. Two FFDM images, and potentially DBT image-sets, at two energies below and above the K-Edge of iodine (33,2 keV) would be acquired and an iodine image generated. Over the course of the first 3D-printing experiments, the scope of the thesis changed towards a feasibility study on the realization of different phantom design concepts. Concept #1 follows the approach of manufacturing an assembled phantom prototype of three 3D-printed plates, which simulate a compressed breast during mammography. The inside of the plates would consist of structures that simulate the anatomic noise from parenchymal breast tissue, especially the glandular duct system. The intermediate space would be filled with some adipose-tissue imitating material. Concept #2 would follow a similar approach, but convert the inner structure design to a height profile, spread over two anthropomorphic plates with only a thin structure plate in the middle. This structure plate would be the remaining element from the initial thesis idea, by being able to theoretically mount platelets containing defined iodine concentrations. After 3D-printing the

assembled phantoms and their individual plates would be imaged and compared to an orthographic projection of the initial CAD designs.

1 Introduction

1.1 Medical applications of 3D-printing

The amount of 3D-printing related design possibilities for technical devices in engineering disciplines are manifold and the medical sector is no exception to it. From simple applications such as medical aids, implants made of flexible polymers, up to the reconstruction of amputated body parts and the growth of new (artificial) tissue - 3D-printing has long become a standard CAM (computer assisted manufacturing) method in modern medicine. A broken arm for instance with an uncomplicated fissure is usually treated with a heavy white cast, made out of wet, $\text{CaSO}_4 \cdot 2\text{H}_2\text{O}$ saturated cloth-strips, which harden out to stabilize the arm, and can be a nuisance in terms of overall body mobility, itches and body hygiene. The *Osteoid* [4] designed by Deniz Karasahin or the *Cortex* [5] by Jake Evill, both exhibit a 3D-printed low weight cast with natural ventilation via an elegant honeycomb design and dismisses water and humidity issues of traditional cast materials. In case of the Osteoid, which was printed via *fused deposition modelling* (FDM) with ABS¹ material, an additional healing accelerating feature is implemented: LIPUS (Low Intensity Pulsed Ultrasound), which causes tissue growth stimulation by ultrasound [6]. Rather than using thermoplastic filaments in fused deposition modelling (FDM) or viscous resins in stereo lithography (SLA), 3D-bioprinting on the other hand makes use of biological materials in order to reproduce the complex micro architecture of extra cellular matrix (ECM) components. Here the resolution is of utmost importance to recapitulate biological function. 3D-bioprinting consists of three main design techniques: *Biomimicry* – the approach to copy and reproduce the cellular and extracellular tissue or organ components on a micro scale; *Autonomous self-assembly* – the indirect approach of setting optimal conditions for self-assembling tissue spheroids guided by embryonic organ

¹ Acrylonitrile butadiene styrene – common FDM printing material

development; and *Mini-tissues* – functional building blocks representing the smallest tissue unit, which in larger number comprise a bigger organ, e.g. Nephrons are the smallest blood-filtering unit in the kidney and can be described as a mini tissue in that regard. As of now, successfully bio-printed tissues types and organs include skin tissue, cartilage and an early stage kidney prototype [7]. Delicate surgery procedures can require placed implants to be absorbed or have enough flexibility to adjust to the surrounding tissue after implantation. Zopf et al. [8] created a 3D-printed biodegradable airway splint made out of polycaprolactone to stabilize a fragile airway passage (left bronchus) in a 2 month old new-born with Tracheobronchomalacia. A key design feature was the flexibility of the splint material, allowing extension, flexion and expansion with the natural surrounding tissue growth. A similar approach is taken in the field of breast reconstruction. After full or partial mastectomy, 3D (bio)-printing can aid in surgical planning and help to improve the reconstructed tissue quality in terms of symmetry and realistic appearance. Common methods are the use of autologous tissue – mainly adipose tissue, taken from the abdomen, providing a more natural look, or common breast implants, which are usually immediately inserted in case of full mastectomy. 3D-imaging provides the basis for such custom implant designs, which are planned and realized via CAD and CAM, and can further aid in surgical planning for transplanting autologous tissue, e.g.: custom 3D-printed breast molds aid inter-operatively to form the flap for the *deep inferior epigastric artery perforator (DIEP) flap* procedure, which is a common method in breast reconstruction [9]. Surgical planning in general and extensive medical training are essential to uphold high medical standards. Through 3D-printing it is possible to create a life-size physical heart model and other cardiovascular models of real patients, with volumetric data acquired by CT. Compared to mere digital organ analysis via computer model reconstruction, this allows for a hands-on detailed inspection of individual life-size anatomy and pathologies, or conducting implant experiments on models e.g.: stents. The printing material can be tissue-similar in terms of density, topology, elasticity or attenuation coefficient – depending on what the specific demands are. These models are also used for training new inexperienced medical staff. A life-size physical model helps to understand spatial dimensions of pathological shapes and can pose as a practice object for cardiovascular related interventions. Imaging-wise, real patient models can further aid in

the adjustment of CT settings to reduce patient dose [10, 11]. Wu et al. [12] used a realistic 3D-printed aortic model with an inserted thoracic stent to assess the optimal CT scanning parameters for post-surgery Thoracic endovascular aortic repair (TEVAR) patients. Post-surgery CT surveillance scans with TEVAR patients come with a high dosage, which can cause radiation induced malignancy. Several scans with different pitch and kVp combinations on the 3D-printed aortic model showed a promising possibility to reduce the applied patient dose at a high pitch with 100kVp without losing significant image quality. Apart from dosimetry considerations, image quality control is an essential component to assure proper diagnostic imaging procedures and maintain high quality standards. Taking a closer look at imaging related applications, the field of 3D-printed imaging phantoms for dosimetry and image quality control purposes has had several publications in the recent years focusing on new designs and printing materials [13]. Compared to CNC machining methods of drilling, turning or laser cutting, the elegant additive nature of 3D-printing poses as a simple and cost effective way to manufacture custom-tailored phantoms for a specific modality [14]. Regarding 3D-printing materials, a lot of research and experiments revolve around finding fitting phantom material compositions to mimic and simulate different tissue types with respect to their physical properties, e.g. linear attenuation in X-ray related modalities [15].

1.2 Phantoms in diagnostic imaging

The American National Institute of Standards and Technology (NIST) [16] defines medical imaging phantoms as: “...objects used as stand-ins for human tissues to ensure that systems and methods for imaging the human body are operating correctly [17].” This clearly points out the requirement of having a proper reference tool to maintain a high image quality with the respective imaging modality. The clinical staff is dependent on proper phantoms for calibration and quality control, since the resulting images have to provide a reliable basis to evaluate patient conditions and plan further medical procedures accordingly. This subchapter will give a short overview about the physics and technical background of the common modalities in medical imaging and describe the phantom characteristics with a couple of examples.

MRI – Magnetic Resonance Imaging: MRI is predominantly used to image soft tissues and liquids like tendons, muscles, the knee, torso or the brain. MRI phantoms are usually in cylindrical (e.g. abdomen) or spherical (e.g. head) shape and have a circular or ellipsoidal outline [18]. The shell material needs to be free of susceptibility effects or signal disruption. Common materials are: Perspex, acrylic, nylon or polystyrene. These materials produce little susceptibility effects at water/material interfaces. Fluid additives like CaSO_4 modify the relaxation time and can reduce the temperature dependency of relaxation times. Besides spatial resolution, low-contrast detectability, geometric distortion, image uniformity, slice thickness accuracy, and signal-to-noise ratio are relevant imaging parameters that need to be evaluated. The *American College of Radiology Accreditation (ACR)* [19] Large Phantom is a popular MRI phantom representative. It consists of a hollow cylinder (190x148mm) representing a typical head size. The shell is of acrylic. The tissue specific mimicked relaxation times T1 and T2 are imitated via a 10mM NiCl + 75 mM NaCl solution. Other common MRI phantoms are the NIST MRI Phantom [20] and the Alzheimer’s Disease Neuroimaging Initiative Phantom [21].

Nuclear Medicine, SPECT and PET Phantoms: Due to the radioactive nature of the PET & SPECT modalities, many imitating approaches are implemented via mathematical (software) phantoms, especially for dosimetry aspects, but also for evaluating image reconstruction

algorithms [18]. However some physical models do exist for image quality control. Mathematical models for image reconstruction and processing require a higher amount of anatomic realism compared to models for internal dosimetry, which are usually comprised of simple geometric shapes. These come with sharp interfacial boundaries, a rather unrealistic assumption about organs in the human body. Further anthropomorphic models require a co-registration of a tissue attenuation map (transmission data), together with a radiopharmaceutical distribution in order to simulate emission tomography accordingly (emission data). The *Mathematical Cardiac Torso phantom* (MCAT) was among the first software packages capable of generating dual emission & transmission datasets. It is a refined version of the internal dosimetry phantom MIRD by the Society of Nuclear Medicine's *Medical Internal Radiation Dose* Committee [22]. The XCAT (*4D extended cardiac-torso*) phantom represents an even further advanced version with a serious increase in anatomic detail. While the MCAT only exhibits a couple of individual structures, the XCAT includes over 9000 geometrical shapes to mimic the human anatomy [23]. Compared to the complexity of mathematical models, physical models are of simple design. Physical PET phantoms are comprised of a hollow chamber (e.g. cylinder) filled with water or a different liquid. This fluid contains some uniformly dispersed radioactive material which enables a precise quantification of radioactivity. Spatial resolution, count sensitivity and the scatter fraction are among the relevant parameters that can be evaluated with a physical PET phantom. Physical SPECT phantoms are of similar design and usually have rod and spherical inserts to test for spatial resolution, contrast and uniformity. The *Jaszczak Phantom* is a prominent example for quality assurance in PET/SPECT for these parameters [24]. It is quite common that the same basic design can be used for PET and SPECT testing, with only small adjustments like exchanging the specific radioactive agent (F18/Tc99m). The *NEMA IEC Image quality phantom* (PET) [25] or *Dynamic Heart Phantoms* are other popular representatives of physical PET/SPECT phantoms for quality assurance. The latter is able to mimic the myocardial perfusion of a beating heart with specific chambers for myocardium and ventricular cavities and the option to simulate perfusion defects.

Ultrasound Phantoms: Ultrasound (US) phantoms simulate tissue properties for the propagation of sound waves in the frequency range of 2-12Mhz for calibration, quality control

and medical training [26]. Modern phantoms incorporate gelatine, agarose or urethane-based materials to mimic soft tissue, while older models were based on water. The key parameters of a US phantom are speed of sound, attenuation and backscatter and are met accordingly in the phantom design. Certain layers or desired shapes with alternating densities can be included to assess depth calibration, spatial resolution and uniformity. US phantoms are available in various compositions, simple or anthropomorphic shapes and various optional tools depending on the intended use. US phantoms are made of different materials to imitate variable tissue density, usually Acrylnitril-Butadien-Styrol (ABS) as a shell material and various anatomic shapes for routine medical tests. The amount of available US phantoms and gadgets shows quite the increase in popularity of this non-invasive imaging modality.

Conventional X-ray: The main characteristics of X-ray phantoms include their material for imitating the correct tissue attenuation and the anatomical design for realistic photon pathlengths and tissue type distribution [18]. Polymethyl methacrylate (PMMA), polyethylene and epoxy resins are among the common phantom materials for soft tissues, while calcium-based compounds are used for bone-like structures. Many conventional X-ray phantoms for diagnostic imaging have anthropomorphic design for the respective body part, which can include water or other liquids. Insertable parts like dosimeters or pathology resembling objects are common in modular phantoms which can be (dis-)assembled to feature the desired anatomy. Leeds Test Objects [27] is a popular producer of phantoms for all common modalities and features a variety of simple and advanced conventional X-ray phantoms. *TOR CDR* [28] is a circular test object for regular imaging performance tests, which includes a grayscale check and the detectability of very fine features like bar patterns for resolution and contrast checks. The *Lungman chest phantom* is a great example for an anthropomorphic thorax phantom for conventional X-ray and CT. It consists of PMMA shell material, can be disassembled and features a very fine bronchial and rib structure [29].

Computer Tomography: Considering phantom material aspects, CT has similar requirements compared to conventional X-ray. PMMA, epoxy resin or water equivalent compounds usually mimic the respective human tissue. As described in the prior modality phantoms, calibration phantoms are mostly of simple design and focus on standardized features to evaluate specific

system parameters. The *Catphan Phantom* [30] is a common candidate for regular quality control. It tests for spatial resolution, slice thickness, uniformity and low contrast detectability. The *NEMA IEC Image quality phantom* [25] described in PET is an excellent calibration model for the combined modality of PET/CT. Considering anthropomorphic phantoms, the *Alderson RANDO Phantom* [31], made of tissue equivalent resin, provides very detailed dosimetry evaluation for internal organs and imaging quality in clinical scenarios. The *CIRS Dynamic Thorax Phantom* [32] incorporates moving parts which replicate respiratory motion, which is ideal to test for motion artifacts which occur during lung and cardiac imaging. Especially the Alderson RANDO Phantom proves an excellent training dummy for medical training due to its very realistic design [33].

Phantom Evaluation Methods: For phantom evaluation both, human readers and automated systems are used. With the increasing capabilities of modern AI systems the latter method gains importance, yet human readers still play a central role in interpreting phantom measurements. Specifically in qualitative assessments such as artifact identification (including the question: is the analysed object even an artifact?), together with contrast and spatial resolution. Both subtle and complex image features might still be missed by Model Observers/AI, or worse: rendered away due to misclassification. However a human reader will experience fatigue, leading to errors, and has variability in terms of subjective interpretation coupled with experience. When examining several images in a row this could lead to a personal bias, due to e.g. certain features, details or pattern recognition the reader noticed in an evaluated image, and unconsciously keeps looking for in future images from an image-dataset. With the increasing amount of data, the element of time consumption and human resource per se is an issue to be pointed out. Automated read outs on the other hand provide an objective reproducible alternative for the main parameters as Signal to noise ratio (SNR), spatial resolution, or dose uniformity. A machine does not get tired, and is able to perform pattern-comparison, image registration processes and other evaluation methods, all simultaneously in a blink of an eye. In automated read outs, so called *Model Observers* are mathematical systems which simulate the human visual system to assess imaging performance. Ideal Observer or *Channelized Hotelling Observer* (CHO) are two models which help to define the maximum performance of an imaging system

and can incorporate realistic limitations like noise and reduced resolution. They are applicable for CT/MRI/PET/SPECT. The results of such observer models are cross correlated with the human observer results [34].

1.3 X-ray imaging of the breast

Compared to other radiographic modalities in medicine, mammography is one of the most technically demanding imaging methods, since it has to combine a high spatial resolution with low radiation dose and a very fine tissue contrast (ALARA² principle). Contrast in particular can prove a challenge, because the attenuation coefficients of fibro-glandular tissue and cancerous breast tissue are very similar (especially in dense breasts), bearing the risk of potential malignant structures to be overlooked. This chapter will give a short overview about the technical and medical background of 2D mammography, such as screen-film mammography (SFM), digital mammography (DM) and contrast enhanced spectral mammography (CESM), as well as 3D digital breast tomosynthesis (DBT).

General components of a mammography system [35]: X-ray tube with a rotating anode paired with a filter for soft tissue imaging. The anode (source of the generated photons, also called *target*) and filter combination are abbreviated as e.g.: Mo (anode material)/Rh (filter material). Common combinations are: [Mo/Mo, Mo/Rh, Rh/Rh, W/Rh, W/Ag, W/Al]³. The filter is necessary to cut off the hard X-ray beams, because due to the breast being composed of very low density tissues (mainly adipose tissue and glandular tissue), soft radiation spectra are required to get a good contrast between tissues of similar density. While Mo/Mo combination is the common setup for a compressed breast thickness of <5cm, Mo/Rh or Rh/Rh (depending on the manufacturer) is the choice for thicker and denser breast tissue. Common kVp values for Mo targets are between 24-32kVp, Rh and W are usually operated with 26-35kVp (peak Voltage – limiting the maximum photon energy produced by the X-ray tube). The final radiation field is always rectangular to match the image receptor.

² As low as reasonably achievable

³ Mo(Molybdenum),Rh(Rhodium),W(Tungsten),Al(Aluminium),Ag(Silver)

A compression plate is used for flattening out the breast to reduce the organ thickness and provide an (almost) constant thickness over the whole organ to reduce the dynamic range. Spreading out the fibro glandular tissue reduces scatter and makes potential malignant structures (cancer) more visible and distinguishable from superimposed structured noise, created by the surrounding breast tissue. Additionally, it saves exposure time (hence dose) and gives a sharper image overall due to less patient motion. The AGD (average glandular dose) per *shot* (=measurement) is about <2 to 3mGy for an average compressed breast (~45mm thickness), giving about 4mGy in total since the common imaging procedure in 2D mammography mostly consists of 2 *standard views*, meaning: CC (*cranial caudal* – top/bottom view) and a MLO (*medio lateral oblique* - side view, from the chest to the side).

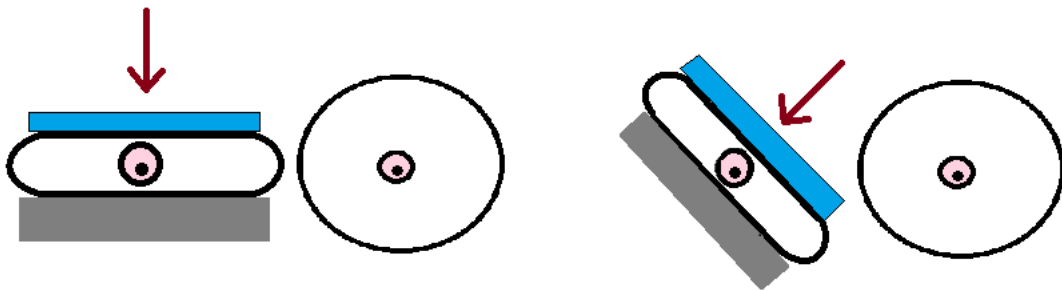


Figure 1: Schematic breast compression for standard views. **Left:** CC view. **Right:** MLO view.

As shown in Figure 1 these two views are not orthogonal. Common *Supplementary views* are SL (straight lateral – 90° to CC or MLO view), *rolled CC* (CC view but with medial or lateral rotation around the axis going through the nipple), or *mag* views (magnification – used for calcifications). Supplementary views are used to work up summation shadows from standard views and are usually followed by ultrasound screening. There are numerous other views, however routine screenings usually make use of the presented 2-4 standard views [36].

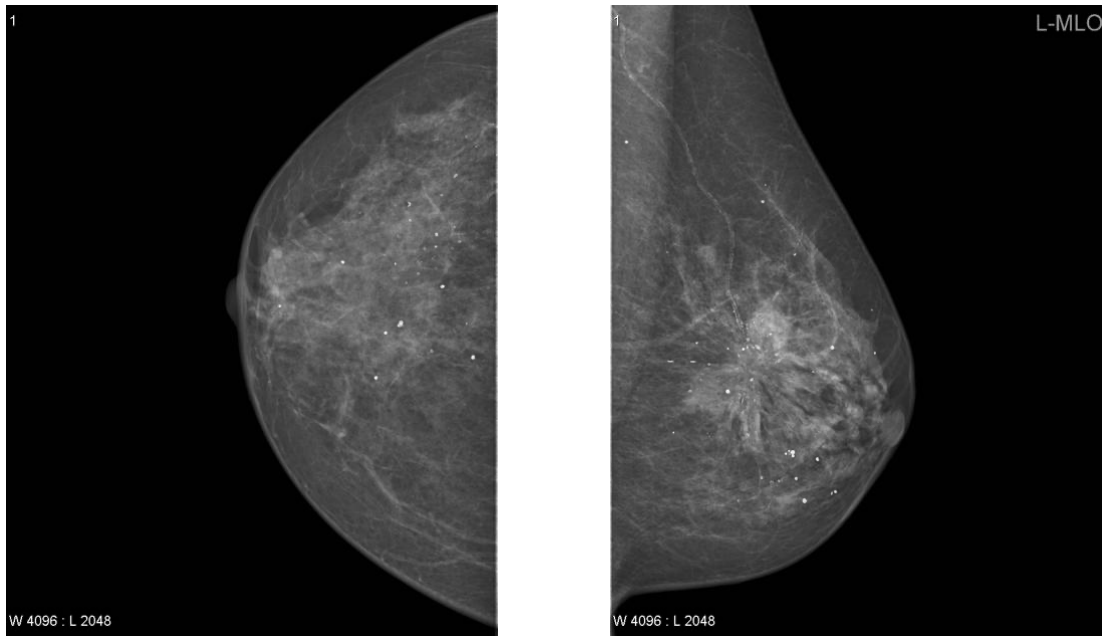


Figure 2: **Left:** CC - View. **Right:** L-MLO View.

Image Source: [37], Creative Common licence CC-NC-BY-SA 3.0

A notable difference between analogue (SFM) and digital image acquisition is the smaller dose. Digital systems cause about 20-30% lower dose for the patient ($\sim 1,86\text{mGy}$ for DM, $\sim 2,37\text{mGy}$ for SFM) [35].

Final components include an anti-scatter grid (however, not all mammography systems use a grid) followed by the image acquisition element (either a cassette in case of analogue (SFM) with the separate AEC (automatic exposure control), or a detector panel in case of digital detection system). The anti-scatter grid consists of lead stripes with a height to strip-spacing ratio of about 3,5-5:1 and moves perpendicular to the lead stripes. This motion during the exposure time blurs them out on the final image. The anti-scatter grid improves the image contrast, because it reduces scattered photons and prevents them from reaching the image plate (cassette or digital detector) (Figure 3). AEC (also called photo timer in case of SFM systems) is used to ensure consistent detector doses. It measures the amount of radiation that passes through the whole mammography setup and adjusts the exposure in real time. In case of a direct digital image detector as in FFDM, the AEC is usually incorporated into the detector panel.

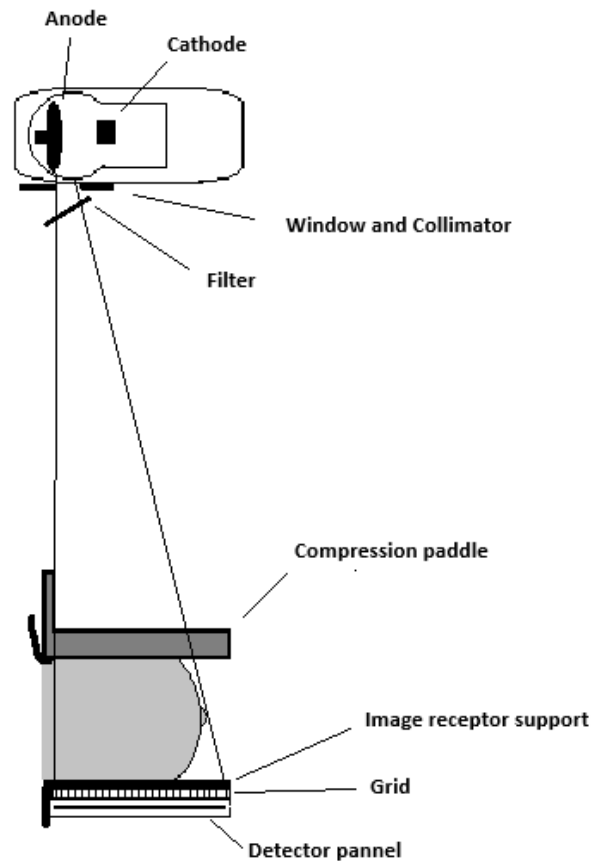


Figure 3 :Compressed breast in a FFDM system with a half field beam geometry.

1.3.1 2D Mammography

A full-field digital mammography (FFDM) setup is an X-ray conducted on the compressed female breast with very low-energy X-ray beams (20-35kVp). The amount and ratio of adipose and fibro-glandular tissue determines the breast composition. The denser glandular tissue absorbs X-rays stronger than the adipose tissue and creates the image contrast. The radiologist differentiates between normal and abnormal tissue formations via differences in contrast. Contours of lesions might give insight to the benign or malignant nature. The contrast to noise ratio (CNR) is one of the main parameters, together with spatial resolution and dose efficiency in 2D Mammography. While being simple and effective, the 2D nature of this imaging method has limitations, such as overlapping tissues which could obscure lesions, which is especially problematic with dense breasts (high fibro glandular/adipose tissue ratio). A work around would be additional images (views) from different angles.

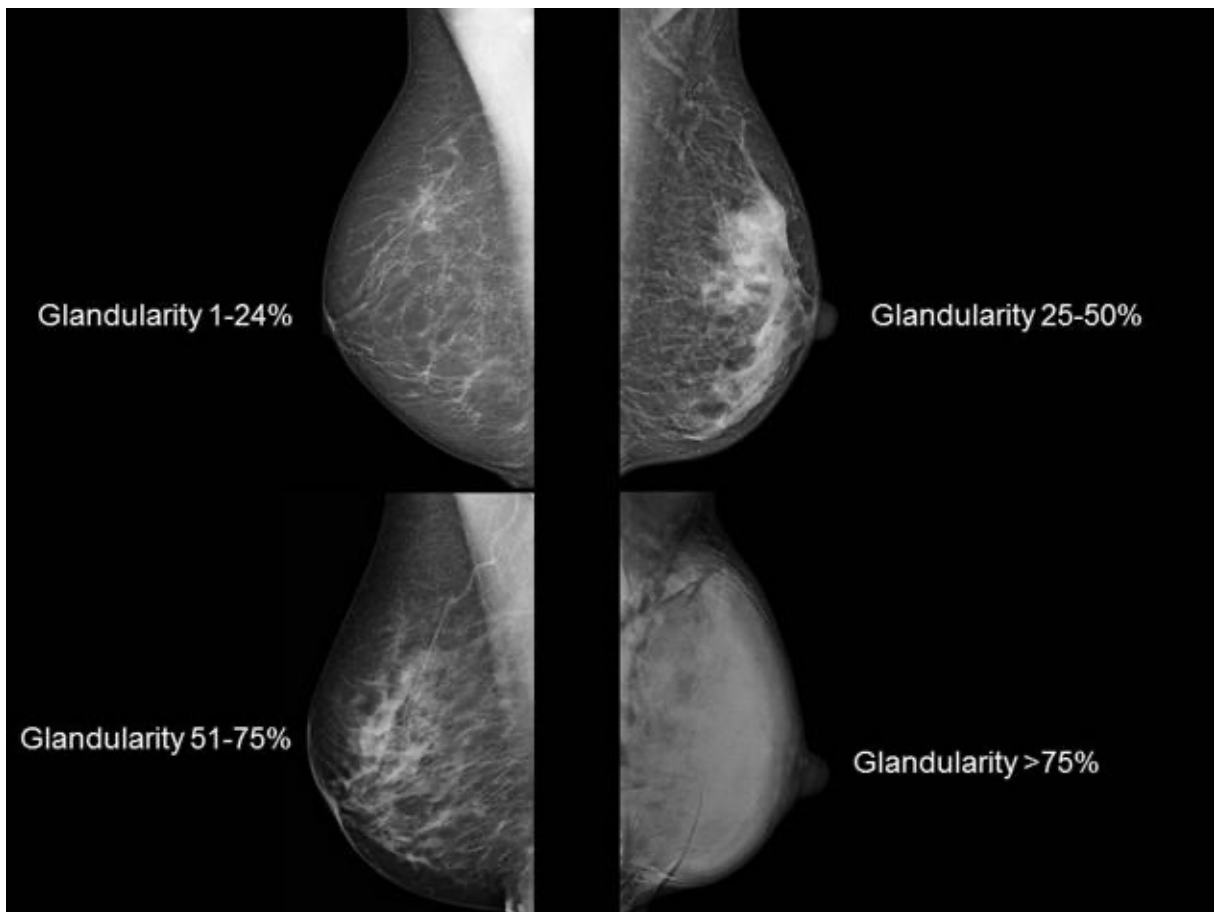


Figure 4: Different breast types with regard to fibro glandular tissue density. Image source: Holland M. [38]

1.3.2 Digital Breast Tomosynthesis (DBT)

DBT is based on the same image acquisition principles as regular CT, however the angular sampling is limited. Instead of a full or half rotation, several images are acquired over a 15-50° arc in this quasi 3D imaging method. Adjacent slices of the breast are reconstructed with FPB or IR. This has the advantage of automatically producing several sliced views compared to one superimposed image as in 2D mammography, taking care of the described overlapping issue of different tissue layers. The breast is still in a compressed state during the imaging procedure. Especially for women with dense breasts the cancer detection rate has severely improved with DBT. The downside however, similar to CT, is the applied dose, since the breast is exposed to more ionizing radiation. Nevertheless the increase in information outweighs the negative aspects and the overall DBT dose levels still remain inside acceptable ranges [39].

1.3.3 Contrast Enhanced Dual Energy Mammography (CEDEM)

CEDEM or Contrast Enhanced Spectral Mammography (CESM), is an advanced form of either 2D Mammography or DBT, since the main difference is the administration of an iodinated contrast agent, which provides enhanced attenuation at energies above the K-edge of iodine at 33,2keV, increasing contrast in vascularized lesions. The medical explanation behind this, is that malignant tumours typically exhibit increased angiogenesis (growing and branching of vessels), resulting in a greater uptake and hence accumulation of iodine, compared to the healthy tissue. Two acquisitions or image sets with the respective mammography system are taken with different energy levels: one below and one above the K-edge of iodine (typically 40keV). In image processing these two images are registered and subtracted from each other to reveal the contrast enhanced areas. It offers an alternative to breast MRI, which is the most sensitive breast imaging modality. CEDEM offers comparable sensitivity, but has lower acquisition times and is cheaper machine cost-wise [40] [41].

1.3.4 Clinical Relevance

2D Mammography, DBT and CEDEM act as complementary tools in breast imaging. Routine screenings are usually performed with 2D Mammography including 2 standard views (=Screening Mammography). In case of a breast problem (pain, lump, skin thickening, nipple discharge), a potential overlap or a deeper investigation for other reasons, DBT and CEDEM come into play [42]. Ultrasound is a critical adjunct to diagnostic mammography, as it is a fast alternative imaging modality for a second look at symptomatic patients. Mammography reporting per se is standardized in BI-RADS: Breast Imaging and Reporting Data System, which has a strict lexicon, structured reporting and defined assessment categories.

1.4 Mammography phantoms

In this chapter four commercially available phantoms are presented with the respective design concept and the intended use. Further a short insight into the current mammography phantom research is given including physical and digital models together with software packages that are used for simulation and design purposes. The following discussed papers served as starting points in the attempt to establish new phantom concept designs with easily available materials.

1.4.1 Commercially available phantoms for breast imaging

The American College of Radiology (ACR) Full Field Mammography Phantom can test the performance of digital mammographic systems and covers the entire image detector, hence the additive term *full field*. This effectively prevents scatter. The phantom is accredited in two sizes, but both versions simulate the same breast thickness of 42mm. It is rectangle shaped with an exact thickness of 41,3mm simulating a compressed breast. The mimicked parenchyma make-up is 50/50% glandular/adipose tissue. The phantom is used to check whether the system can detect small clinically relevant structures like micro calcifications, tumour-like masses and fibrous structures in ducts. The ACR does not produce and sell these phantoms directly, but they accredit phantoms that adhere to the ACR standards. The ACR provides a detailed protocol on how a company can get a new phantom accredited via the ACR quality control manual [43].

Sun Nuclear (former CIRS) BR3D Breast Imaging Phantom - Model 020 is made up of 6 interchangeable slabs (100x180x10mm) with heterogeneous backgrounds that can mimic different amounts of breast glandularity and is intended for DBT [44]. Two tissue equivalent materials are swirled into each other, one being 100% adipose tissue equivalent, the other glandular tissue equivalent. The mix-ratio is 50/50% by weight. One of the slabs contains lesions (CaCO_3 specks) with variable grain sizes, spheroidal masses with variable diameters and small fibres with 10mm length, also with variable diameters. This structure slab can be slid in between any desired stack height. This phantom is used for assessing the system's target detecting capability, but it is not accredited by any official radiology institution. In an

evaluation paper on image quality assessment in DBT, Brunner et al. [45] concluded that the CIRS Model020 is not capable of providing useful information for image quality evaluation for DBT on its own.

The Tomophan Phantom is a DBT phantom consisting of a 3 component system: a 28mm test object, a 14mm spacer, (giving total thickness of 42mm) and a chest wall piece. The test object can be flipped, moving the primary test plane higher or lower in the imaging field. The 28mm test object can be used as a standalone to simulate a smaller breast or optionally an additional 28mm spacer can be added to simulate a thicker (56mm) breast. The phantom has several inserts such as 8 acrylic spheres to determine the systems low contrast capability, a 10x10x0,2mm aluminium foil insert for the calculation of the contrast to noise ratio (CNR) and 1mm aluminium beads along the z-axis for image scaling evaluation along the z-axis. The Tomophan phantom has all necessary perks to completely characterize a DBT system and also includes a web-based image analysis service called *Smári* in the commercially available phantom package [46].

Sun Nuclear (former CIRS) Contrast Enhanced Spectral Mammography Phantom - Model 022 is used for quality control in CESM systems and made of 4 slabs. The overall dimensions are 180x110x100mm (stack size can be reduced to simulate different breast thicknesses). One target slab consists of a 50/50% glandular/adipose tissue equivalent mix with 2 sets of 5 iodine plugs on each half. The iodine concentrations are 0,2/0,5/1,0/2,0 g/cm², representing the clinical range, together with a 5th plug being 100% glandular tissue equivalent, and is centred in the middle of the 4 iodine plugs as a glandular tissue reference point. A contrast slab is divided in the middle between 100% adipose and 100% glandular tissue on each side in order to test the iodine concentration of the plugs with 2 homogeneous backgrounds. The 2 remaining slabs of 100% adipose tissue equivalent are the top and bottom slabs with rounded outlines to resemble the compressed breast during mammography, similar to the slab design in this thesis [47].

1.4.2 Recent developments and state of the art in mammography phantom research

The quality of mammography phantoms has improved significantly, as part of the advances of imaging technology and phantom research in general. The main focus of recent improvements lies on breast tissue equivalence, further enhancing anthropomorphic design and realism in physical and digital/software models. 3D printers and the printing materials have become better in quality, which improved the printability of complex geometries. This, in turn has significantly increased the amount of design and manufacturing possibilities in (3D-printed) phantom research. Varallo et al. [48] created a FFDM/DBT phantom design simulating a compressed healthy breast by using a digitally reconstructed patient model as a design basis. Three physical models were 3D-printed with a dual extrusion FDM printer (Ultimaker S3 [49]), using PLA/PET filaments as a substitute for skin and glandular tissue and ABS for adipose tissue (Figure 5). In different print approaches both PLA and PET were used as a skin envelop into which the phantom, divided into 12 slices with 1cm thickness, could be inserted. Due to the asymmetrical geometry the slice order remains fixed, but separating the model into parts allows for the insertion of dosimeters or other desirable objects like pathological structures imbedded into a slice substitute. By using power spectral analysis for DM and DBT the β metric [50] was estimated and compared with clinical images. The β metric analyses textures by focusing on the edge-preservation characteristics. Power spectral analysis analyses the spatial frequency content of images and allows to evaluate noise and textural patterns in images. They concluded that the calculated phantom β value (implying the texture complexity of the model) is more or less in line with the clinical data they used as a reference. However the clinical data amount used for comparison was smaller compared to similar studies, meaning that the clinical β reference value could be different in larger data sets. Further they pointed out some unwanted air gaps between the envelops and the stacked phantom slabs, which they accounted to material shrinking during the cooling process.

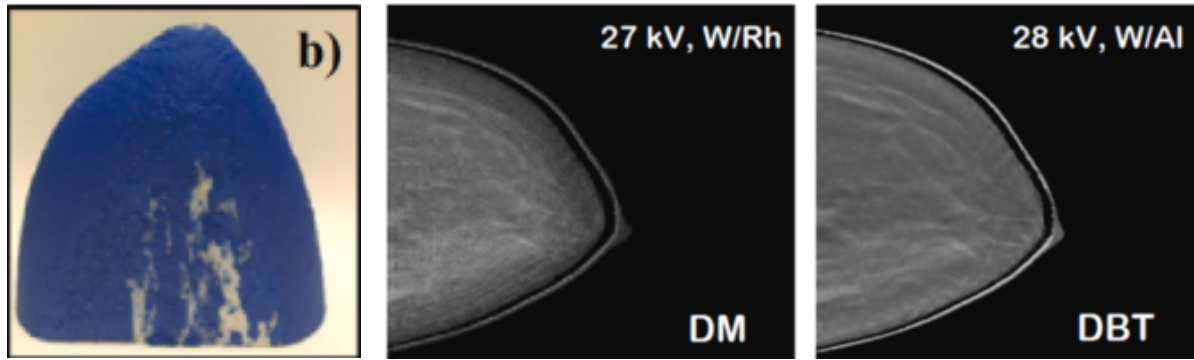


Figure 5: **Left:** Dual Extrusion printed mammography phantom PDM3

Right: FFDM and DBT images of the Phantom.

Image Source: Varallo et al.[48]

Rossmann et al. [51] worked on a hybrid model, being partly of anthropomorphic nature, but also including a uniform phantom design compartment for standard quality control metrics. They used photopolymer inkjet printers (*Objet Connex 350*, and *Objet Eden 333*) with the photopolymer inkjet materials *TangoPlus* and *VeroWhitePlus* for imitating adipose and glandular tissue and a *Jflexible Resin* doped with 3 w% zinc-acetate and 1.6% tungsten powder to meet the radiodensity for glandular tissue. This design allows small lesion-simulating inserts (micro lobulated with 0,2 – 0,5mm diameter) to be mounted onto a structure plate (Figure 6 Middle), which can be slid between the anthropomorphic slabs for contrast enhanced imaging. The contrast enhanced lesions were printed with 2,4,6 and 8 w% of iodobutane.



Figure 6: Modular phantom

Left: Top and bottom half with the anthropomorphic compartment in the front and simple standardized compartment in the back.

Middle: Insertable slab with iodine masses of different sizes with four different Iodobutane concentrations.

Right: CEDEM Image (left) and contrast enhanced DBT slice (right).

Image Source: Rossmann et al. [51]

Schopphoven et al. [52] simulated the parenchymal tissue patterns in an anthropomorphic phantom for FFDM by 3D-printing a compressed breast-resembling slab with a height profile on top. The different surface peaks of the phantom represent the grey value distribution of an unprocessed clinical FFDM image, which formed the basis for a 3D digital design model. The model was printed with a Polyjet 3D printer (*Stratasys Objet 30pro*) with a polypropylene like printing material *Rigur RGD450*. A PolyJet printer is a high-precision 3D printer that deposits a liquid photopolymer layer by layer, and curing it with UV light. The mathematical approach for calculating the respective z-heights to resemble the pixel values, was done by fitting the logarithmic Intensity ratio $\ln\left(\frac{I(z)}{I_0}\right)$, representing the attenuation*depth product, to a 2nd degree polynomial. The FFDM system used for calibration responded in good agreement to the phantom considering AEC (automatic exposure control) segmentation, and automatically selected exposure parameters. This means that the system automatically used similar imaging settings because the phantom was able to simulate the original breast (from which the initial FFDM image was acquired that posed as a design basis for the phantom), hence had similar mammography machine settings. 5 human readers from the German mammography screening programme also confirmed the realistic image impression.

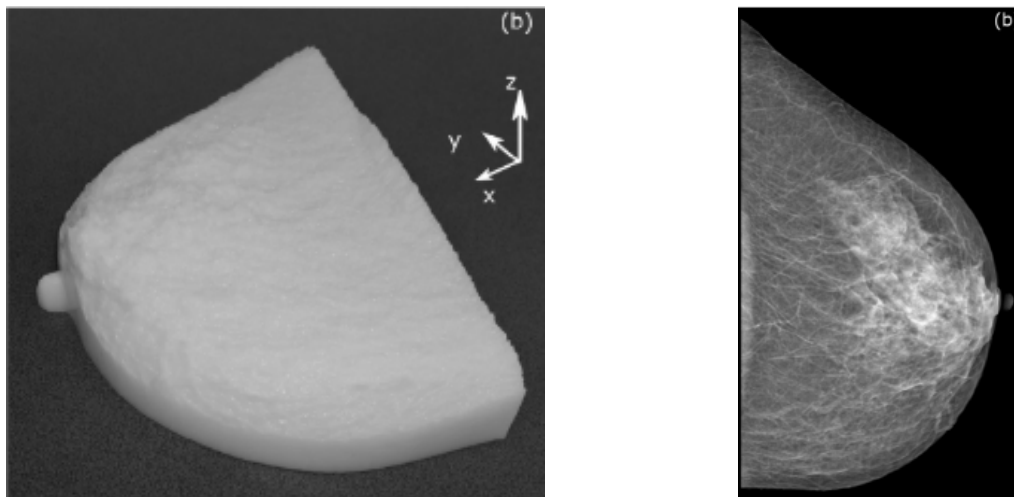


Figure 7: **Left:** 3D-printed compressed breast with a height profile on the top surface.

Right: FFDM image of the phantom.

Image Source: Schopphoven et al. [52]

Although being related to digital X-ray rather than mammography, a similar concept to Schopphoven et al. [52] was realized by Irnstorfer et al. [53]. In this approach a anthropomorphic phantom of a neonate was realized by 3D-printing a height profile, which was calculated and designed in a way that the surface peaks were orientated towards the X-ray machine focal spot, so that the resulting image is compensated for the distortion due to perspective projection in X-ray.

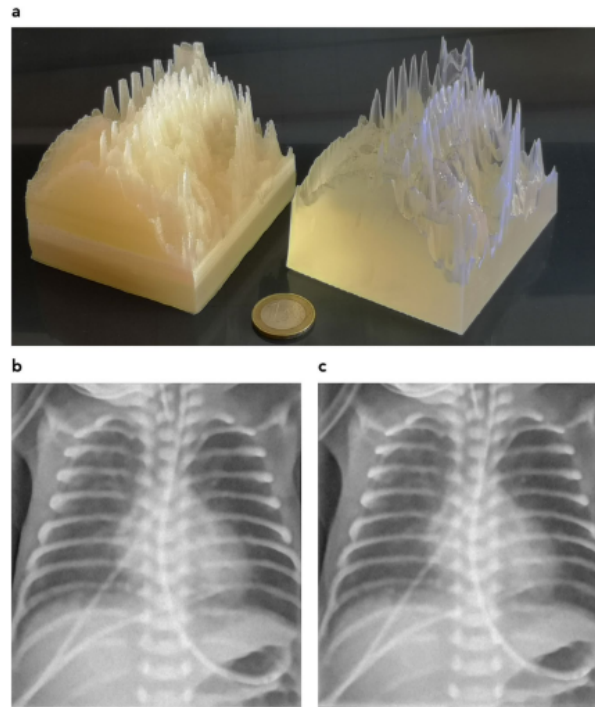


Figure 8: X-ray phantom of a neonate.

A, Left: Neonate phantom is printed via FDM with the respective X-ray image in b)

A, Right: Neonate phantom printed with SLA with the respective X-ray image in c).

Image Source: Irnstorfer et al. [53].

Cockmartin et al. [54] designed an anthropomorphic breast model with a 48mm thick PMMA shell and different sized spheres put inside. The intermediate space was filled with water and a structure plate was installed inside with 3D-printed spiculated and non-spiculated masses of various shapes and diameters along with microcalcification targets. The idea was to have a phantom, which upon shaking can change the pseudo-anthropomorphic pattern created by the spheres, and hence get different tissue imitating background patterns (anatomic noise) for repeated measurements. This is interesting in regard to machine learning and AI related

observer models, since it prevents the programs to look for reference points in the pattern, and bypass the actual observation task. The phantom was evaluated on five different systems, each with DBT and FFDM imaging, and the target detection was cross compared between DBT and FFDM and between machines. The images were evaluated by 5 readers via the 4-AFC paradigm (4 alternative forced choice). The structured phantom pointed out clear differences between the detection performance of DBT and FFDM, with DBT outperforming FFDM in finding the spiculated masses (reached almost 100%). The phantom was deemed suitable for testing DBT systems during calibration and quality control.

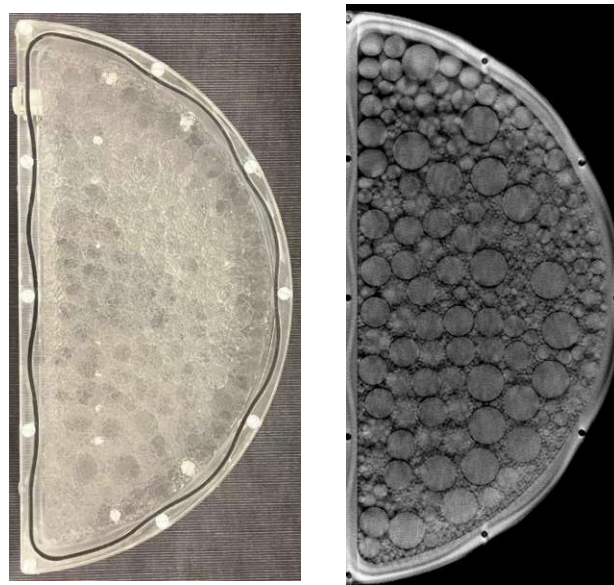


Figure 9: **Left:** L2 Phantom by Salomon et al. [55].

Right: DBT image.

Courtesy of the group of Prof. DDR. Johann Hummel who provided the DICOM files.

Ivanov et al. [56] conducted several experiments on computationally modelled step-wedge phantoms, which were 3D-printed with 21 materials in order to evaluate the linear attenuation coefficient (relevant for absorption imaging) and refractive index (relevant for phase-contrast imaging) with respect to skin, glandular and adipose tissue. This included solid filaments for FDM and resins for SLA. They took images with monochromatic beam energies of 30, 45 and 60keV and increasing step-wedge phantom thickness. The resulting data were cross correlated with the known tissue values and tables, and the respective deviation for all 21 materials at the measured photon energies were calculated. Nylon, PETG and Hybrid together with clear resin

based materials were the most suitable for skin and glandular tissue, due to the lowest difference in linear attenuation for absorption imaging. ABS resulted as the best candidate for imitating adipose tissue. For phase-contrast imaging ABS also came closest in imitating adipose tissue but at the same time was also a good candidate for glandular tissue and skin tissue. Mettievier et al. [57] conducted a similar set of experiments explicitly for FDM printing materials. PLA (white & orange), PET, NYLON and ABS were tested as substitute materials for skin, glandular and adipose tissue to assess the linear attenuation coefficient. In regard to Mammography phantom materials this paper is interesting, because the imaging energies covered spectra close to the mammography spectrum, between 14-36 keV, with especially the range of 28-36keV being relevant for CEDEM. The test objects were printed as step-wedge phantoms in the same manner as Ivanov et al. [56] did, and printed on the Ultimaker 3. The results were plotted as a Linear attenuation coefficient/Photon energy diagram with the initial tissue attenuation data for skin, glandular and fatty tissue by Boone [58] (Figure 10).

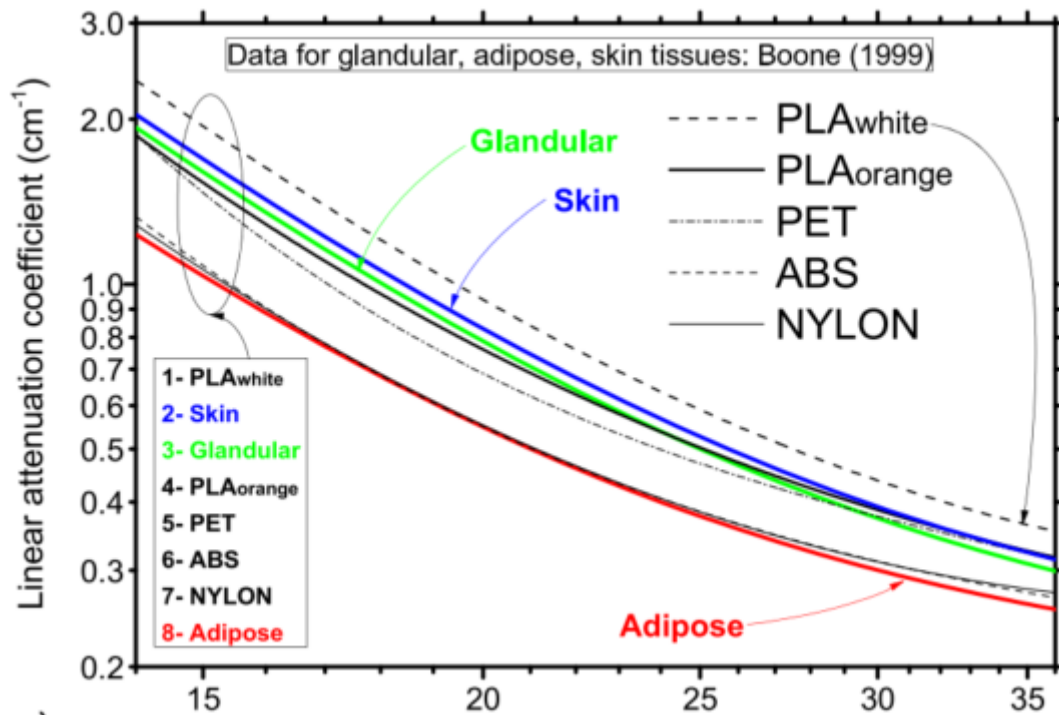


Figure 10: Linear attenuation coefficient of the tested FDM materials with the included tissue data by Boone [58].

Image Source: Mettievier et al. [57]

Regarding digital models, their clear advantage lies in the adjustable complexity and general flexibility to alter the dimensions and physical parameters to meet the wanted anatomic composition. Depending on the available computing power and utilising realistic imaging simulations like ray-tracing models, the simulations can come very close to real conducted imaging procedures. The previously described phantom by Cockmartin et al. [54] is the physical variant of four computational breast phantoms which were designed by Baneva et al. [59], two of which were realized as physical phantoms. The basic design is a semi-cylindrical shape filled up with spherical beads of different sizes. Both physical and digital models of the same design were compared next to each other in DBT and FFDM with identical incident air kerma conditions (DBT: 7,4mGy, FFDM: 4mGy). The digital design process was done with a dedicated in-house software *LUCMFRGen*, which stacked 29.000 virtual spheres in a semi cylinder, but with the restriction that none of them overlapped with a stacking density of 64%. In the evaluation process a subjective and quantitative comparison of virtual and real phantoms in DBT and FFDM showed a very good agreement. The fractal dimension, indicating the complexity of the simulated parenchymal tissue pattern, and Power Noise parameter β were higher for the real images, but the authors claim that the characteristics of sharpness and scatter were not simulated and shall be a task for future work. A completely new digital multi-modality breast phantom was composed by Kontos et al. [60]. It is based upon a cube-like geometry, and formed to a breast shaped volume via deformation processes. Just as physical phantoms, its intended use is to test imaging system performance. Ten individual tissue compartments in the breast were created via the Voronoi technique, including the glandular ducts, fatty tissue, and a vascular network. The Voronoi technique is a method to divide a given space by setting seed points which expanded homogenously in all directions until coming in contact with a neighbouring expanding seed point. The glandular system with ducts and lobes were grown from the nipple towards the chest wall. A Perlin noise function was used specifically for the fat and glandular lobes for a more realistic simulation of the tissue interfaces and Cooper's ligament network. The Perlin noise function is a gradient (vector based) noise algorithm, which generates pseudo-random values across a continuous space. The vascularization of the model was grown from the chest towards the nipple. For the simulation of the imaging procedure in a

patient the digital breast model was compressed with a neo-Hookean elasticity model. A neo-Hookean elasticity model describes elastic behaviour of materials undergoing large deformations and is used in continuum mechanics. Due to computational restrictions the final voxel size was set to 120um, although finer sizes of 50um are practical but memory demanding. While this model exhibits great complexity in terms of adjustable tissue parameters and compartment-variety, further ex vivo research was advised by the authors, especially in regard to morphological patterns (duct network complexity and realistic size ranges for lobules and shape characteristics). A similar but more compact software package was developed by Blzinakova et al. [61] named the *BreatSimulator*. It provides a simple GUI, with which 3D breast models of a desired composition can be designed. A set of 4 main modules and further submodules allows to define the external shape and a structure with different compartments for 5 tissue types: glandular and adipose tissue, breast lesion, skin, pectoralis and lymphatics. Like in the breast simulation software by Kontos et al. [60], it is possible to simulate a compression and virtual imaging procedure including a conventional and dual energy imaging. The conducted experiments included the optimal pairing of low and high monochromatic energies for virtual dual energy mammography. The energy range was set between 14-28keV and 225 energy pairing combinations were tested. The virtual subject created with BreastSimulator was a medium sized breast model with one calcification present. The combination of 17 and 28keV resulted as the best incident monoenergetic beams for maximum detectability of the calcification. In a second study the effect of breast compression was analysed and the conclusion was that an increased mammogram image quality is obtained with decreasing breast thickness. The breast model of the second study was based on real CT slices. The third and last study analysed the beam trajectory of scattered X-ray in a small breast and showed the increase of the scatter angle with increasing X-ray energy. The BreastSimulator was further evaluated by Mettivier et al. [62] in a separate paper and compared simulated CT images with clinical breast CT scans, focusing primarily on the β metric [50], which describes the anatomic noise in terms of texture complexity in breast images. The virtual models closely matched the real clinical CT value β , which means that the BreastSimulator is capable of creating virtual anthropomorphic phantoms suitable for image quality assessments. A quasi-realistic voxel

based mammography phantom was created by Elangovan et al. [63], intended for FFDM and DBT use. The approach is based on a collection of 100 DBT slices of real breasts from asymptotic clinical cases rich in glandular tissue for the extraction of the anatomical features. An initially empty breast volume with high resolution was created by thresholding from the DBT patient images via the OPTIMAM image simulator framework. The OPTIMAM simulator is part of a project by the NCCPM, which is dedicated to finding optimal methods and parameters in a VCT (Virtual Clinical Trials) approach [64]. The outline resolution was 100 μ m and the same voxel size was used for the internal compartment structure. The skin thickness was approximated with 1,5mm, and the enclosed volume defined as adipose tissue before being partly reassigned to other tissue types. The glandular tissue was grown by setting certain seeds points inside the volume, and applying a growing pattern which would simulate the structure of previously analysed real DBT images rich in glandular tissue as a scaffold. Cooper's ligaments and blood vessels were implemented by setting landmark points inside the volume and then connecting these landmarks with 3D splines, which were dilated after the connection process to simulate a vascular network. The validation process was comprised of several methods to evaluate the digital phantom images for FFDM and DBT. A Fractal Dimension Analysis was conducted, where the fractal dimension of the simulated images were compared to real clinical DBT and mammogram images. With no significant differences, the complexity was assumed as realistic. A power spectrum analysis compared the statistical image properties and the model images passed as realistic with a <7% difference in 2D mammograms and <4% in DBT compared to clinical images. Additionally 7 real human observers, two of which had significant experience viewing DTB images (over 25years), rated 30x30mm image patches in a forced choice method with 4 options, 3 of which were from real clinic images, 1 simulated. One of the observers, who had the most experience, pointed out certain patterns in the images looked too symmetrical, which the authors attributed to the Cooper's ligaments and blood vessel simulation approach. Overall also the human observer data led to the conclusion that this virtual phantom approach has a high amount of realism in simulating 2D mammograms and DBT images.

2 Materials and Methods

2.1 Phantom designs

This chapter describes the complete design process of all Phantom models in detail, with a thorough explanation of the essential design steps in the respective software packages Fusion by Autodesk and Blender 4.2.

2.1.1 Three component basic model - CBM

The assembled CBM phantom consists of a stack of 3D-printed interchangeable anthropomorphic plates, further referred to as *slabs*, in semi-circular shape. It is supposed to resemble a compressed breast during mammography (Figure 11). The individual slab geometries are 240x120x13,3mm each, giving 240x120x39,9mm in stacked formation. The slabs depicted in Figure 11 are numbered Slab #1 - #3 from top to bottom. Slab #2 has a flat edge, while the outer edge of Slab#1 and Slab#3 is rounded, in order to imitate the volumetric change of the breast during compression. The radius of curvature for the rounded edge in Slab #1 and Slab #3 is the same as the respective slab thickness (13,3mm). The wall thickness is 2mm for Slab #2 and 1,2mm for Slab #1 and #3. A wall thickness of 2mm for Slab #2 is a compromise of stability and enough wall volume to allow for potential iodine platelet inserts with a thickness of 0,8mm. This design concept was implemented specifically for CEDEM, but the platelet inserts were ultimately not realised. The individual slab wall thicknesses of 2mm and 1,2mm, both fulfil the requirement of a manifold of 0,4mm which is the nozzle diameter of the used FDM 3D printer (FLSUN V400 [65] [66]). This ensures a consistent layer width and no unwanted overlaps during the printing process. The rear end of each slab remains open to allow for filling with an adipose tissue equivalent, which was done with coconut oil. The stack of slabs can in theory be expanded by additional interchangeable middle slabs like Slab #2 to simulate a thicker breast with less glandular tissue density. However, further calculations showed, that a linear increase with additional slabs of the same thickness does not comply with

the *Mass-Glandularity to compressed breast-thickness-ratio* presented by Dance et al. [67], upon which the initial design calculations for the inner structure volumes rely (see Figure 12). Each slab body is initially of hollow design, with a specific inner structure added during the second half of the design process. This inner structure simulates the female breast parenchyma visible in a mammography scan, in particular the *glandular tissue network*. The phantom is designed as a two tissue types imitating compartment model: glandular tissue with ducts exhibiting diameters of around 0,1mm up to 2,5mm, and adipose tissue filling the intermediate space. The slab envelop or *casing* is considered to imitate skin, but is not given an individual material for simulation. It is represented by the same material as the glandular tissue, because the X-ray attenuation for both tissue types is very similar around 28keV (see Figure 10). Since a majority of the real anatomical diameter distribution of the glandular ducts is mostly in the range of 1-2mm, the design of the inner slab structure is also based around these diameters [68].

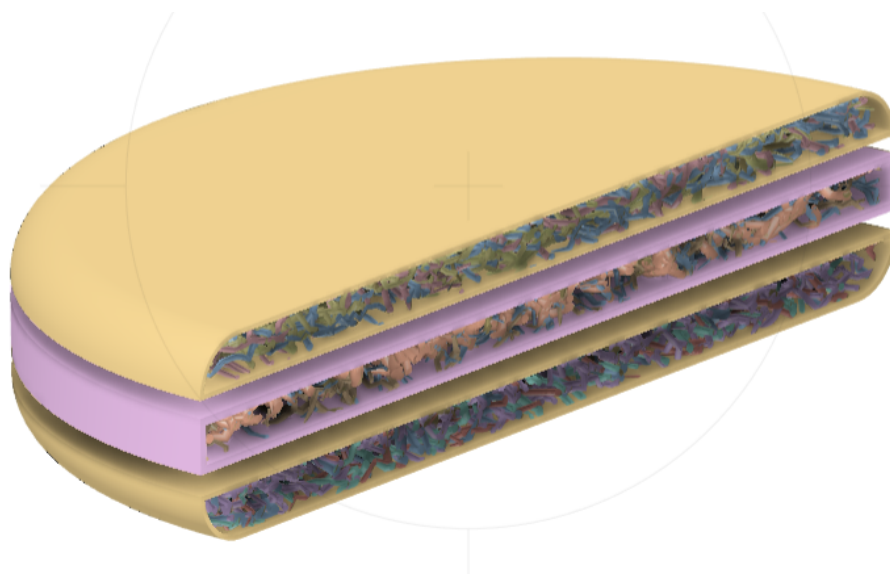


Figure 11: Rear View: Fusion Design Rendering of Three Component Basic Phantom (CBM). Slab numbering from top to bottom: Slab #1, Slab #2, Slab #3. Measurements: 240x120x39,9mm

The basic design, in terms of shape and geometry, was inspired by the phantom design of Cockmartin et al [54] and the advanced L2 phantom by Salomon et al. [55].

The slab casings were designed first with CAD software Fusion, while for the inner structures Blender 4.2– Ivy Generator Plugin was used. Each inner structure is a combination of several cut-outs of big random tubular patterns created with Blender Ivy Generator (Figure 14). The

respective slab outline acted as a cutting scaffold (Figure 15). The slab casings were designed in Fusion as “volume bodies” and converted to “mesh bodies” as STL files. For all the initial Slab #1,#2,#3 hollow casings, a full-volume complementary slab was additionally created. These full-volume slabs are imported into Blender, acting as the necessary cutting scaffold for the desired random tissue structure (also called *Ivy structure*, after the Blender plugin Ivy Generator).

Calculation of the inner structure (glandularity) volume

All slabs in the CBM phantom act as so-called *pseudo-anthropomorphic structured background plates* because they simulate the breast parenchyma during mammography. Slab #1,#2 and #3 each contain approximately one third of the total inner structure volume, that is simulating the glandular tissue. The calculations for the required inner structure volume are based on the findings of Dance et al. [67].

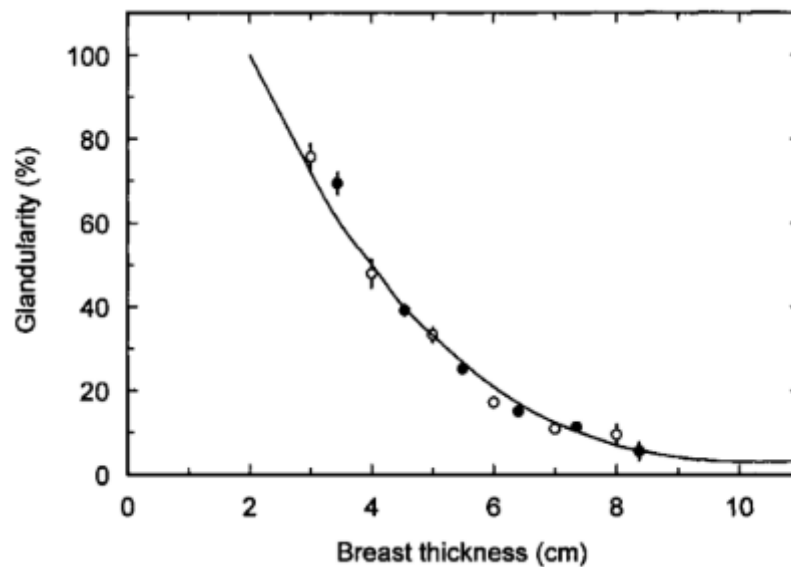


Figure 12: Mass glandularity/compressed breast thickness relation by Dance et al. [67]

The calculation of the necessary inner structure volume according to the phantom thickness (40mm for the CBM phantom), is based on the change of mass glandularity [%] in relation to the compressed breast thickness [mm] according to Dance et al. [67], with the respective

diagram depicted in Figure 12. A 50% mass glandularity corresponds to a compressed breast thickness of 40mm.

The depicted mass-glandularity had to be converted into volume-glandularity. The *International Commission on Radiation Units and Measurements (ICRU) reports 44&46* [69] defines the density of glandular tissue with $\rho_{glandular} = 1,04 \frac{g}{cm^3}$, and adipose tissue with $\rho_{fat} = 0,92 \frac{g}{cm^3}$. Therefore the mass-volume conversion can be expressed as:

$$G_{mass} = \sim G_{volume} * \frac{\rho_{glandular}}{\rho_{fat}}$$

With $G_{mass} = 0,5$ this results in $G_{volume} = 0.4489 \sim 0,45$.

Since the CBM phantom is designed as a two tissue mimicking compartment model, all simulated tissue volumes for glandular and skin tissue were divided by the total volume of all three slabs:

$$G_{volume} = \frac{V_{TOP_S} + V_{TOP_C} + V_{BOT_S} + V_{BOT_C} + V_{MID_S} + V_{MID_C}}{V_{TOP_F} + V_{BOT_F} + V_{MID_F}}$$

The total volume of each slab, as well as the casing volume were calculated directly via Fusion object analysis (see [Table 1](#)). The vertical wall volume of Slab #2 Casing V_{MID_C} is intentionally not considered, since it does not contribute to the X-ray attenuation during projection. The Slab #1 and Slab #3 casing walls do so due to their outline curvature. Hence the total volume of Slab #2 casing reads as: $V_{MID_C} = R^2\pi * t$ (with t being the wall thickness).

The calculated sum of the glandular structure volumes for Slab #1, Slab #2 and Slab #3 slab resulted in: $V_{TOP_S} + V_{BOT_S} + V_{MID_S} = \sim 180000mm^3$, giving $60000mm^3$ for each slab equally. Since the casing geometry of Slab #1 and Slab #3 is identical and both slabs only differ in the internal structure they can be switched from top to bottom of the phantom stack to gain an altered background structure during imaging, or alternatively Slab #2 could be flipped.

The following table shows a summary of all calculated volumes of the respective slab geometries, including the casings, the inner structure, and the total volume of each slab.

Table 1: CBM phantom volumes for $G_{volume} = 0.45$

Volume element	Abbreviation	Volume in mm ³
Top structure/glandular volume (Slab #1)	V_{TOP_S}	59698
Top casing	V_{TOP_C}	56626
Bottom structure/glandular volume (Slab #3)	V_{BOT_S}	58932
Bottom casing	V_{BOT_C}	56626
Middle structure/glandular volume (Slab #2)	V_{MID_S}	62820
Middle casing	V_{MID_C}	97385
Full volume Slab #1	V_{TOP_F}	286900
Full volume Slab #3	V_{BOT_F}	286900
Full volume Slab #2	V_{MID_F}	300839

Slab #2 – potential Structure plate: In the initial design idea of the CBM phantom, Slab #2 was supposed to have several holes drilled into the casing with 1mm depth and 0,8mm diameter. The idea was to insert iodinated platelets for CEDEM imaging and determine their visibility against the anatomic noise (=pseudo-anthropomorphic background structure, simulating the parenchyma). This would make Slab #2 not only a pseudo-anthropomorphic plate, but also a *Structure plate*, since the iodinated platelets would simulate potential pathological structures (cancerous tissue or calcifications). However during the course of the thesis the main objective changed towards a more design heavy approach in creating an alternative phantom design.

2.1.1.1 Inner structure

For the initial raw random structure (=raw Ivy Structure) to grow, a base growing surface needs to be placed, and a growing starting point determined (Figure 13). A thin (1mm) half-circular disc was used with the Ivy Structure-starting point positioned approximately in the middle of the edge of the rounded slab outline. The base disc was arbitrarily oversized to provide a big

enough growing surface for the Ivy structure, because the bigger the Ivy structure, the bigger the options to choose from considering which part shall eventually be cut out for the inner slab structure. The Ivy Generator plugin settings: *Generation*, *Size*, *Weight* and *Branch* allow for unlimited generation possibilities of Ivy structure patterns (Figure 14). Since every *growing basis*, *growth starting point* & *plugin settings* combination creates a unique new pattern, the exact structures used in this thesis cannot be replicated. Figure 13 & Figure 14 show an exemplary Ivy structure growing procedure with similar settings as were used in the CBM phantom design. The full-volume slab for the respective Slab #1,#2 or #3 is imported to Blender and fixed in the Blender coordinate centre. Then the generated Ivy structure is moved until the desired overlap position with the slab is reached (Figure 15, Left). Before the final cut, all scaling, rotations or Ivy structure branch-thickening⁴ operations have to be implemented. These transformation operations allow for an additional randomization step. With the *Boolean Editor Plugin* an *Intersection cut* between the Ivy structure and the full volume slab is made, leaving behind only the part of the Ivy structure intersecting with the full volume slab (Figure 15, Right). The result is saved as a new Ivy Structure Design STL file (e.g.: Slab#2_Design_001.stl) and imported into Fusion. With the implemented Fusion measuring tool the branch thickness is controlled, which is supposed to be between 0,8 and 2,5 mm to be anatomically realistic [68].

⁴ *Bevel depth* in the parameter window usually set from 1m to 1.5m or 2m

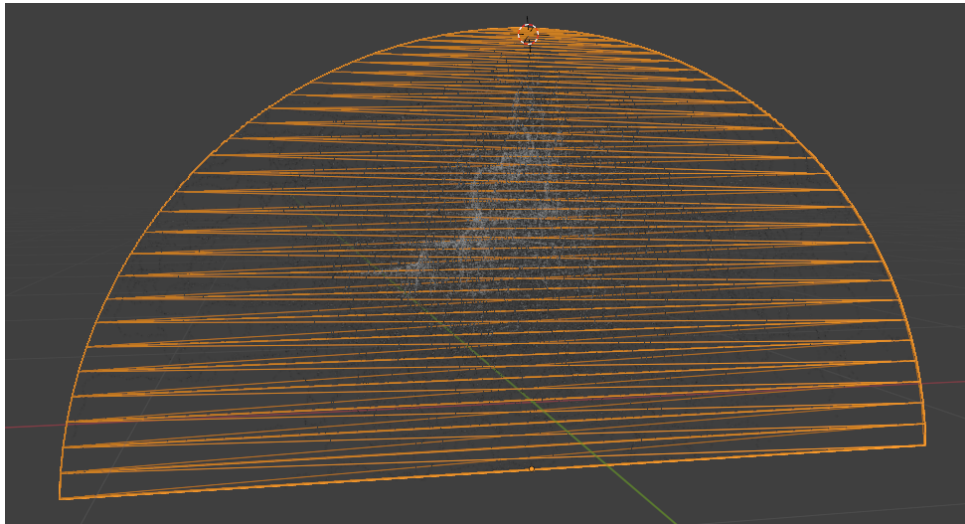


Figure 13: Wireframe half circular disc base surface (orange) with red-white striped growth starting point on top and a random Ivy pattern (grey) - Blender 4.2 Ivy Generator plugin

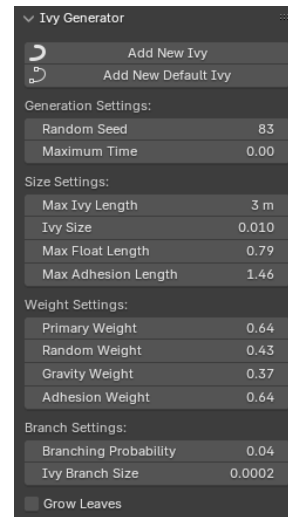
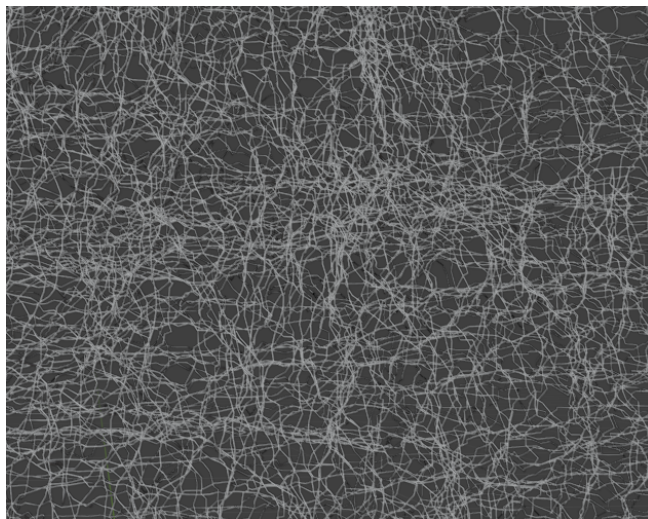


Figure 14: Zoom into the grown Ivy Structure in Figure 13 with the respective settings (The orange wire-frame growing basis from Figure 13 is hidden in this view).

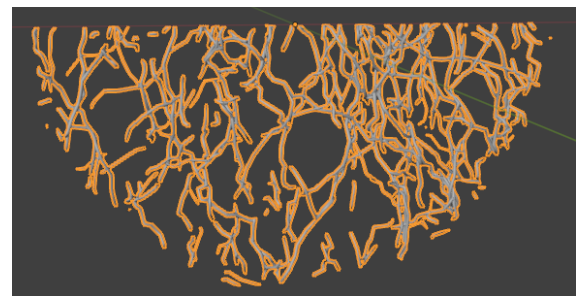
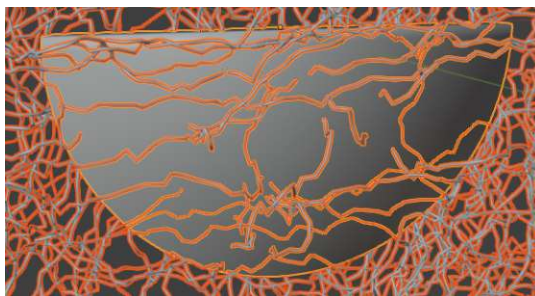


Figure 15: **Left:** Placement of the full volume slab (here Slab #2).

Right: Result of the intersection cut between the generated Ivy structure and the full volume Slab #2. Blender 4.2 – Boolean Editor plugin.

Combining the inner structure with the casing: To meet the calculated inner-structure volume requirements (Table 1) and an equal structure distribution across each slab, several individual Ivy Structure-meshes can be combined in Fusion and saved as a new united mesh body. This body is then placed inside the desired hollow casing, and scaled non-uniformly to reach a slight overlap between combined Ivy-Structure-mesh and the slab casing mesh. The down-scaling reduces the total size of the Ivy structure, therefore the Ivy Structures were already designed to hold 10% more volume than necessary (e.g. $\sim 66000 \text{ mm}^3$ to fit the desired 60000 mm^3 after scaling). This combining-step is very delicate and requires an exact placement, since the casing has to provide printing support for the inner structure on the one hand, but also act as a continuous boundary between slab inside & outside (see an example for Slab #2 in Figure 16). Placing the Ivy Structure mesh too close to the outer boundary of the casing will result in holes during the slicing process for generating the final print file in the slicer software! The last step combines the positioned Ivy Structure mesh with the casing mesh.

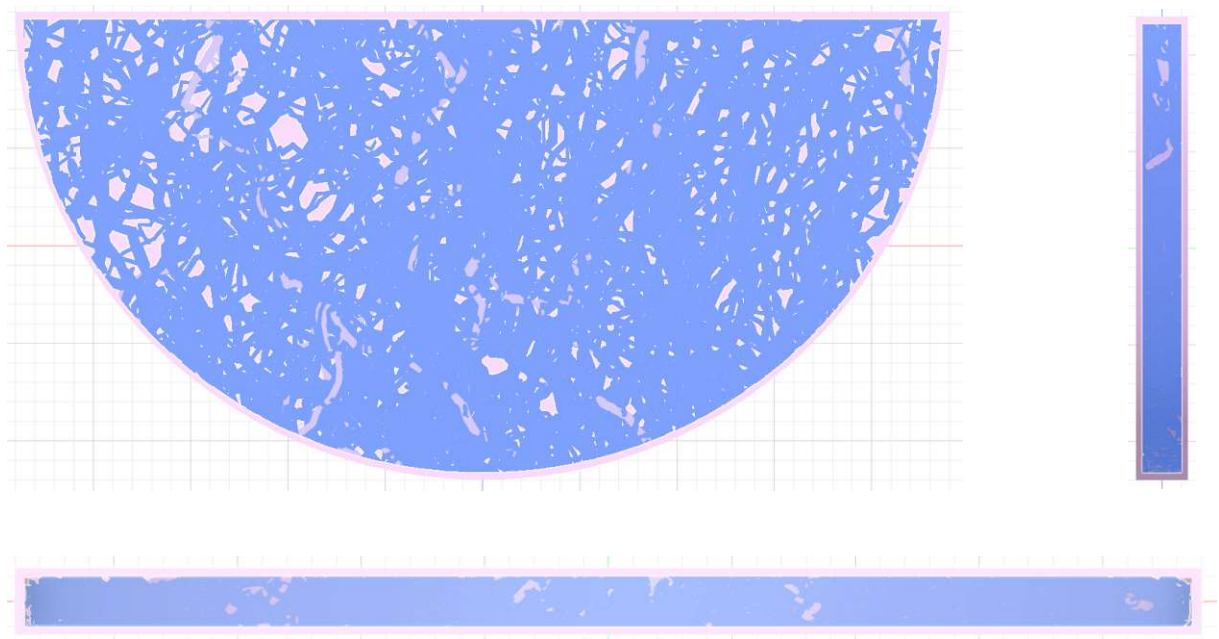


Figure 16: Alignment control of Slab #2 casing (pink) and the shadow of the rescaled inner structure (blue),

Left: Front view,

Right: Side view

Bottom: Chestwall view

2.1.2 Phantom 45

Phantom 45 is the 2nd Design concept of this thesis and consists of 3 slabs (Slab A, Slab B, Slab C) with a total thickness of 45mm. Slab B is 5mm thick, while Slab A and Slab C are 20mm each, with a wall thickness of 1,2mm (Figure 17). Opposite to the previously described CBM phantom with a total thickness of 40mm (3x 13,3mm), the anatomic noise in Phantom 45 is exclusively simulated by the top and bottom slab (Slab A and Slab C), while the *structure plate* (=Slab B) could potentially hold small iodine discs or arbitrary structures imitating pathological outlines. The outer slab diameter is 240mm, with a 20mm rounding radius for the edge curvature in Slab A and Slab C. The chestwall side of Slab A and C are closed. A 10mm infill hole is positioned in the middle of the curvature on the front side of Slab A and Slab C. The inside structures for Slab A and Slab C are initially designed in the same way as the CBM phantom, but in an additional step the 3D Ivy structure is converted into a height profile. The idea is that the height profile results in the same X-ray attenuation on the final mammography image as a real 3D structure would due to super imposition. For the effective path length and attenuation of the X-rays, the order, in which the photons pass through the materials, is irrelevant.

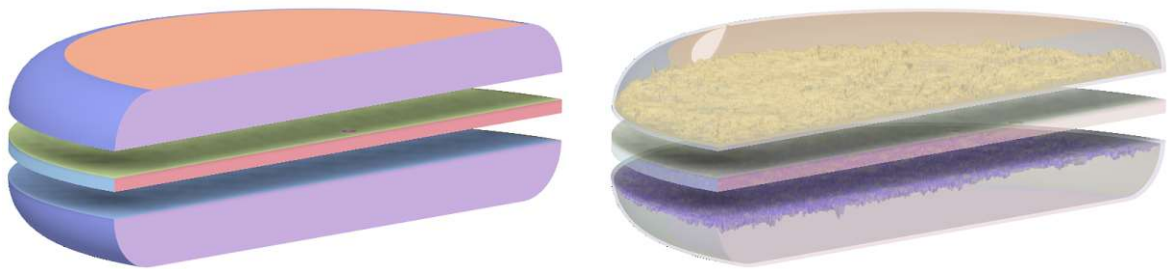


Figure 17: *Phantom 45* assembly.

Left: Two outer slabs (Slab A and Slab C). In between a structure plate (Slab B).

Right: Transparent view. The inner structures of Slab A and Slab C in the form of a height profile (yellow top/purple bottom) are visible.

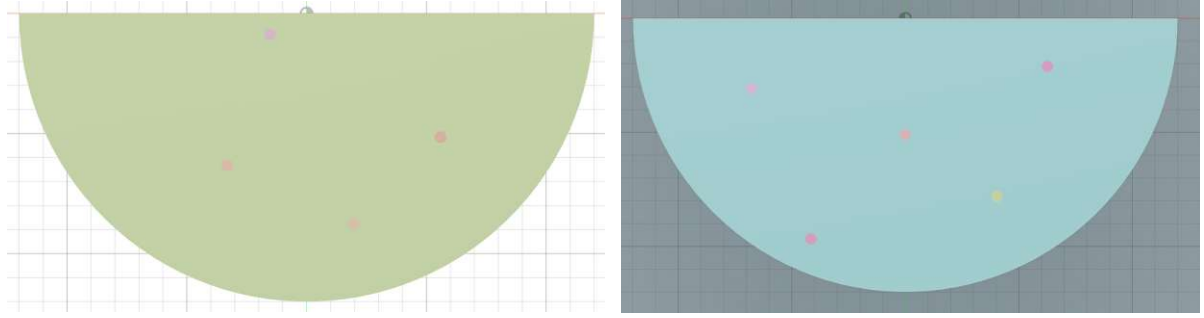


Figure 18: Both sides of a structure plate design with 9 arbitrarily set potential insert options for 0.8x5mm (depth x diameter) iodine platelets.

According to Dance et al. [67] a higher compressed breast thickness of 45mm results in a lower mass glandularity of about 40%, which translates to a volume glandularity of about 35%. The new geometry and tissue type distribution simplifies the volume-glandularity expression:

$$G_{volume} = G_{mass} * \frac{0,92}{1,04} = 0,3538 = \sim 35\%$$

$$G_{volume} = \frac{V_{pattern} + 2 * V_{casing} + V_{middle_{total}}}{2 * V_{outerslab_{total}} + V_{middle_{total}}}$$

Table 2: Phantom 45 Design Volumes for $G_{volume} = 0,35$

Volume element	Abbreviation	Value [mm ³]
Volume outer slab casings (A,C)	V_{casing}	58355
Total outer slab volume (A,C)	$V_{outerslab_{total}}$	421200
Total middle slab volume (B)	$V_{middle_{total}}$	113097
Total volume inner structure (A+C)	$V_{pattern}$	104616

A total inner structure volume of 104616mm³ is required for Phantom 45, in order to mimic the glandularity of a 45mm thick breast according to the glandular tissue/adipose tissue ratio curve by Dance et al. [67] (Figure 12).

2.1.2.1 Conversion of Ivy structure to Height profile

An alternative representation of the glandular tissue in the shape of a height profile was made to make the inner structure easier to print. A height profile has the advantage that it is a solid volume, with an alternating surface, but no cavities or complicated overhangs. Depending on the steepness of small phantom-features during the print, overhangs can lead to inaccuracies or failed filament deposition. These potential issues are avoided with a height profile. The existing Ivy structure design (e.g. *Design A*, *Design C for Slab A and Slab C*) for each slab was combined with a very thin slab with thickness of 0,01mm in the CAD software (Figure 19). This is a necessary intermediate step for the conversion of the Ivy structure to the height profile, and important for orthographic projection rendering purposes. Naturally the thin slab poses as an additional attenuation layer during projection and causes a higher grey level value over the whole Ivy Structure mesh evenly. But since this layer addition is homogenous for the total surface (meaning every pixel of the mesh surface), it will have little impact on the relation of the grey values between the pixels. In short: The whole image will get a little brighter for both, the software projection and the real X-ray image. In terms of added glandularity the effect is negligible. The initial hollow slabs into which the height profile-structure will be positioned have a volume of 63085mm^3 , and the thin slab has 539mm^3 , so the resulting error is less than 1%, while the error margin of the mass glandularity/breast thickness ratio according to Dance et al. [67] is around 2%.

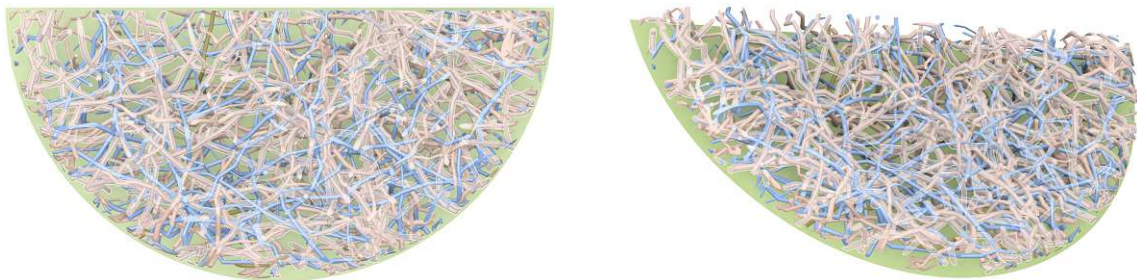


Figure 19: Top and shifted view of Design A put over a thin slab with 0,01mm thickness for easier Boolean operation during height profile conversion in Blender

This additional thin slab overlay was done merely because a Boolean-cutting operation (done in Blender) during the height profile design process requires a simple homogeneous surface

together with a simple vertices distinction in order for Blender to calculate the newly generated mesh correctly. A 8bit orthographic projection (Figure 27) of the thin slab/Ivy structure combination with 1280x1024 resolution was done and acted as a texture basis for the following design steps in Blender.

2.1.2.2 Height profile design with Blender

First a simple mesh *plane* is generated in a new blender file and divided into smaller units in *Editor Mode* (subdivision: 100 cuts, resulting in a 101x101 array). Back in *object mode* a *subdivision* + *displacement modifier* are assigned to the plane. The displacement modifier submenu: *texture* loads the .PNG file of the orthographic projection.

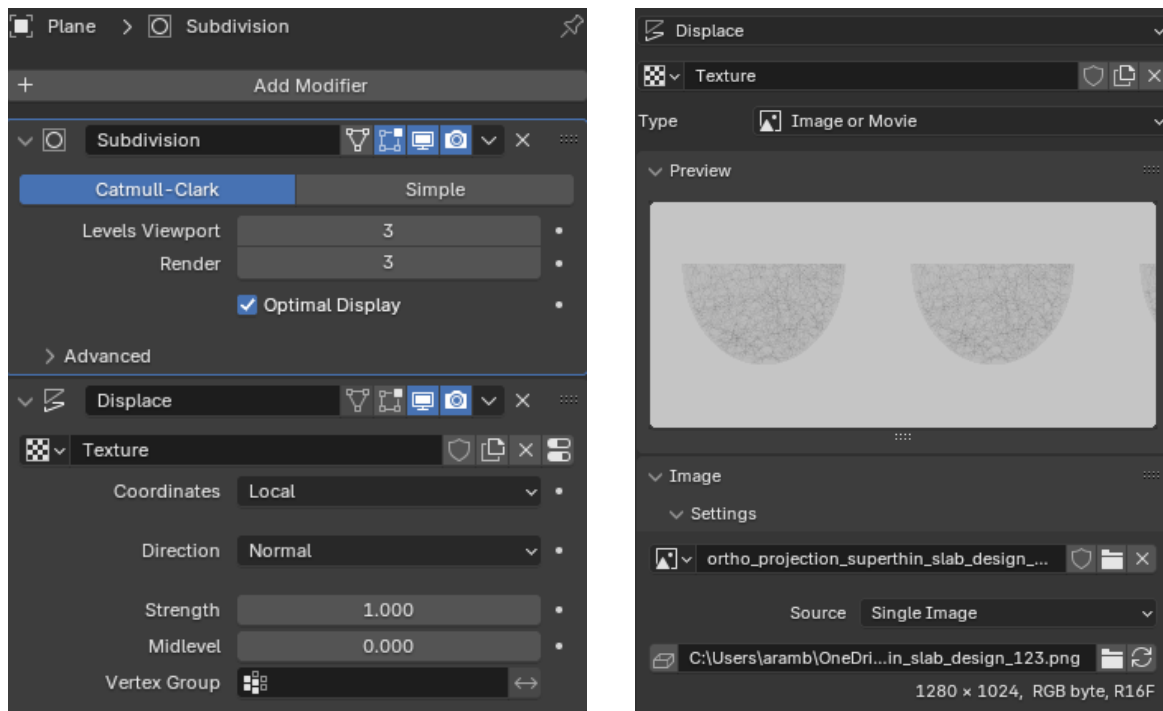


Figure 20: **Left:** Displacement + subdivision modifier settings for the plane extrusion and refinement level
Right: Example texture: “Design_A.png” is the orthographic projection image.

This transforms the plane into a height profile according to the grey level pattern in the projection image (loaded as the texture) displayed in Figure 21.

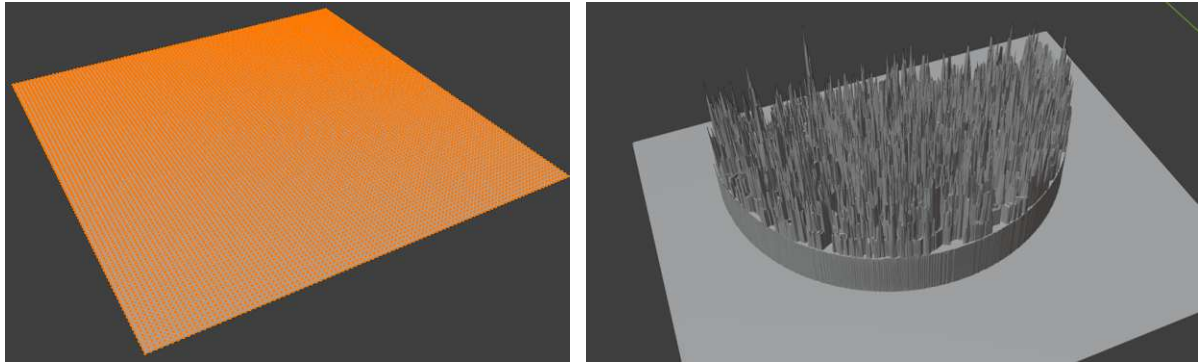


Figure 21: **Left:** Subdivided plane before the displacement modifiers are applied.

Right: Plane transformed into a height profile based on the orthographic projection of Design A.

The height profile needs postprocessing: The rectangular frame has to be removed. It represents no grey value information (the same as grey value = 0), indicating *no signal* in terms of a hypothetical X-ray image. The height profile surface must be closed and the remaining mesh scaled down to fit into the casings of Slab A and C respectively. The desired mesh state is called *watertight*, meaning a fully closed surface area, which is necessary for any 3D-printer slicing software to calculate the mesh volume, and thereby the printing steps, correctly. These two steps are done by adding a *cube*-mesh, which is placed beneath the height profile in the desired height (Figure 22). It is important, that none of the spikey area comes in contact with the cube. This step is the reason why the previously described very thin slab was combined with the Ivy structure of Design A (Figure 19): It will cause the height profile to have a very distinct rim (Figure 21 Right), a base so to say, which is ideal for a fast Boolean cutting operation. In this case the *Boolean - Difference* option was selected. The *cube* object must be selected first, and the *plane* object (=height profile) second to get the desired cutting result (Figure 22).

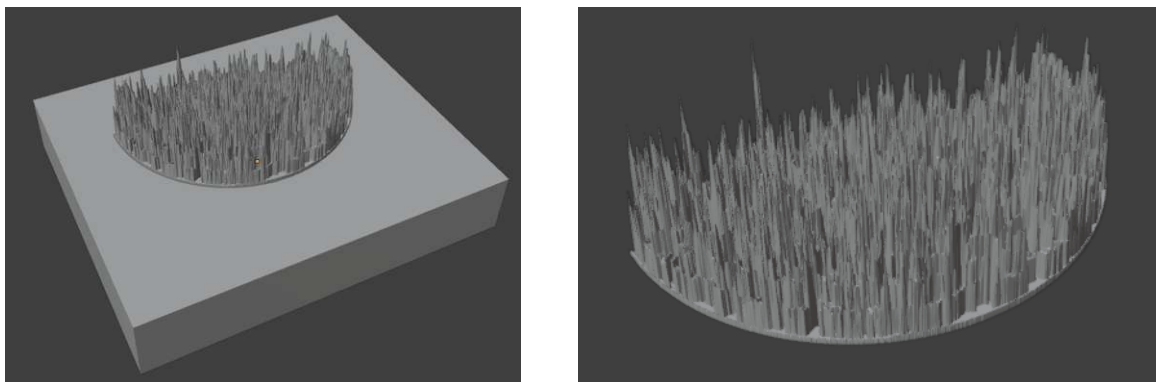


Figure 22: **Left:** Height profile with the added cube below for the Boolean Difference cutting operation.

Right: Cutting operation result: watertight mesh surface without the rectangular frame.

The divided plane initially had a 101x101 array, hence the xyz-dimension of the height profile has to be scaled down to 240x120x17.6mm to fit the slab casing ratio, but will require further adjustment in z (=height) direction in Fusion to meet the desired glandular volume. Eventually the height profile-mesh is exported (.STL) and loaded into Fusion for two remaining postprocessing steps: Potential holes and errors are repaired with the tools *close holes* and *invert surface-normals*. A final down scaling step matches the required glandularity. The resulting height profile – inner structure has the dimensions of 237,6x117,6x6,153mm with a height profile volume = $V_{pattern} = 50047,415mm^3$ – 99,96% of the original Ivy structure in Design A (Figure 23). It has to be noted that Fusion does not support more than 3 decimal numbers in the GUI for scientific notation hence the scaling operation might need a few manual iterations to reach the desired volume.

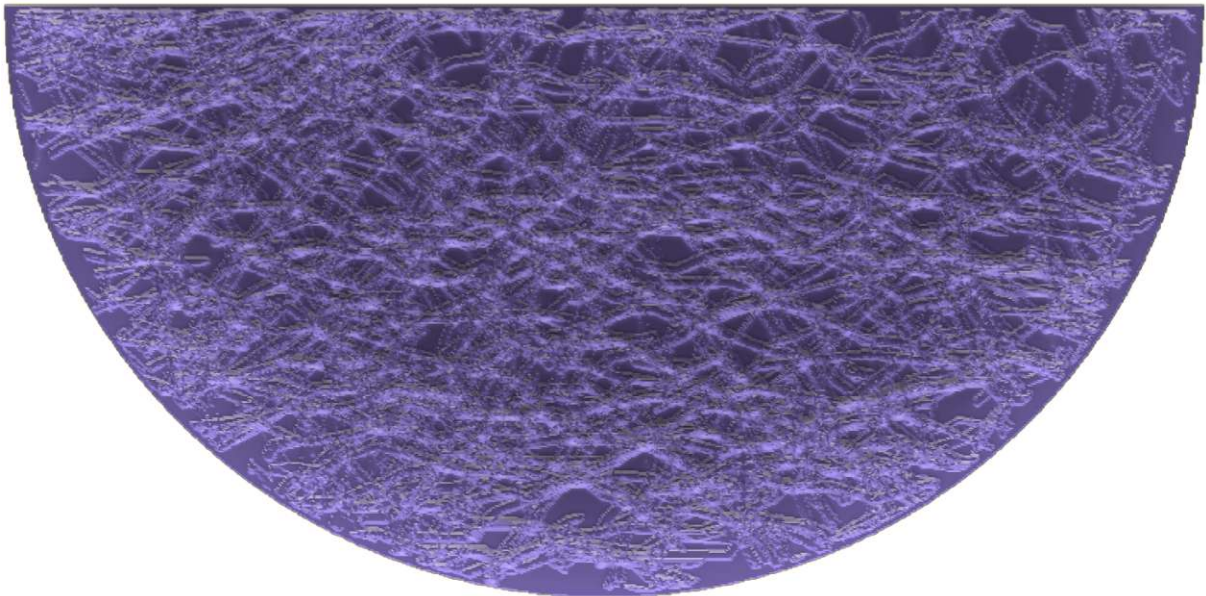


Figure 23: Fusion rendering of the completed height profile based on Design A.

The new height profile is projected once again to determine the amount of resolution loss due to the transformation process. This is done in Blender by positioning the *Camera – object* perpendicular to the height profile mesh (Detailed settings: Figure 25). A couple of *rendering-nodes* need to be set: This is done in *Blender menu: Compositing* (Figure 24). Keeping a 8bit grey level range and selecting *raw* depiction (disabling all automated Blender filters) creates an X-ray image-like depiction of the transformed height profile in form of a depth shading image seen in Figure 26 (see Figure 24 for the *Compositing* Nodes setup).

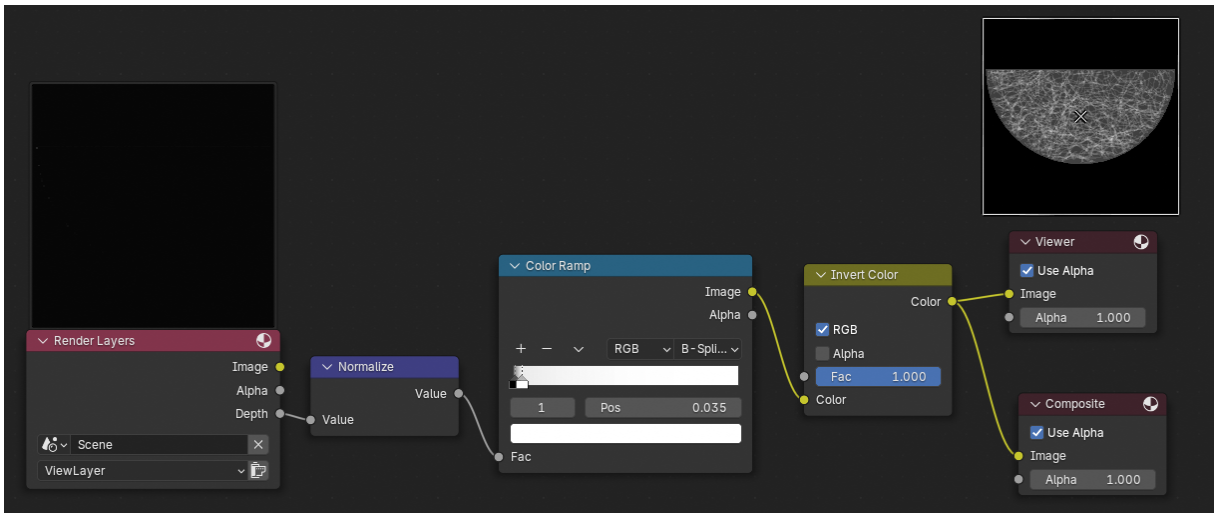


Figure 24: Blender *Compositing* Nodes for the height profile rendering displayed as a depth shading.

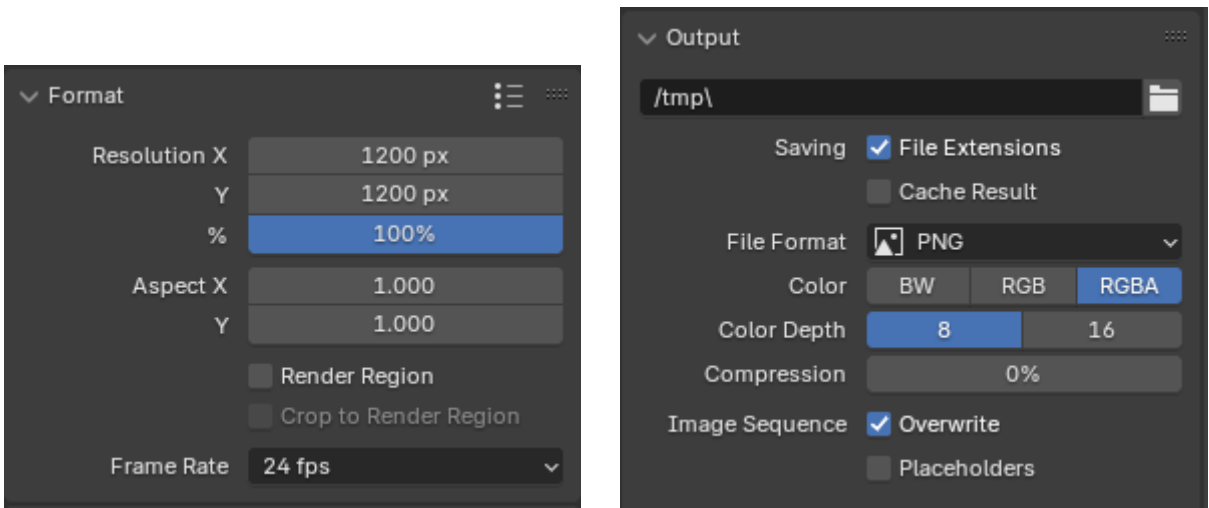


Figure 25: Blender Camera Object Layer Settings for rendering the height profile.

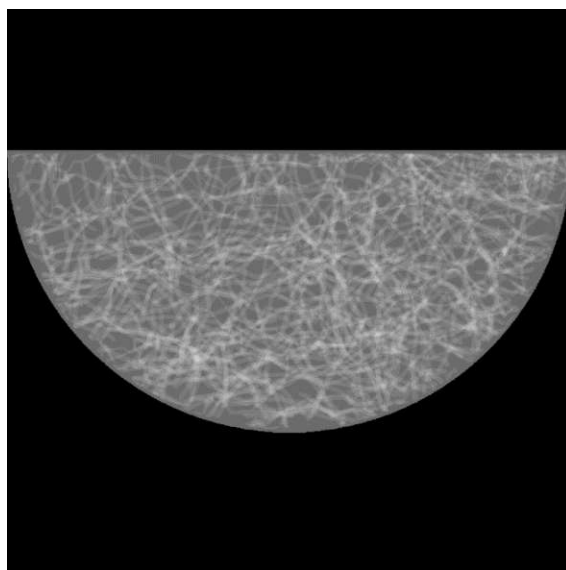


Figure 26: Example of a Blender rendering with height profile: Design A.

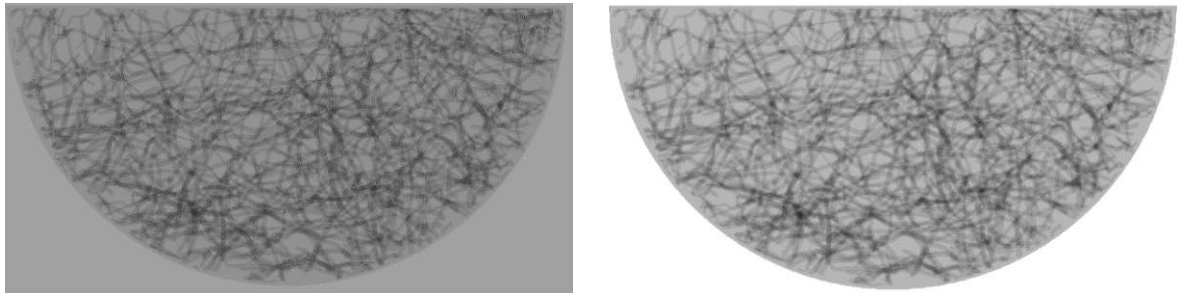


Figure 27: Comparison of mesh projections: **Left:** original Ivy structure Design A. **Right:** Height profile Design A (bottom, colour inverted).

Both projections look identical since a software rendering can capture even the slightest differences in the height profile. However the 3D-printed physical height profile slabs will be limited in terms of depth resolution depending on the 3D printer specifications. Especially SLA printers with a very fine layer height in the range of 0.05mm or below can maintain the spatial resolution of the spikes best.

2.1.3 Phantom 45 Dual Extrusion Alternative Design

In this alteration of Phantom 45, the phantom is created as a full-volume printed slab with the original 3D Ivy structure as the inner structure. No height profile conversion was done here. Also the adipose tissue is mimicked by a linear attenuation fitting filament (ABS), instead of using an adipose tissue-equivalent material to fill up the intermediate space after printing, like in the Phantom 45 height profile design and the CBM phantom. This alternative design keeps the original Ivy structure, but requires the casing, the Ivy structure and the space in between both to be 3 separate mesh files, that can be assigned different materials during 3D-printing. The mesh representing the adipose tissue between the casing and the Ivy structure is realised as an additional slab, that exhibits tunnels and surface holes according to the Ivy structure. It can be interpreted as a negative of the Ivy structure design (Figure 28 Bottom). The splitting of each slab design into three inter-stacked meshes (Casing, Ivy structure, adipose tissue slab) is necessary, because the slicing software is unable to distinguish overlaps between the intermediate-space-filling adipose tissue slab mesh and the Ivy structure mesh at the same printing position. Ignoring this overlap will result in an incorrect deposition of alternating layers of Filament1 (Tough PLA) and Filament2 (ABS) during the print.

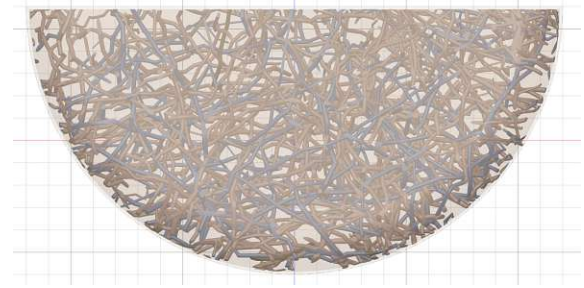
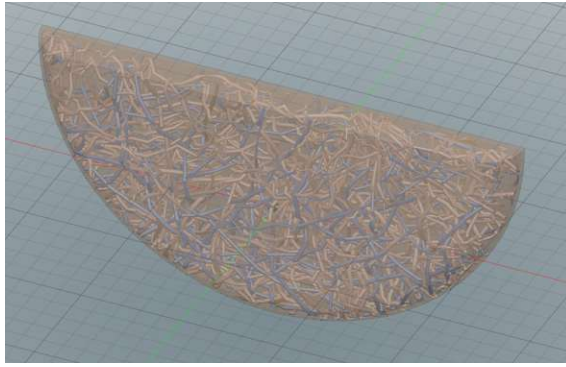
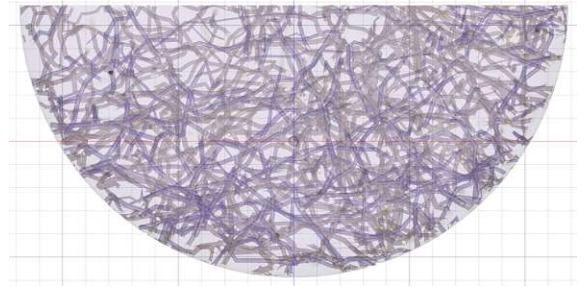


Figure 28: Ivy Structure Design A + Hollow Casing.

Left: Side View.

Right: Front View.

Bottom: Adipose tissue slab filling the intermediate space between casing and Ivy Structure Design A.



2.2 3D printers and printing materials

All realised designs were printed with the *Ultimaker S3* and *FLSUN V400*, both FDM printers. Some experimental prints for Phantom 45 Slab A were conducted with the *Elegoo Saturn 4 Ultra* SLA printer, yet the completed phantom models were merely FDM models. The following is an overview about the principles of FDM and SLA technology with their pros and cons, technical specifications of the printers and the used filaments and resins. Additionally the filling materials for the remaining intermediate space (Paraffin Wax and Coconut Oil) are presented.

FDM (fused deposition modelling) printers use a solid thermoplastic filament, usually with a diameter of 1,75 or 2,85mm, which is wound up on a spool and slowly fed into a *hotend* (=melting chamber) by the *extruder*, all positioned inside the printhead. The filament is melted and then pushed through a metal nozzle onto a printing surface (*print bed*) to form the desired object. The print bed is usually made out of glass, spring steel or carbon, giving different adhesion properties. The extrusion rate is adjustable to meet the desired print quality, and to set the printing speed. Depending on the motion system either the print bed is fixed and the printhead is moving in xyz direction (in case of the V400), or the print bed takes on the

movement in a specific direction during the print. In case of the Ultimaker S3 the print bed moves in z direction (changing height), while the print head is moving in the xy plane.

SLA (stereolithography) solidifies a liquid resin with a set array of LEDs with a specific wavelength (usually in the UV to near-UV spectrum of 355-405nm), that triggers the polymerization process which hardens the resin. The print setup for this technology is built with a so called tank, into which the desired resin is poured. The bottom of the tank is transparent, with an array of UV-LEDs below it. A build plate is submerged into the resin until a specified distance between tank floor and build plate is reached. The very fine layer of resin which is between the tank floor and the build plate is now irradiated with UV light for a set amount of time. In case of masked stereo lithography (MSLA), this hardens a full layer simultaneously. Masked refers to printing a whole layer at once, compared to laser systems which trace one cross sectional pattern of a layer point by point. After each layer the build plate is raised out of the resin and re-submerged for the next layer. This printing method allows for very fine layer heights, which most FDM printers can hardly reach. One of the downsides of this method is that bridges and overhangs are more difficult to print compared to FDM, and that the final print usually requires postprocessing in terms of a tedious cleaning process with isopropanol. Furthermore, an additional light-curing process in terms of post-print radiation in a closed off UV light chamber can be necessary depending on the resin.



Figure 29: FDM Printers Ultimaker S3 (left), V400 by FLSUN (middle). SLA printer Saturn 4 Ultra by Elegoo with a completed print attached to the build plate (right).

Overall both printing methods have their advantages. The decision really depends upon the geometry of the design and the physical requirements the resulting prints should have. This includes transparency, heat resistance, impact resistance, surface texture, but also linear attenuation of X-rays and density in regard to this thesis.

2.2.1 Ultimaker S3

The Ultimaker S3 [49] is a dual extrusion FDM printer, with two printheads, each with separate filament spools. This is especially useful for two component models since the filament switch is much faster compared to single extrusion models. It supports various materials such as PLA, ABS, PETG, Nylon, TPU as well as composites like carbon fibre or glass-filled filaments. The build volume is 230x190x200mm, which allows small to medium sized prints. The standard nozzle size is 0,4mm, but can be switched to bigger nozzle sizes like 0,8mm. Some test prints were conducted with the 0,8mm nozzle, the final prints however were done with 0,4mm. The resolution range covers 20-200 μ m for the 0,4mm nozzle. The maximum print speed is <24mm³/s. The automated bed levelling is a pleasant feature, assuring good first layer adhesion without the need of manual calibration. The print bed is made of glass with heating capacity of 20-140°C. The nozzle temperature range covers 180-280°C. Ultimaker has its own Slicer software: *Ultimaker Cura*.

2.2.2 FLSUN V400

The V400 [66] is a high speed single extrusion printer which can reach up to 400mm/s (updated version up to 600mm/s). It uses 1,75mm filaments and supports the materials: PLA, PLA+, ABS, PETG,WOOD,TPU, PC, NYLON. The print bed is circular, with a maximum print volume of 300x410mm. It uses a 0,4mm nozzle with layer height range 50-300 μ m. The nozzle temperature goes up to 300°C, spring steel print bed up to 110°C (can lead to system reboot due to overheating). It supports auto levelling, but needs fine adjustment which can also be done during the print. The very high printing speed is a big advantage of the V400, drastically reducing printing times, while still maintaining a high precision.

Slicing Software for FDM, Ultimaker Cura: The phantom slab designs were imported as STL files into Ultimaker Cura, a slicing software that converts CAD objects or other arbitrary mesh files into a 3D printer file format. Adjustable print settings in this software are e.g.: printing material (with respective pre-set profiles), nozzle- and print bed temperature, layer height and layer width, print speed, additional print object supports, support blockers, fan cooling, etc. The *slicing* operation creates a set amount of vertical layers into which the print object is divided, depending on the chosen layer height. The thinner the layer height, the higher the resolution, but this also increases print times significantly. A print preview rendering gives a rough idea about the vertical print object segmentation. The sliced object is exported as GCODE file for the printer to read.

2.2.3 Saturn 4 Ultra by Elegoo

The Saturn 4 Ultra [70] is a resin-based masked stereo lithography (MSLA) printer using a 405nm wavelength COB (Chip on Board) light source with Fresnel Collimating Lenses. The layer thickness ranges from 0,01-0,2mm with an accuracy of 0,02mm. The xy resolution is 19*24 μ m. The Saturn 4 Ultra can reach a maximum print speed of 150mm/h, and has a build volume of 218,88x122,88x220mm. Compatible slicing software includes ChituBox and AutoDesk Fusion.

Slicing Software for SLA, ChituBox. Chitubox [71] is a slicing software for SLA printing, with which the relevant parameters of exposure times and resting times can be set. It has a simple GUI and allows to add support structures automatically. It has a wide compatibility with various printers and has fine-tuning exposure settings included which can further enhance print quality.

2.2.4 3D-printing & Slab Filling Materials

The decision on the selected FDM printing materials was based upon the research of Mettievier et al. [57] (see Figure 10). While PETG has a good fit for imitating glandular/skin tissue attenuation around 28keV with a attenuation difference of less than 11,3%, it was also the most

difficult to print, since it requires high temperatures and has a tendency towards stringing and *warping* (shrinking during cooling after deposition due to contractional forces). PLA on the other hand is very beginner friendly and causes hardly any issues, however the respective linear attenuation difference for glandular tissue is generally higher than PETG. ABS poses as a good adipose tissue-imitating material, but also has the issue of potential warping. The warping problem in general depends on several factors such as filament quality, cooling down speed and infill density. Reports inside the 3D FDM community advise closed and heated printing chambers to slow the cooling process and hence reduce the warping issue (see Discussion). SLA resins were only used for experimental prints with Phantom 45 Slab A.

In this work the following printing materials were used:

PLA (poly lactic acid, transparent) by Geetech [72] (FDM): PLA is a semi-crystalline polymer with crystalline (ordered) and amorphous (disordered) regions. PLA is known as a beginner friendly filament with a good transparent look after printing in case the clear version is used. Although not *glassy* like some other specialised filaments, it is suitable for the phantom designs in this thesis in order to see the quality of the inside structure. It is comprised for 3D printers with 1,75mm filament diameter, covers a temperature range of 185-210°C and a print bed temperature of 25-60°C. It showed very good adhesion properties, almost no stringing and no warping was observed during the print. Geetech does not specify the specific temperature parameters or the density, so Heat Deflection Temperature (HDT) was assumed at ~60°C which is typical for PLA filaments. 3D-printing material vendors referenced the Ultimaker PLA with 1,24 g/cm³, which is also assumed for this filament [73].

Tough PLA (White + Grey) by Ultimaker (FDM): Tough PLA has a higher mechanical resistance than the conventional PLA filament, and is comparable to ABS in that regard. The filament diameter is 2,85mm, with a density of 1,22g/cm³ and a Heat Deflection Temperature (HDT) of 58°C/Glass Transition Temperature (T_g) of 59°C. Printing temperature range is 210-220°C, Build plate temperature 60°C. Almost no warping was observed with this filament and

the material compatibility with ABS during a Dual Extrusion print on Ultimaker S3 was very good [73].

HDglass PETG (polyethylene terephthalate glycol, transparent) by FormFutura (FDM):

HDglass is a very clear filament with 90% optical light transmittance. The filament has 2,85mm in diameter and a density of 1.27 g/cm³. Glass transition Temperature lies at 70°C. The printing temperature covers a range of 235-260°C with a bed temperature of 80°C. This filament showed no oozing or stringing, but caused warping across larger thin areas [74].

EasyFil ABS (acrylonitrile butadiene styrene, Grey) by FormFutura (FDM):

A filament with high mechanical strength and HDT up to 85°C. The filament diameter is 2,85mm with a density of 1,05g/cm³. Printing temperature ranges between 230-255° and a print bed temperature of 100°C is advised [75].

ABS-like 3.0 Photopolymer Resin – Translucent by Elegoo (SLA):

This low viscosity resin reacts to 405nm UV light and is defined by Elegoo as a high precision resin, exhibiting low shrinkage. It has high mechanical properties in terms of toughness, strength and impact resistance. Further it is described as a rapid curing resin when exposed to its defined curing wavelength, improving printing efficiency [76].

TR250 LV Grey by Phrozen:

The TR250LV is an acrylate based high heat resistance (100°C) resin with low viscosity and a density of 1,17g/cm³ at 25°C. It further exhibits high mechanical strength and is ideal for prints which must withstand mechanical stresses at high temperatures [77].

Infill materials simulating adipose tissue:

100% Paraffin Wax from melted IKEA candles was used as a filling material for the PETG printed slabs (Phantom 45) in order to mimic adipose tissue. The exact chemical composition in terms of alkane chain length is unknown, however the density and melting temperature is assumed around 0,9- 0,93g/cm³ and 50-57°C [78]. Conventional cooking coconut oil was used

to fill the CBM phantom slabs and mimic adipose tissue. The density for coconut oil was assumed to be 0,9-0,93 g/cm³ but with a melting temperature of 25°C.

2.2.5 FDM Printing Parameters and Processes

This subchapter gives a more detailed explanation about the print settings, especially for the CBM phantom, since its complex design required certain adjustments to be properly printed. Further a thorough explanation about the complicated mesh positioning for the Phantom 45 Dual Extrusion alternative design is provided. Due to the simple design of the common Phantom 45, the relevant parameters are summarised in the table. Please find the table at the end of the subchapter with all print settings for CBM phantom and Phantom 45 and Phantom 45 Dual extrusion alternative design (Table 3: FDM Print Settings).

The CBM phantom was printed on the FLSUN V400 with the Transparent PLA (Geeetech) filament. Layer height was set to 0,2mm, which is a compromise between quality and printing time. Cura Slicer automatically sets the initial layer height to 0,3mm for the first layer to improve adhesion. The line width was set to 0,4mm to meet the nozzle diameter, which was also applied to all other line widths (walls, infill). The line width also influences the wall thickness of the slab design, since a manifold of the line width is necessary to avoid overlaps, which can lead to a heterogeneous wall structure along the object height. The infill density was set to 100% with the “grid” pattern. Printing temperature for GeeTech Transparent PLA was set to 200°C with a print bed temperature of 60°C. Print bed temperature directly influences the adhesion of the first layer and should be in the range of 55-60°C for PLA in general. The main print speed was set to 200mm/s. All other print speeds (walls, infills, support, etc.) are automatically adjusted by Cura Slicer. Retraction (pulling back the filament from the melting chamber) is enabled and the default settings were used. This parameter is only important to reduce potential oozing, but due to the high print speed and material composition this is not an issue for PLA. Cooling is set to default with 100% fan speed.

Support: Since the slabs were printed in an upside down position, and the inside structure does not align with the outer circumference at the bottom, only the slab casing touches the print bed, while the inner structure would float without support from below. Therefore a support structure is created but only for the first few layers, since otherwise this would result in additional unwanted structures throughout the whole phantom slab. Unfortunately Cura Slicer does not offer the possibility to restrict a support structure after a certain layer height, hence a workaround has to be implemented by adding a *support blocker* (Figure 30 left).

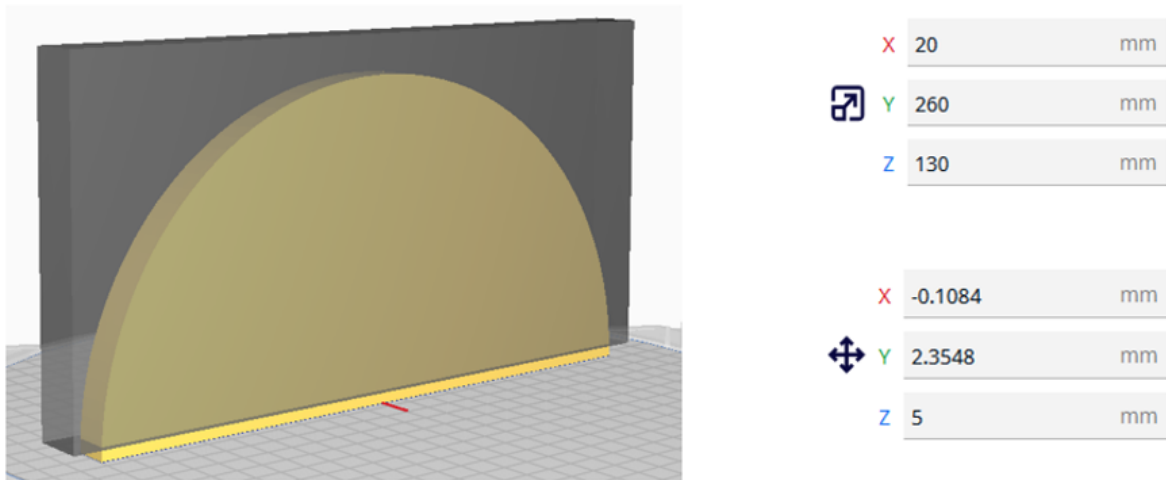


Figure 30: **Left:** Support Blocker set over Slab #2.

Top right: Support Blocker scaling parameters

Bottom right: Support Blocker positioning.

The support blocker has to cover the object completely and must be elevated to the desired height (z coordinate in mm, Figure 30, Bottom right). Since the print preview only displays the layer number, one has to calculate the appropriate z distance from the bottom manually by taking the initial layer height (0,3mm) + (layer number where the inner structure begins -1)*layer height (0,4mm). For Slab #2 this results in 3,9mm, however it is advised to create a little overlap between the first few millimetres of the inner slab structure and the support. This will improve the printability of the initial inner structure branches (see Figure 32).

The blue outline showing in Figure 31 and Figure 32 is the *Brim*, which provides additional adhesion to the print bed. Brim line count was set to 20. It is possible to keep the default settings of 12 outlines, however it is advised to increase the number to 20, because it will offer more

area to add optional duct tape stripes in order to fix the whole print firmer to the print bed (see *Print refinement* in Discussion).

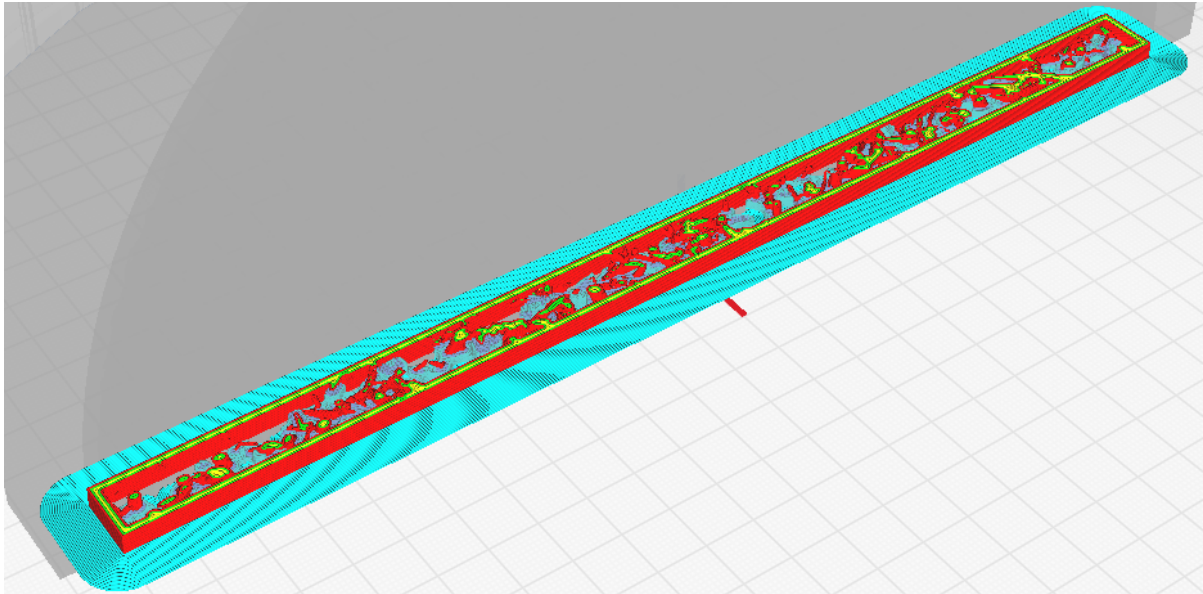


Figure 31: Cura Slicer print preview until layer 11. Support structure (blue & violet structure inside the casing)+ Brim (blue outline) for additional adhesion.

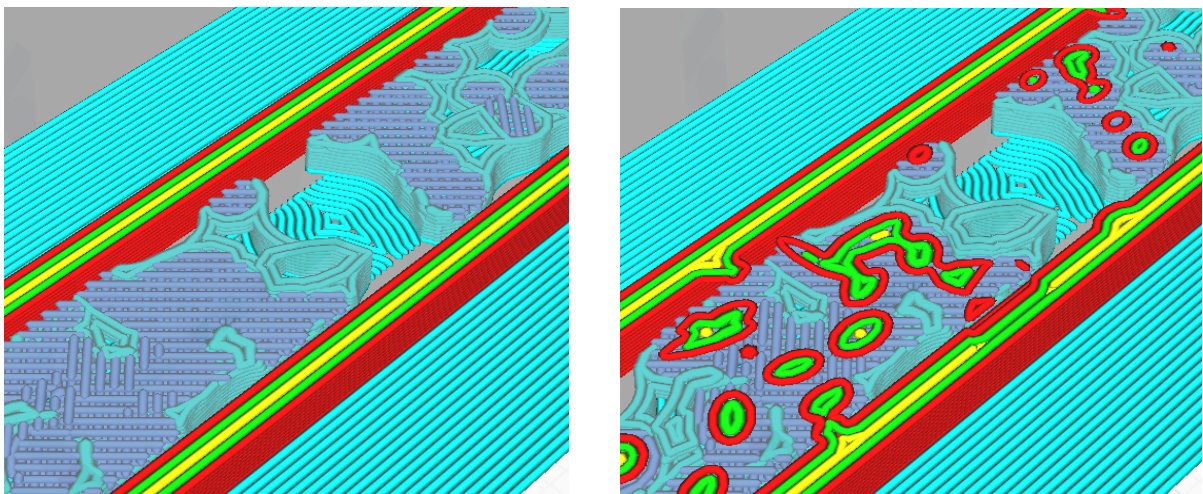


Figure 32: **Left:** Support structure on Slab #2 until Layer 10 (height: 3,9mm).

Right: First inner structure layer 11. The violet waffle structure is the support infill.

Notes for the Dual Extrusion Print of Phantom 45 alternative Design

The printability of both materials onto each other was checked via a test cube of Tough PLA enclosing three shapes printed with ABS: a big sphere, a small sphere and a cube (Figure 33). All bodies have 100% infill density. The X-ray-print-preview (Figure 33 right) of the slicer software shows the arrangement from the rear. By selecting the respective extruder, either the longitudinal cube-housing with the negative cut out for the spheres or cube is shown (extruder 1 – Tough PLA, representative for the casing and the glandular tissue of the phantom, Figure 34 Left), or the spheres and the cube are shown in the preview (extruder 2 – ABS, used for the adipose tissue slab with the negative cut out for the glandular tissue, Figure 34 Right). Figure 35 shows an X-ray image of the test cube taken with 28kVp, 111mA, 56mAs and AEC (automatic exposure control) enabled. It shows a good contrast between the casing (Tough PLA) and the 3 inserted test objects (ABS). The dark areas towards the respective centre, for both the cube and the 3 objects are beam hardening artifacts, which have not been corrected. Since this is a raw image, no postprocessing and correction algorithms have been applied at all. The print density for each material is constant.

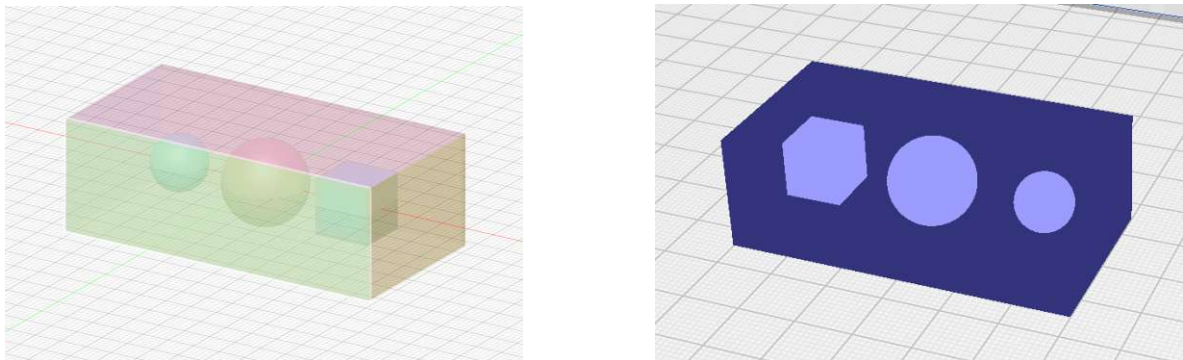


Figure 33: **Left:** Test cube for dual extrusion print Tough PLA/ABS.

Right: X-ray print preview.

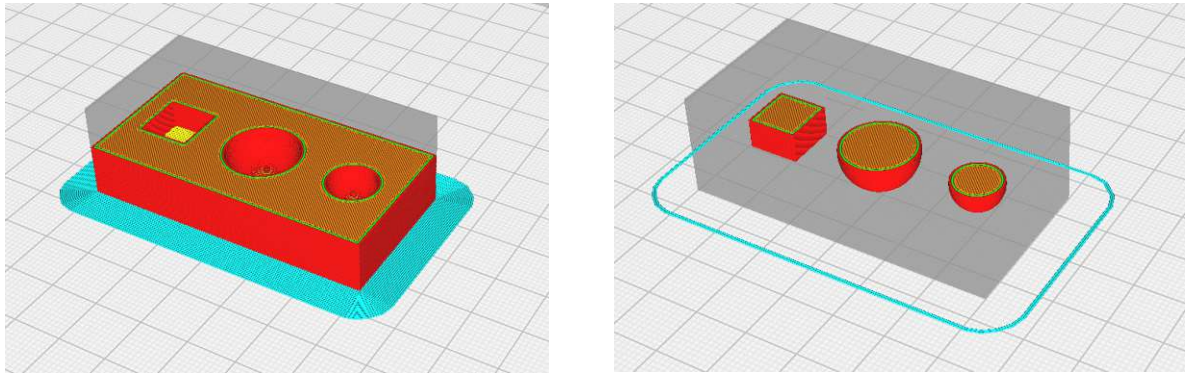


Figure 34: **Left:** Test cube with negative cut outs for 2 test spheres and 1 cube - Printed with Tough PLA.
Right: Test-spheres/cube - printed with ABS

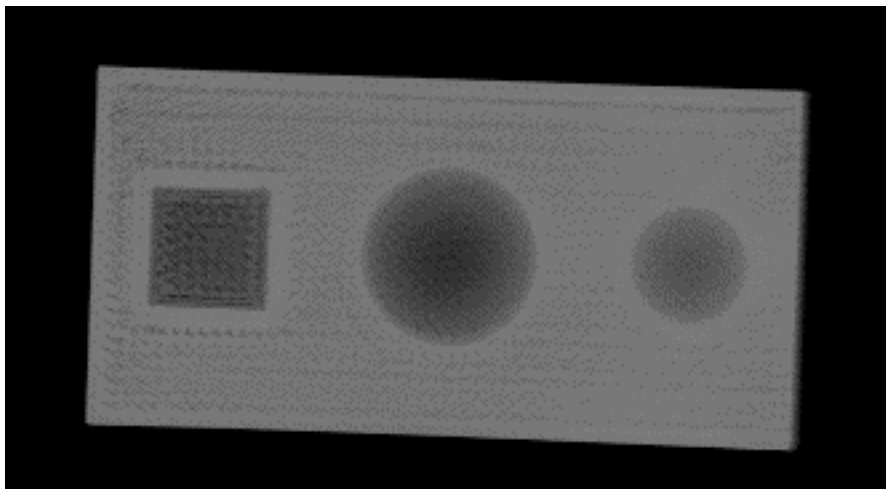


Figure 35: 3D-Printed Test Cube of Tough PLA (casing), and ABS (inserted objects), X-ray Image at 111mA, 28kVp, 56mAs. The fine dotted lines that form this grid structure are unwanted air gaps between adjacent filament layers. See Discussion for further elaboration.

Phantom 45 Dual Extrusion Alternative Design – Mesh positioning: When importing the 3 separated STL files (Casing mesh, Ivy structure mesh, adipose tissue mesh) into Cura Slicer it is important to check for the correct orientation and no overlap of all 3 meshes. The meshes have to be rotated diagonally to fit the print volume of the Ultimaker S3. The Ivy structure mesh and the adipose tissue slab have to be elevated manually by 1,2 mm in the Z-direction, since the slicer software does not take the supporting nature of the hollow casing-mesh into account and forces the meshes down to the print bed (disable “Drop Down Model” in the left side menu).

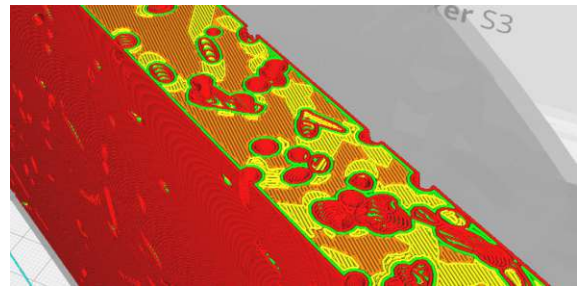
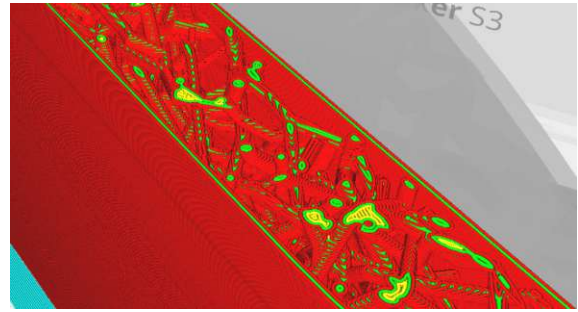
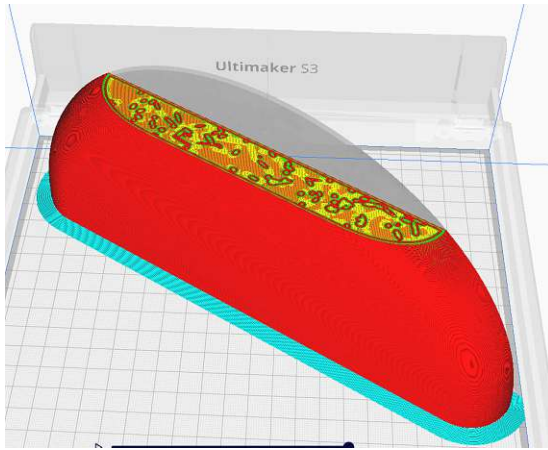


Figure 36: Print preview of Phantom45 Dual Extrusion print Slab A with 3 separate meshes in Cura slicer.

Left: Combined view of an arbitrary layer with Casing mesh, Ivy structure mesh and intermediate adipose tissue slab mesh.

Right: Casing mesh & Ivy structure mesh visible.

Bottom: Intermediate adipose tissue slab mesh visible.

A layer height of 0,3mm, 100% infill and a print speed of 45mm/s (PLA with 215°C) and 60mm/s (ABS with 245°C) results in a print time of 1 day and 20hours 45min. This includes a prime tower to ensure a clean filament change and prevent potential oozing by residual filament-wipe off on the inactive nozzle.

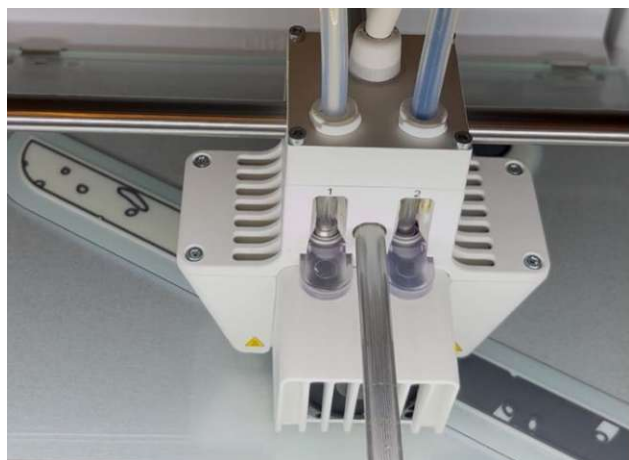


Figure 37: Dual Extrusion print of Phantom45 in progress

Table 3: FDM Print Settings

Phantom Design	CBM	45	45 Dual Extrusio
Printer	FLSUN V400	Ultimaker S3	Ultimaker S3
Filament	PLA (transparent) Geeetech	PETG HD Glass FormFutura	Tough PLA + ABS
Nozzle[mm]	0,4	0,4	0,4
Layer Height[mm]	0,2	0,2	0,2
Initial Layer Height[mm]	0,3	0,3	0,3
Layer Width[mm]	0,4	0,4	0,4
Infill[%]	100	100	100
Infill Pattern	Grid	Grid	Lines
Print Temperature[°C]	200	245	215/245
Build Plate (=print bed) T [°C]	60	80	60
Print Speed [mm/s]	200	50	45/60
Extrusion rate [%]	100	100	100
Cooling [%]	100	0 (off)	100
Support	Yes (see description)	No	No
Build Plate Adhesion	Brim (20 lines)	Brim (9 lines)	Brim(18)
Additional settings	Support Blocker	No	Prime Tower (default)

2.2.6 SLA Printing Parameters

The optimal print settings for the respective resin was tested via printing a so-called *validation matrix* first [79] (Figure 38). This is a thin plate with very fine features, that become more or less defined depending on the Bottom Exposure time and (Normal Layer) Exposure time.

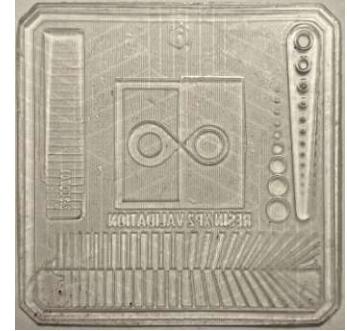


Figure 38: Validation Matrix

Table 4: SLA Print Settings

Resin	ABS-like 3.0	TR250
Layer Height[mm]	0,05	0,05
Bottom Layer Count	5	5
Exposure Time[s]	2,2	1,5
Bottom Exposure Time[s]	25	20
Transition Layer Count	5	5
Transition Type	Linear	Linear
Transition Layer Interval Time difference[s]	2,97	3,08
Waiting Mode During Printing	Resting time	Resting time
Rest Time Before Release[s]	0,2	0,2
Rest Time After Release[s]	0	0
Rest Time After Retract[s]	0,5	1

2.3 Filling process

After the print the remaining intermediate space of the slabs was filled up with coconut oil for the CBM Phantom and paraffin wax for Phantom 45. This should imitate the adipose tissue during a mammography scan. Due to the complicated inner structure and the low softening temperature of the printing material (PLA ~58°C) in the CBM Phantom, coconut oil with a low

melting temperature of 25°C was preferred over paraffin wax (melting Temperature ~57°C), avoiding the risk of destroying the inner structure. Furthermore, trapped air bubbles and potential clogging during the filling process was anticipated with paraffin wax in combination with the CBM phantom.

Phantom 45: For filling the Phantom 45 slabs, conventional IKEA candles (100% paraffin wax) were melted inside a heat resistant measuring cup at 80°C in a dry-air oven until they were fully liquid. The first filling was ~80% of the slab volume. After a short waiting time the wax temperature was assumed to have cooled down to at least the glass transition temperature of the HDglass PETG material (70°C). Further it was assumed that the solidification process would be fast enough to not alter the inside structure and the casing shape. After half an hour the process was repeated since the wax had shrunk and left air pockets and an airgap between solidified wax and casing. The slabs were left in upright position over night. The next morning the slabs were reheated twice in the oven for the wax to become soft again and automatically fill out remaining air pockets. Due to the positioning of the filling hole in the slab design, the slabs could not be filled all the way to the top.

CBM Phantom: The coconut oil was put in a water bath and slowly heated until being fully liquid. In the meanwhile the CBM Phantom slabs had three holes drilled through the remaining support structure on the semi-open chestwall side, to have infill holes with a sufficient diameter available. The holes were drilled in three steps, increasing the drill diameter from 4 to 5 to 7mm each time. The successive diameter increase was done to spare the inner structure from unnecessary destruction by sudden torque of a big drill bit (slab thickness: 13,3mm, final drill bit diameter: 7mm). Drilling depth was ~5mm. A small funnel with a squeezed liner attached to the neck was used to fill the phantoms very slowly. Between the heating and filling process the coconut oil temperature was repeatedly measured with a two-metal wire sensor stuck into the oil, until it reached 50°C (PLA softening temperature is 58°C). During the filling of each slab all three drilled holes were used to evenly fill in the oil. Most air bubbles could be removed by knocking carefully on the Topside/Bottomside of the casing. The slabs were filled until the coconut oil flowed over to counteract the volume shrinkage during cooling overnight. On the

next day the slabs were cleaned of residual oil sticking to the surface. The remaining semi-open chestwall side was sealed by applying several layers of melted 100% paraffin wax with a brush. The hardened residual wax was cut off clean along the edges with a Stanley knife. All phantom slabs were then put into a refrigerator at 5°C, and wrapped in newspaper to prevent the coconut oil from becoming liquid again (25°C). The transport between the refrigerator and mammography system was always done with an isolated bag with a cooling element inside.

2.4 Visualisation and Projection tools

All calculation, projection and rendering tools were either used in Fusion and Blender or are python based, written in PyCharm 2024.1.14 Professional Edition (Academic Licence) [80].

The relevant file packages include:

- **numpy** (numerical calculations, arrays & matrices)
- **pyvista** (3D visualisation, and data analysis – good for point clouds, meshes/.STL, volumetric data)
- **tkinter** (for the GUI interface)
- **VTK** (visualisation tool kit)

The base code was assembled verbally via *OPENAI-ChatGPT* [81] and then individually altered by hand to meet the specific requirement.

STL Projection Rendering tool: The *STL Projection Rendering* tool was created to get either an orthographic projection of the Ivy Structure designs from Fusion and Blender. These orthographic projections were used to compare the image quality of the resulting FFD/DBT images (see Results). It poses as a simple rendering tool to project the 3D mesh-models as 2D super imposed projections, but it is not a volumetric projection software that uses ray-tracing methods or applies virtual attenuation data to a voxelized mesh (Figure 39). It contains input fields to load the STL files, one output field (for saving), and options for resolution and DPI. A preview is automatically created after pressing: *Bild rendern und speichern (Render and save)*. The opacity for all projected Ivy Structure meshes was set to 4% (0.04).

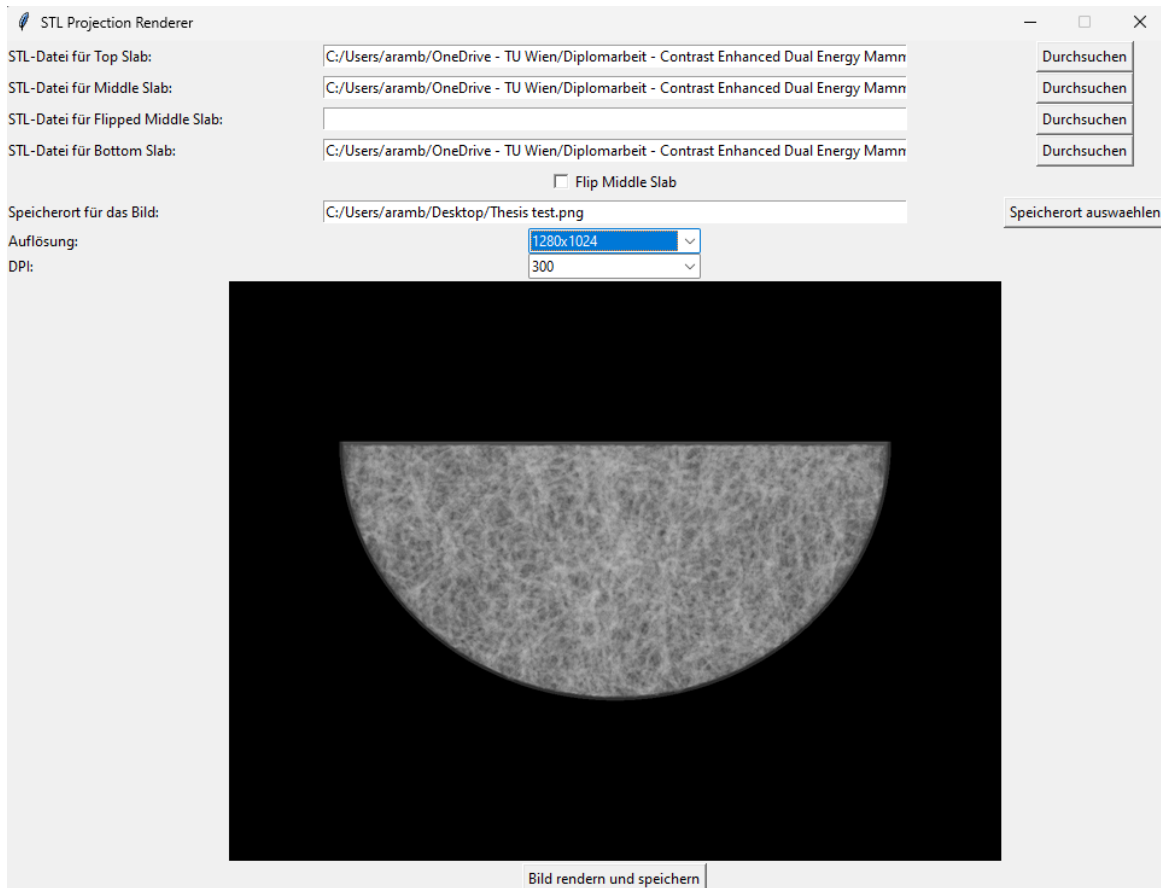


Figure 39: STL Renderer GUI with preview: Orthographic projection of the assembled CBM Phantom.

For dividing the individual renderings and FFD/DBT images into quadrants in the Design & Imaging Results chapter, the online tool: *PineTools Split-Image* was used [82].

2.5 Imaging systems and settings

All phantom images were acquired on a *Siemens Healthcare* [3] – *Mammomat Revelation* (SerialID:10159), with the help of Prof. DDr. Johann Hummel at the *Universitätsklinik für Radiologie und Nuklearmedizin Wien*. The FFD images were taken at CC (Cranio Caudal) standard view, with a tube voltage of 27kVp for the CBM phantom images and 28kVp for Phantom 45 with a Tungsten and Rhodium anode/filter combination (W/Rh). Automatic Exposure Control was enabled. A DBT for the assembled CBM phantom was done with 28kVp, 72mA and an exposure of 4mAs. The phantom thickness was 40 and 45mm for CBM and Phantom 45 respectively. The distance between source and detector was 656mm. The rectangular detector consists of a 3482x2682 (rows x columns) grid with a physical detector

element spacing of $85\mu\text{m}$ (in this case also the pixel size). Below is an exemplary image of the compressed CBM phantom mounted on the Mammomat.

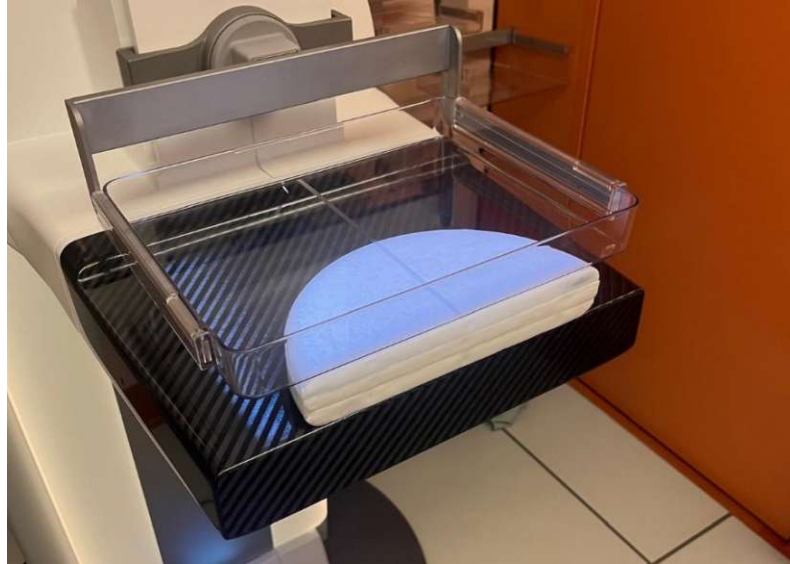


Figure 40: Assembled CBM Phantom in compressed state during image acquisition on the Siemens Healthcare Mammomat Revelation.

3 Results

3.1 Printing & Filling Results

3.1.1 CBM Phantom Slabs

All three printed slabs resulted with straight surfaces and no warping was observed. Top and Bottomside were smooth after scrapping off residual PLA pieces for all slabs. The individual layers were only slightly noticeable by hand. The chestwall-side was even and fully closed with paraffin wax layers (Figure 41 Top Right). The drill holes for the filling process were still visible but also closed tight with wax. After the filling with Coconut oil and cooling overnight, some hardened oil was visible on the Top and Bottom side of the slabs as fine horizontal layers that were scrapped off with a Stanley knife. Whether this was overflowing oil from the filling process or oil penetrating the PLA layers overnight could not be determined.



Figure 41: **Top Left:** Assembled CBM phantom. Assembly order top to bottom: Slab#1.,Slab #2, Slab #3.
Top Right: Chestwall side with visible drill holes.
Bottom: Frontside view with no visible air gaps between the slabs.



Figure 42: Individual CBM slabs. Order from top to bottom: Slab #1, Slab #2, Slab #3..

Left: Topside View.

Right: Bottomside View.

3.1.2 Phantom 45 Slabs

The Topside of the print was bent for Slab A and Slab C which is attributed to warping during the cooling of the print (Figure 43 Top Right). The Bottomside of the slab, with the height profile printed on the inside, was completely straight for both slabs. For the first printed slab (Slab A) the Bottomside showed a lot of residual PETG and unevenly distributed extra filament hanging off. The ripples of the individual layers were noticeable by hand across the surfaces. After postprocessing by scrapping off residual printing material with a Stanley knife and polishing with sanding paper the surfaces became smoother. The Bottomside of Slab C had almost no residual printing material. The closed chestwall side was very smooth and transparent, almost glass like. The Top and Bottomside were translucent before the filling. The Bottomside of the print was transparent enough to make out the defined height profile pattern before the wax filling. Pattern visibility also remained for the first few mm after the filling process (Figure 43 Bottom Right). Due to the position and angle of the designed filling hole on the Frontside of the slabs, a complete filling with wax was not possible without pouring a significant amount of wax on the outer surface. After the filling, the Topside of the slabs were further bent because the shrinking wax dragged the surfaces towards the centre. The Bottomside was also slightly bent inwards. This however is attributed to softening of the material by the liquid wax. In stacked formation air gaps are present between the slabs due to the slight bending after filling and residual PETG accumulations on the casings which were too solidified to be properly removed (Figure 43 Middle Right). Slab B (structure plate) showed warping on the chestwall side, being elevated at the corners (Figure 43 Bottom left). Additionally the surface had a homogenous grid pattern. The designed drill holes for potential platelet-inserts were slightly smaller in diameter. The circumference was even but the holes had a rounded bottom plane.

The Dual extrusion print of Phantom 45 Alternative Design failed due to massive warping and was ultimately not repeated. For printing issues please see Discussion.



Figure 43: **Top Left:** Assembled Phantom 45.

Top Right: Slab A with bent Topside (blue arrow)

Middle Left: Assembled Phantom 45 Frontside view. Stacking order: Slab A, Slab B, Slab C

Middle Right: Chestwall side with visible air gaps in stacked formation.

Bottom Left: Slab B (structure plate) with grid pattern and drill holes.

Bottom Right: Slab A Bottomside view with visible height profile pattern at the edges after wax filling.

Experimental SLA Prints of Phantom 45 Slab A

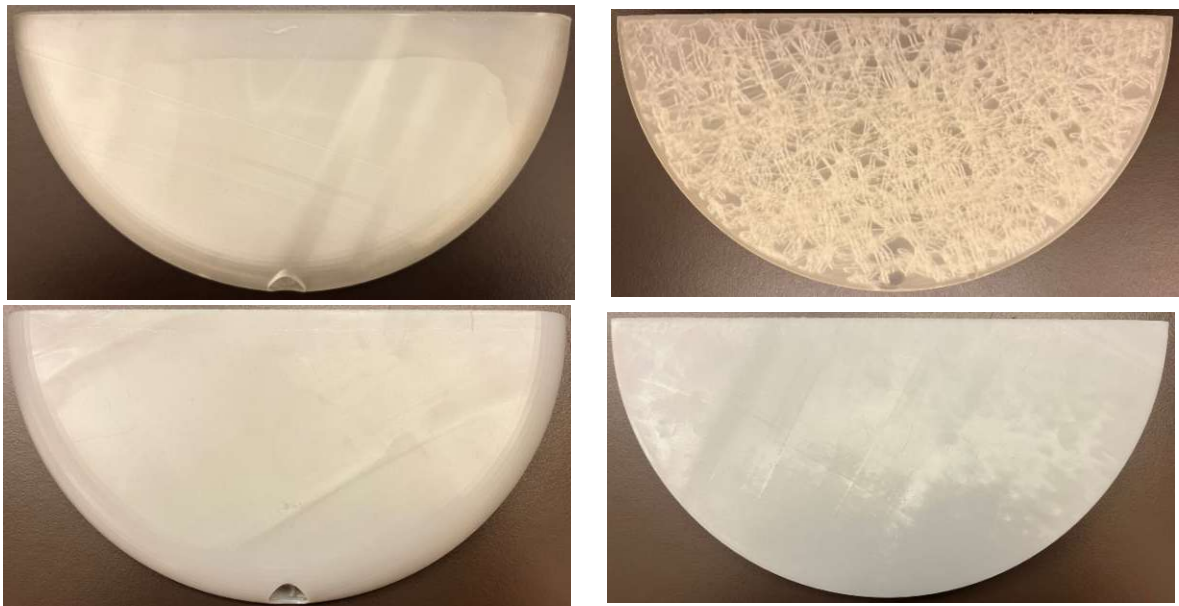


Figure 44: Topside (left) and Bottomside (right) of Slab A.

Top: Slab A printed with transparent ABS-like Resin 3.0 by Elegoo.

Bottom: Slab A printed with TR250 by Phrozen.

Phantom 45 Slab A printed with ABS like resin 3.0 exhibited a smooth surface and excellent transparency (Figure 44 Top). The Topside was slightly bent. Phantom 45 Slab A printed with TR250 exhibited smooth and plane surfaces on all sides (Figure 44 Bottom). Both slabs were rinsed repeatedly with isopropanol and were additionally cured with a 395nm UV pocket torch. Due to an issue during the wax filling process the experimental SLA printed slabs were not put up for imaging.

3.2 Design & Imaging Results

The interesting image criteria in qualitative comparison between the orthographic projections of the designs and the mammography images are the contrast differences and pattern visibility. The orthographic projections of the designs are simple super impositions of the design meshes, without considering any linear attenuation or density differences. However they allow for the comparison of fine features and overall pattern visibility of the realized and imaged prints. X-ray images of each assembled (stacked) phantom design and the individual slab components were taken with the previously presented mammography settings. The stacked CBM phantom was additionally imaged as DBT with 26 images, and reconstructed as 41 slices. Please find the respective pairings of (CAD) Fusion rendering (left), orthographic projections (right) and the X-ray images(bottom) on the following pages. Each page is dedicated to one phantom slab, or the respective phantom in assembled formation. All images were viewed and converted from DICOM (16bit) to PNG (8bit) with *microDicom* [83]. The dark areas inside the phantom slabs indicate trapped air bubbles that remained during the filling with paraffin wax/coconut oil for the Phantom 45 and CBM phantom respectively. The contrast between the printing materials simulating the glandular tissue (PETG/PLA) and the paraffin wax/coconut oil imitating the adipose tissue is strong enough to make out fine details.

3.2.1 CBM Phantom Images

In this subchapter the Fusion rendering, its orthographic projection and the corresponding FFDM image will be compared next to each other. A visual pattern matching and rough structural analysis between the orthographic projection and the FFDM image shall portray the accuracy of the resulted prints in comparison to the initial CAD Design. The visibility of fine and complex features as well as horizontal (*bridge*) structures are of great interest considering the inside structure. This will indicate the lower limits of printability considering resolution and the level of complexity the printers can realize. Each slab will be analysed individually as well as the CBM phantom in full assembly. The assembled phantom will further have a DBT slice evaluated.

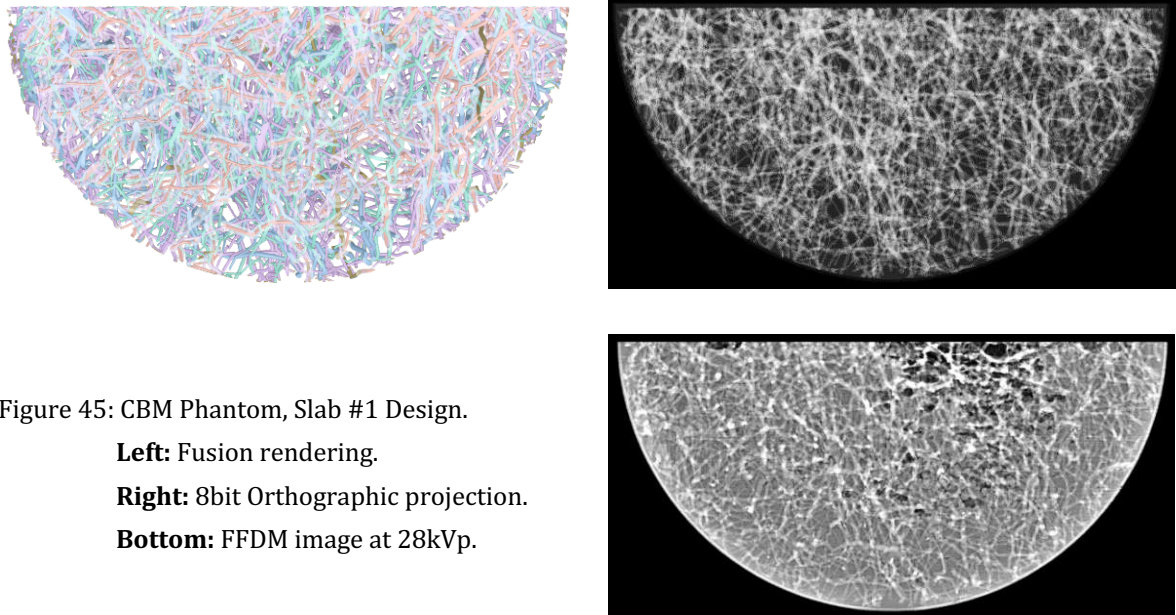


Figure 45: CBM Phantom, Slab #1 Design.

Left: Fusion rendering.

Right: 8bit Orthographic projection.

Bottom: FFDM image at 28kVp.

Slab #1 holds a glandular structure (inner structure) volume of 59698mm^3 and is a combination of 5 individual Ivy Structures, represented by the individual colours in the Fusion rendering in Figure 45 (left). The FFDM image (Figure 45 bottom) was acquired at 27kVp , with 140mA tube current and 71mAs exposure (= tube load). The contrast between PLA and the coconut oil is strong enough to distinguish the individual structure elements. Visually the FFDM image shows a good overall pattern match with the 8bit orthographic projection (Figure 45 right) of the Fusion rendering. In the upper half of the slab the network gets denser and is difficult to evaluate by eye. Black areas in the FFDM image imply air pockets, and are visible especially in the 2nd quadrant (Figure 46 bottom). The 1st and 2nd quadrant show distinct features from the drill holes, which have not been properly sealed with wax after the filling process (Figure 46 red). The white rim along the curvature slightly fading towards the centre is caused by the rounded edge of the slab. A closer analysis of the 3rd and 4th quadrant shows that very fine details could be realised, even with 90° over hangs and bridge-structures without support (Figure 47 green). Even complex areas like intersections where many structure paths meet seem very well realized and can be found in both the orthographic projection and the FFDM image. In Figure 47 (4th quadrant, pink) a fine feature was not realized that is visible in the orthographic projection.

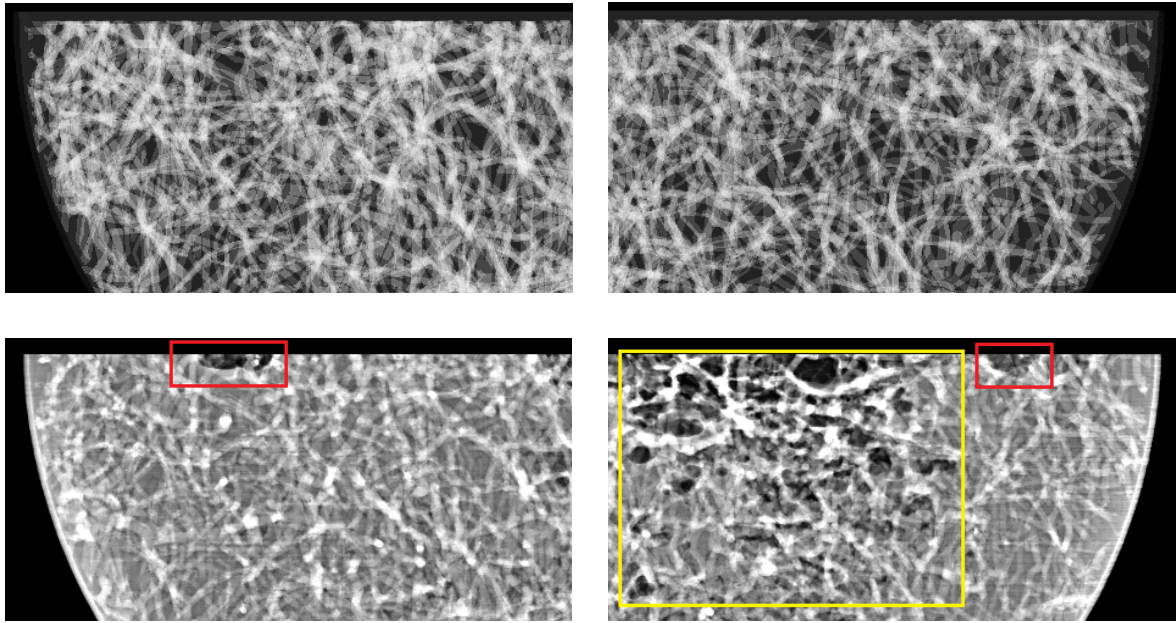


Figure 46: Slab#1: 1st (left) and 2nd (right) quadrant comparison.

Top: 8bit orthographic projection.

Bottom: FFDM image. The red markings indicate drill holes which were not properly filled. Yellow shows several air pockets.

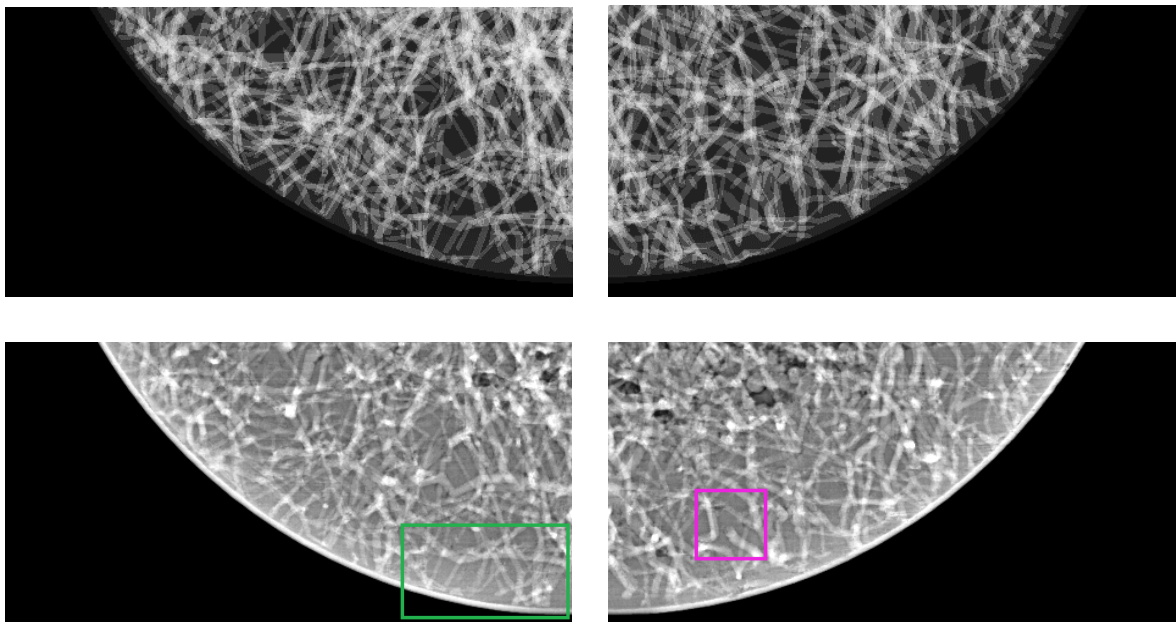


Figure 47: Slab#1: 3rd and 4th quadrant comparison.

Top: 8bit orthographic projection.

Bottom: FFDM image. Green shows very fine details that were realized and horizontal structures. Pink shows a feature that is visible in the orthographic projection but missing in the FFDM image.

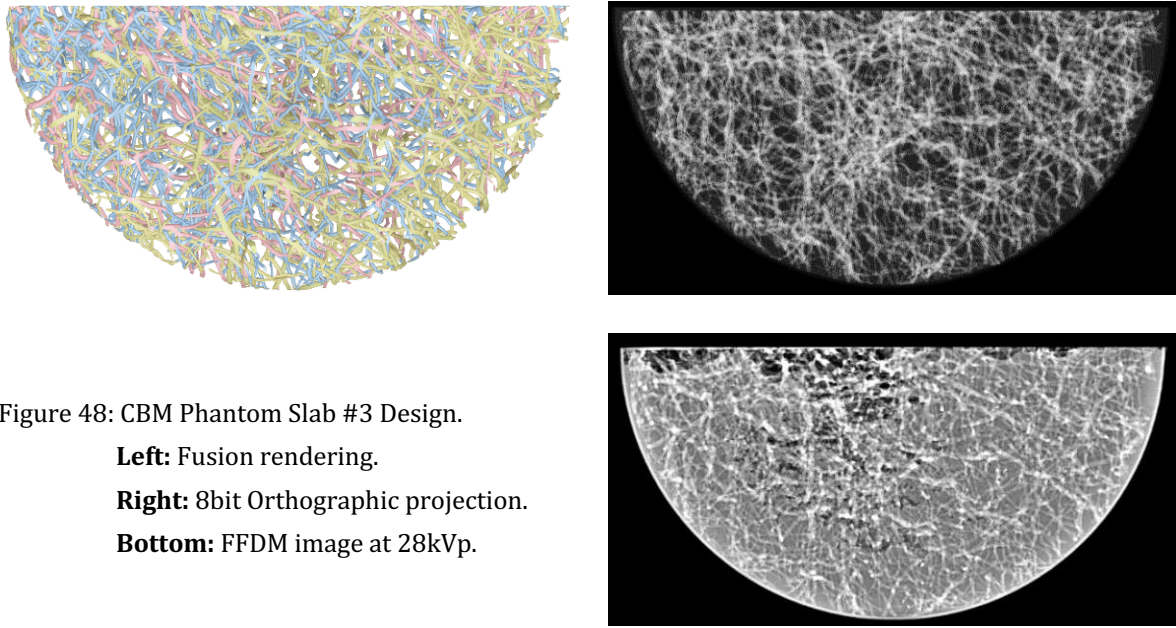


Figure 48: CBM Phantom Slab #3 Design.

Left: Fusion rendering.

Right: 8bit Orthographic projection.

Bottom: FFDM image at 28kVp.

Slab #3 has a glandular structure volume of 58932mm^3 and is a combination of 4 individual Ivy Structures (Figure 48 left). The FFDM image (Figure 48 bottom) was acquired at 27kVp, with 140mA tube current and 71mAs exposure. The very dense areas especially in the centre cannot be evaluated visually due to their complexity, but also due to the amount of air pockets. The curvature exhibits the same white rim with the fade effect towards the centre as was visible in Slab #1. The structures in the lower half and the right side of the upper half (2nd quadrant) show a very consistent contrast between PLA and coconut oil. The black spots around the centre and especially in the 1st quadrant indicate air pockets (Figure 49 yellow). Further two adjacent drill holes in the 2nd quadrant are also visible as two dark spots (Figure 49 red). Near the edge of the slab in the 2nd quadrant, the FFDM image exhibits a very bright feature that appears as fine intersections of lines in the orthographic projection (Figure 49 pink). This might indicate a conglomeration of PLA filament and point out a printing limitation in terms of spatial resolution. Also with Slab #3 the FFDM image shows very fine details realized. The FFDM image in the 4th quadrant exhibits a very fine pattern that was well realized by the printer (Figure 50 green).

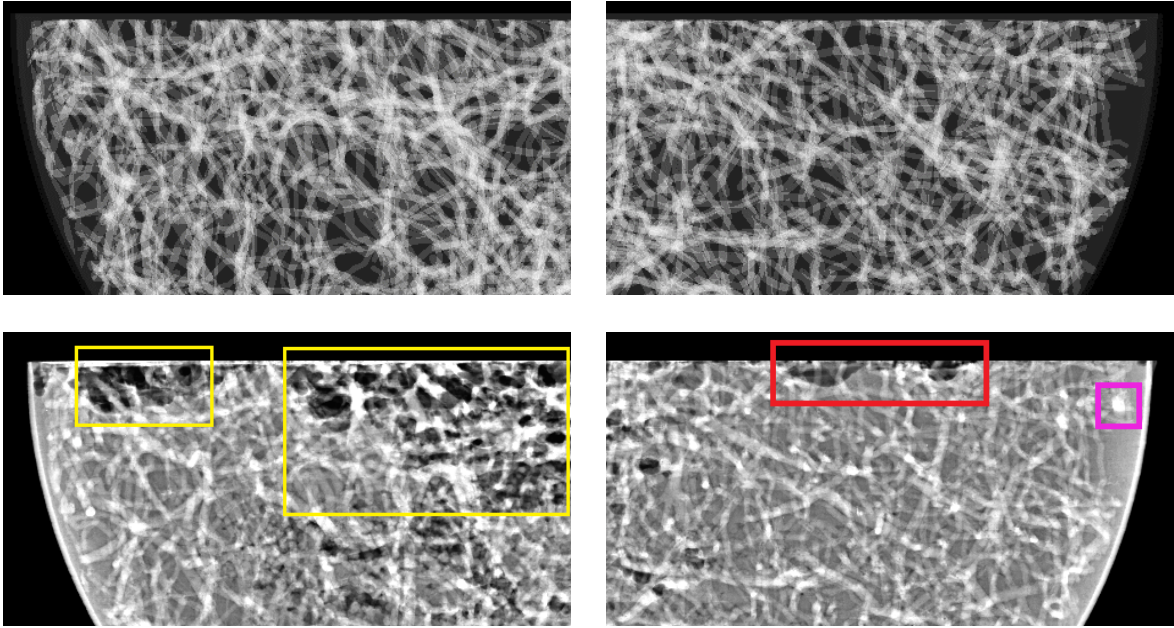


Figure 49: Slab#3: 1st (left) and 2nd (right) quadrant comparison.

Top: 8bit orthographic projection.

Bottom: FFDM image. In the 3rd quadrant (yellow) air pockets are visible. The 4th quadrant (red) shows two adjacent drill holes that have not been properly sealed with wax. Pink shows a very bright feature not represented in the orthographic projection.

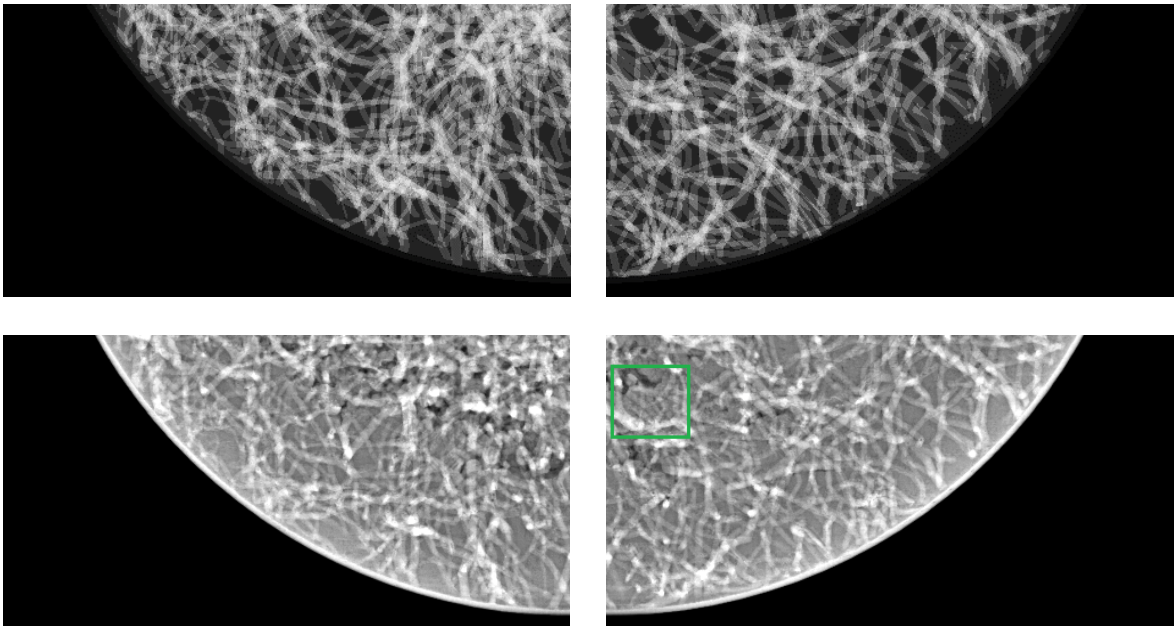


Figure 50: Slab#3: 3rd (left) and 4th (right) quadrant comparison.

Top: 8bit orthographic projection.

Bottom: FFDM image. The 4th quadrant shows several very fine parallel lines which get intersected by another line. The same detail can be found in the orthographic projection.

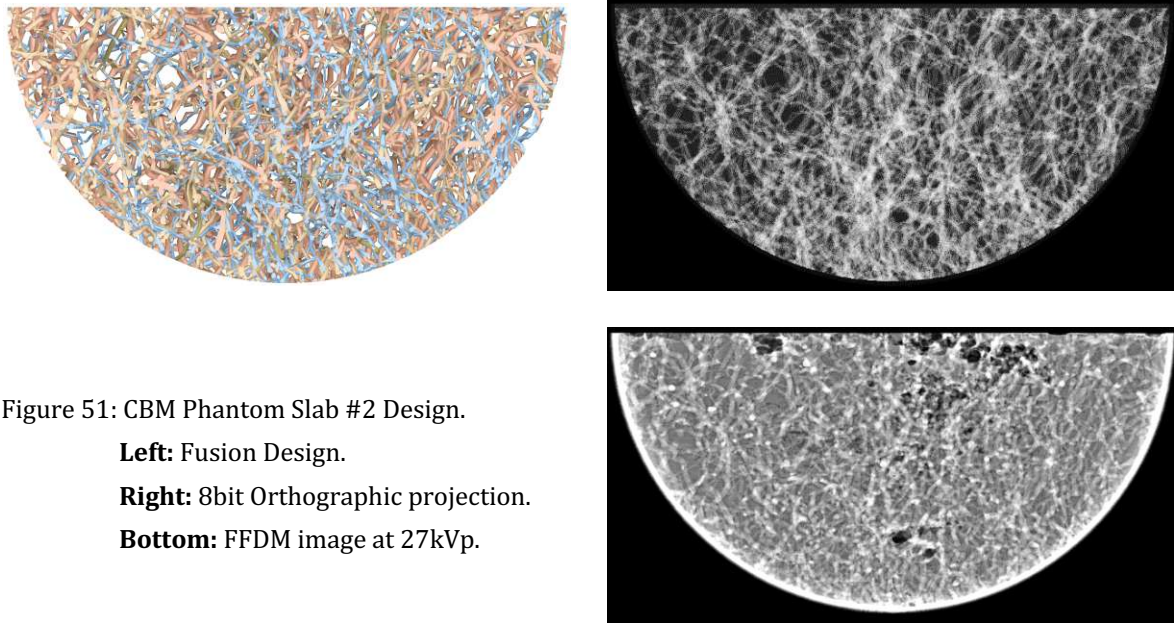


Figure 51: CBM Phantom Slab #2 Design.

Left: Fusion Design.

Right: 8bit Orthographic projection.

Bottom: FFDM image at 27kVp.

Slab #2 has a glandular structure volume of 62820 mm³ and is composed of 3 individual Ivy Structures (Figure 51 left). The FFDM image was acquired at 27kVp, with 140mA tube current and 71mAs exposure. The edge of the slab curvature appears very bright compared to Slab #1 and Slab #3 and exhibits no white fade towards the centre (Figure 51 bottom). PLA and coconut oil show a consistent but low contrast and make the distinction of fine features difficult. Bigger structures and patterns in the FFDM image can be distinguished and compared to the orthogonal projection (Figure 51 right), yet fine details, especially towards the edge can hardly be compared visually. The FFDM images shows two distinct black spots in the bottom half of the slab, indicating air pockets in the 4th quadrant (Figure 53 yellow). Further air pockets are visible in the 2nd quadrant of the top half of the slab (Figure 52 yellow). The drill hole in the 2nd quadrant is almost not visible because it is filled with coconut oil and wax (Figure 52 red). The drill hole in the 1st quadrant in Figure 52 is sealed but not filled with oil or wax (red). Certain dotted structures appear very bright. These are structures that contact both walls of the slab and are oriented orthogonally to the visual plane, hence causing heavy attenuation (Figure 52 1st quadrant pink).

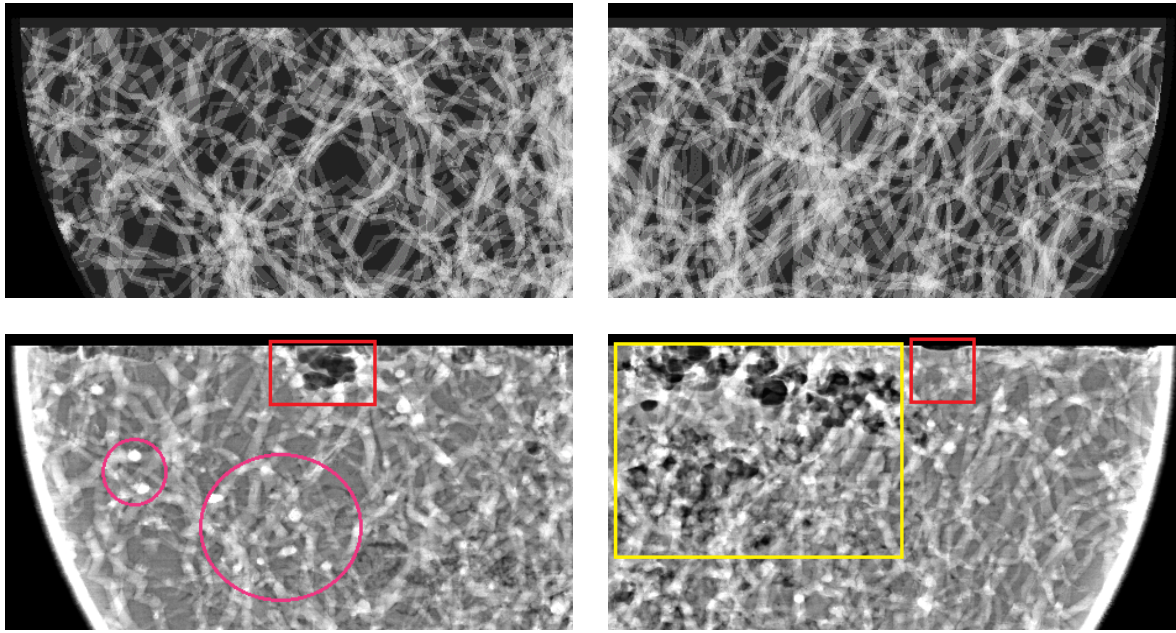


Figure 52: Slab#2: 1st (left) and 2nd (right) quadrant comparison.

Top: 8bit orthographic projection.

Bottom: FFDM image. The 1st quadrant (red) shows a drill hole with an air pocket and very bright dotted features (pink). The 2nd quadrant (yellow) holds a lot of air pockets towards the centre. The drill hole is indicated by a dent in the wax seal (2nd quadrant red).

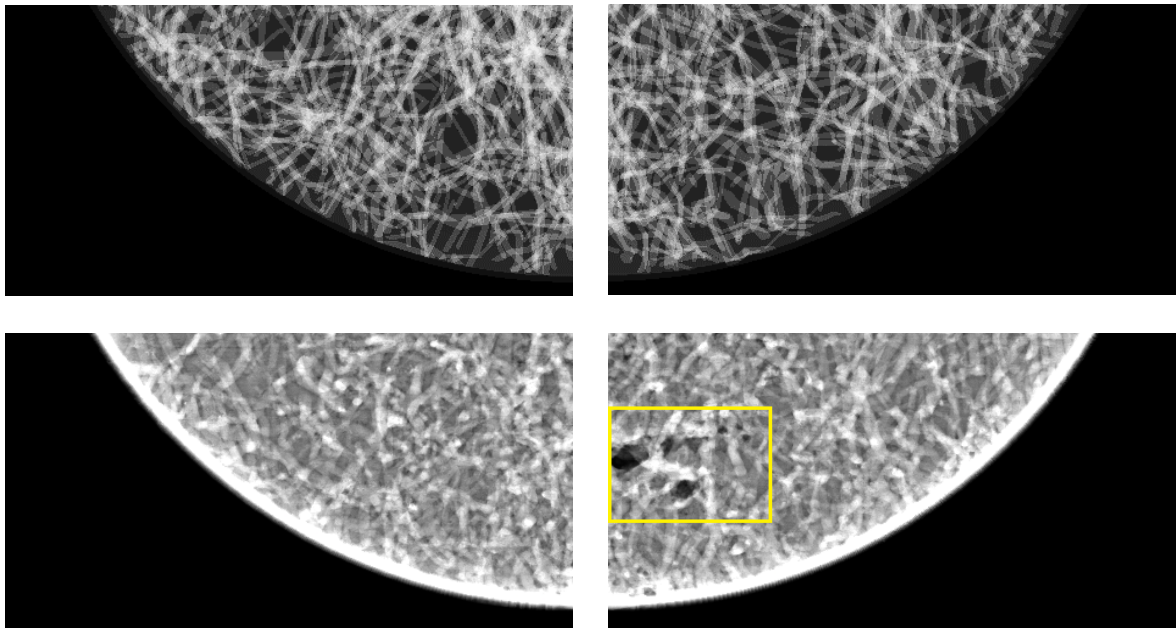


Figure 53: Slab#2: 3rd (left) and 4th (right) quadrant comparison.

Top: 8bit orthographic projection.

Bottom: FFDM image. The 4th quadrant exhibits two bigger and a few smaller air pockets. The fine features are very difficult to correlate by eye due to the low contrast.

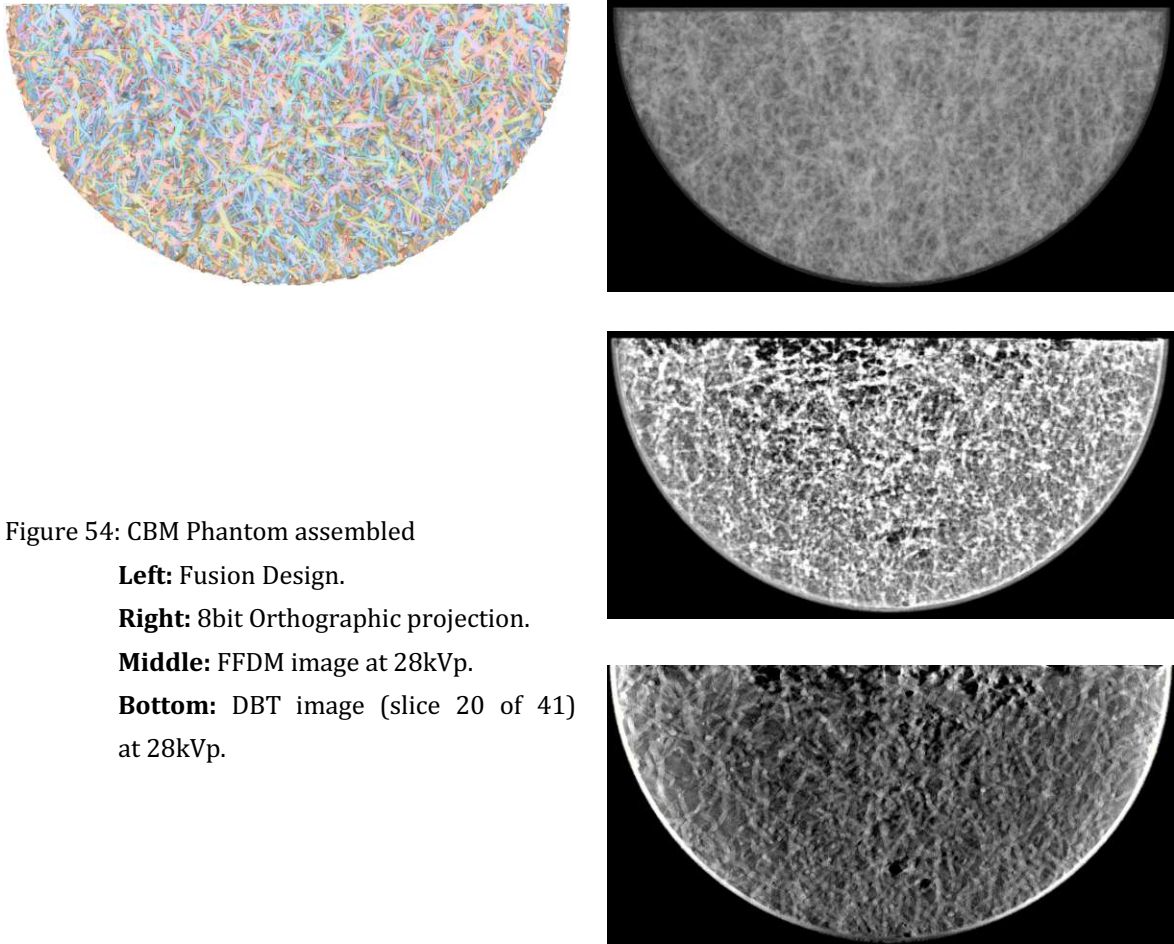


Figure 54: CBM Phantom assembled

Left: Fusion Design.

Right: 8bit Orthographic projection.

Middle: FFDM image at 28kVp.

Bottom: DBT image (slice 20 of 41)
at 28kVp.

The assembled CBM phantom has a total glandular structure volume of 181450mm^3 and consists of all 12 Ivy structures from the individual slabs (Slab#1, Slab#2, Slab#3) (Figure 54 left). The FFDM image was acquired at 28kVp, with 184mA tube current and 76mAs exposure (Figure 54 middle). For DBT, 26 images were acquired at 28kVp, with a tube current between 71-72mA and an exposure of 4-5mAs (example slice Nr. 20 at Figure 54 bottom). The 41 reconstructed DBT slices have a thickness of 1mm. The assembled CBM phantom FFDM image and DBT slice image both show a higher signal at the edge with a fade towards the centre. Several air pockets especially in the 1st and 2nd quadrant are visible (Figure 55, middle & bottom, yellow), as well as two distinct air pockets in the 4th quadrant (Figure 56, middle & bottom, yellow). The 1st and 2nd quadrant in the FFDM and DBT image both show empty drill holes that were not filled with oil (Figure 55, middle & bottom, red).

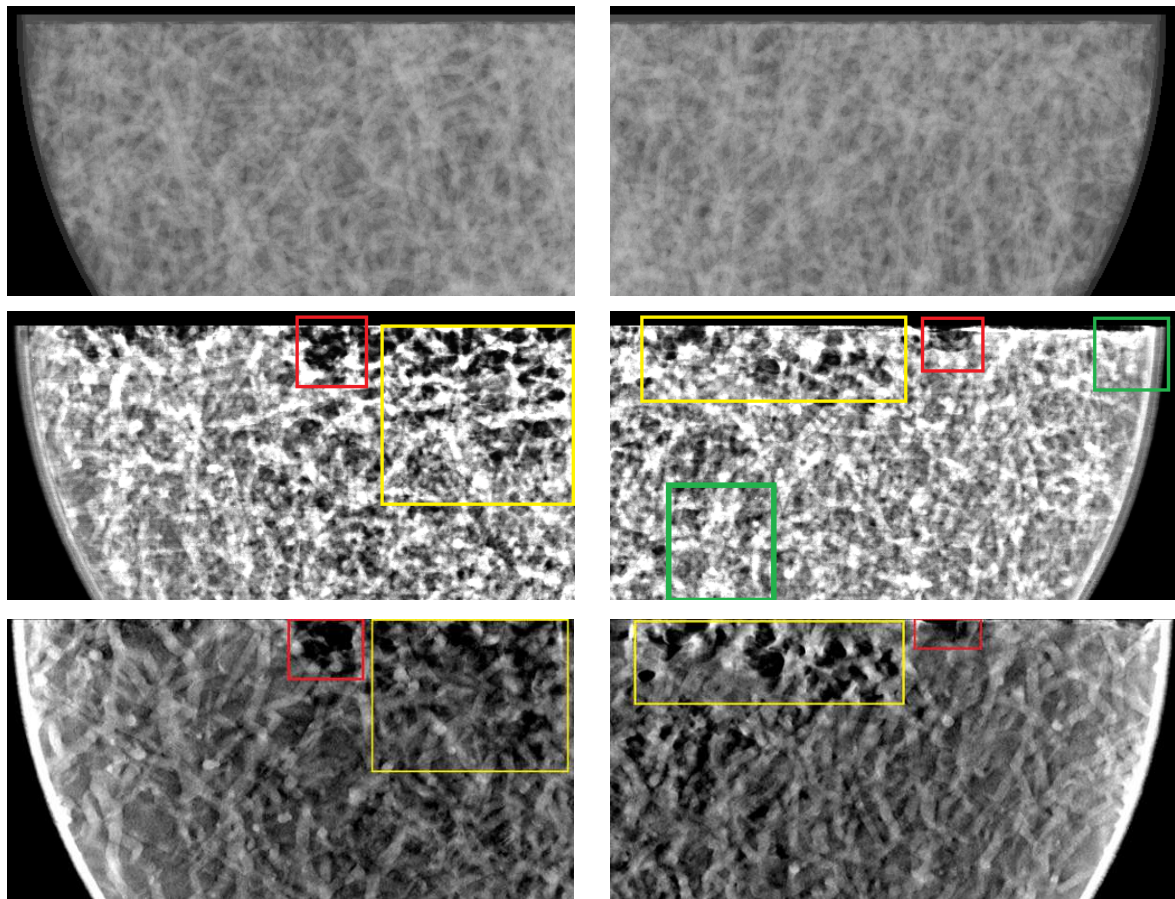


Figure 55: Assembled CBM phantom: 1st (left) and 2nd (right) quadrant comparison.

Top: 8bit orthographic projection.

Middle: FFDM image. The red rectangles in the 1st and 2nd quadrant imply drill holes that were not filled with oil. The two features (green) in the 2nd quadrant allow an identification of the FFDM image with the initial orthographic projection. Further a lot of air pockets are visible towards the centre (yellow).

Bottom: DBT slice 21/41 image. As in the FFDM image the 1st and 2nd quadrant both depict drill holes what were not filled with oil (red rectangle). Further the DBT slice unveils the air pockets clearly compared to the FFDM image (yellow).

Due to the high density of the overlaying inner structures, a distinction of fine and complex features is impossible by eye. Additionally the effect of perspective during image acquisition effectively shifts the pattern distribution of the glandular structure, giving the assembled phantom a different look in the FFDM/DBT image compared to the orthographic projection. Even bigger patterns and structures can hardly be matched with the orthographic projection, however the 2nd quadrant shows two features which allow to link the FFDM image to the orthographic projection (Figure 55, middle, 2nd quadrant, green).

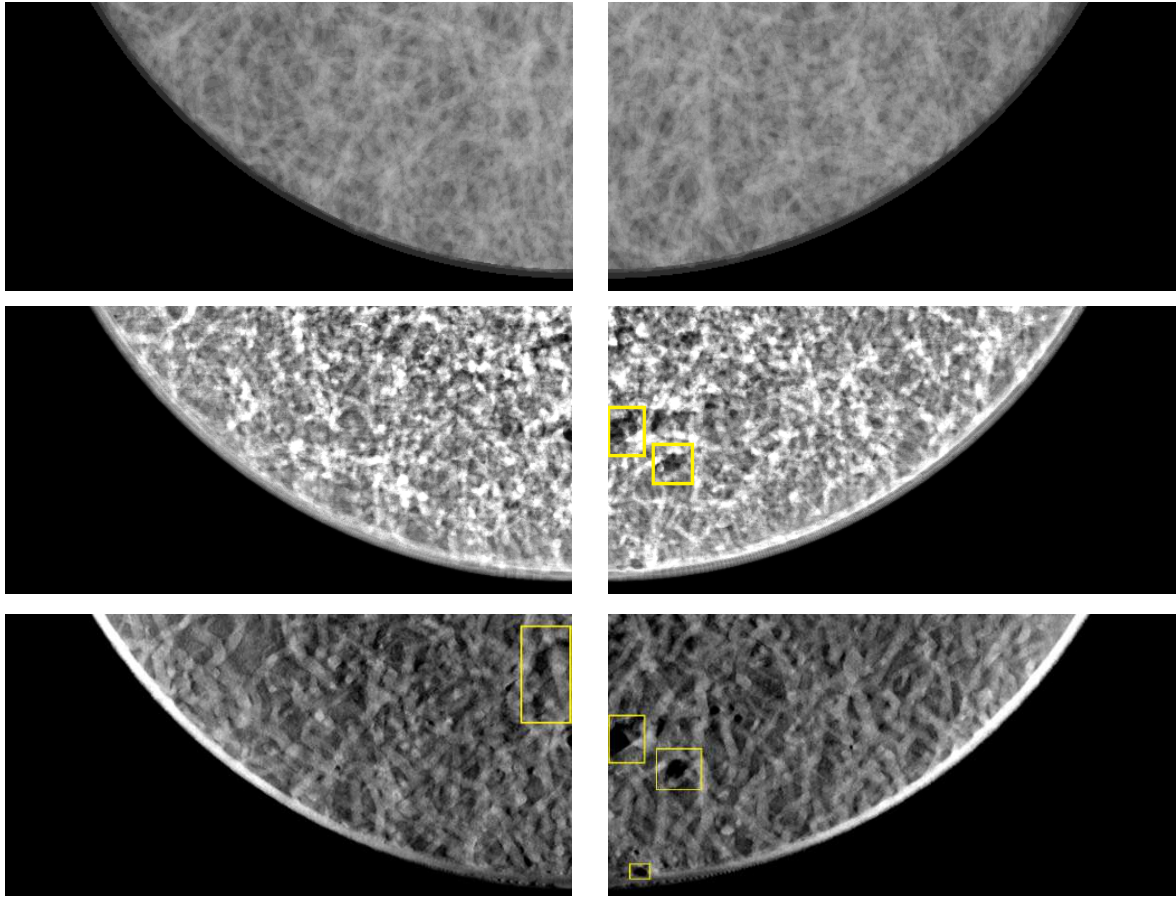


Figure 56: Assembled CBM phantom: 3rd (left) and 4th (right) quadrant comparison.

Top: 8bit orthographic projection.

Middle: FFDM image. Two distinct air pockets in the 4th quadrant (yellow)

Bottom: DBT Slice 21/41 image. The same two air pockets as in the FFDM image, and another small one at the bottom.

The 4th quadrant of the DBT slice in Figure 56 reveals a hidden air pocket at the bottom edge of the slab, that is hidden in the FFDM image due to super imposition (Figure 56, middle & bottom, 4th quadrant, yellow). The same effect can be observed in the 3rd quadrant of the DBT image, where another air pocket is revealed (Figure 56, bottom, 3rd quadrant, yellow).

3.2.2 Phantom 45 Images

Due to the height profile nature of Phantom 45 no DBT was acquired. Further only Slab A and Slab C were imaged individually, because Slab B represents a structure plate without any anthropomorphic details. Slab B was imaged as part of the assembled Phantom 45 (Figure 63 bottom).

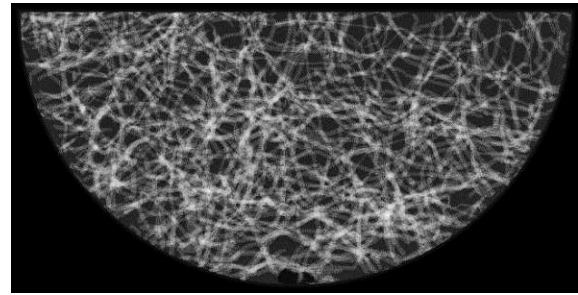
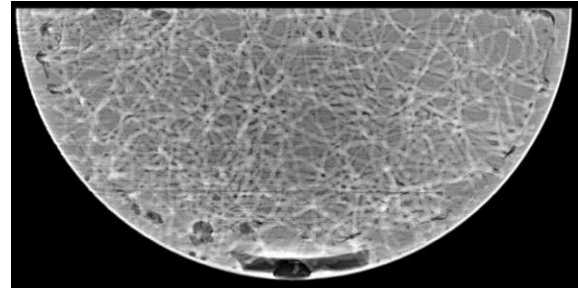


Figure 57: Phantom 45 Slab A Design

Left: Fusion rendering.

Right: 8bit Orthographic projection.

Bottom: FFDM image at 28kVp.



Design A represents a glandular structure volume of 50047mm^3 , based on a projection of 3 individual Ivy structures (Figure 57 left). The FFDM image was acquired at 28kVP, with 111mA tube current and 56mAs exposure (Figure 57 bottom). The contrast for the glandular structure (PETG) and the adipose tissue imitating paraffin wax is very good and allows for a visual pattern matching. The centre appears darker due to the warping related bending of the Topside of the casing (Figure 57 bottom). This is caused by an air gap between compression plate and the bent casing. The curvature of the rounded edge exhibits a high signal with a slight fade towards the centre. The area around the infill hole shows a lot of air due to an insufficient filling of wax. Further air pockets are visible along the curved edge (Figure 58, Figure 59 yellow). The slab exhibits horizontal lines across the entire surface due to fine air gaps between adjacent filament layers of the casing. These lines are most visible in areas with little inside structure, especially in areas towards the edge as shown in the 1st quadrant (Figure 58 pink arrow). The problem of the horizontal lines in combination with the air pockets makes the pattern matching difficult around the slab edges. Especially fine details are hard to distinguish. The majority of structures in the FFDM image can also be found in the orthographic projection.

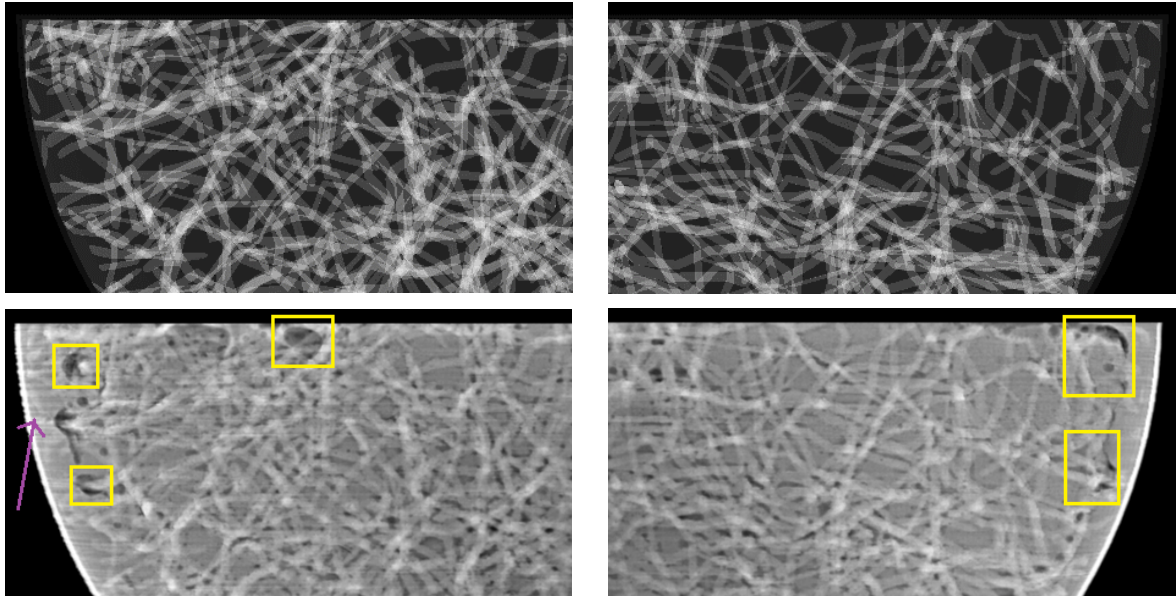


Figure 58: Slab A: 1st (left) and 2nd (right) quadrant comparison.

Top: 8bit orthographic projection.

Bottom: FFDM image. Yellow indicates small air pockets along the curved edge. The centre appears darker due to the air gap of the bent casing. In the 1st quadrant (pink) horizontal lines are visible towards the edge

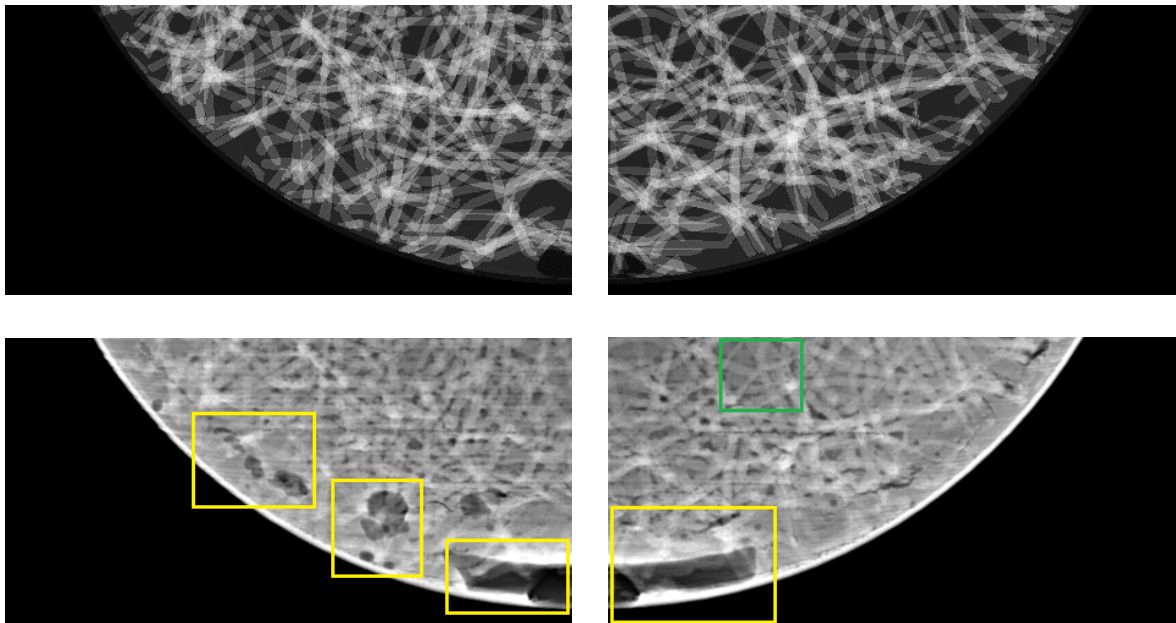


Figure 59: Slab A: 3rd (left) and 4th (right) quadrant comparison.

Top: 8bit orthographic projection.

Bottom: FFDM image. Yellow indicates air pockets and missing wax towards the infill hole. In the 4th quadrant examples of fine structures are visible (Green). The 3rd and 4th quadrant both show a horizontal line pattern across the whole surface.

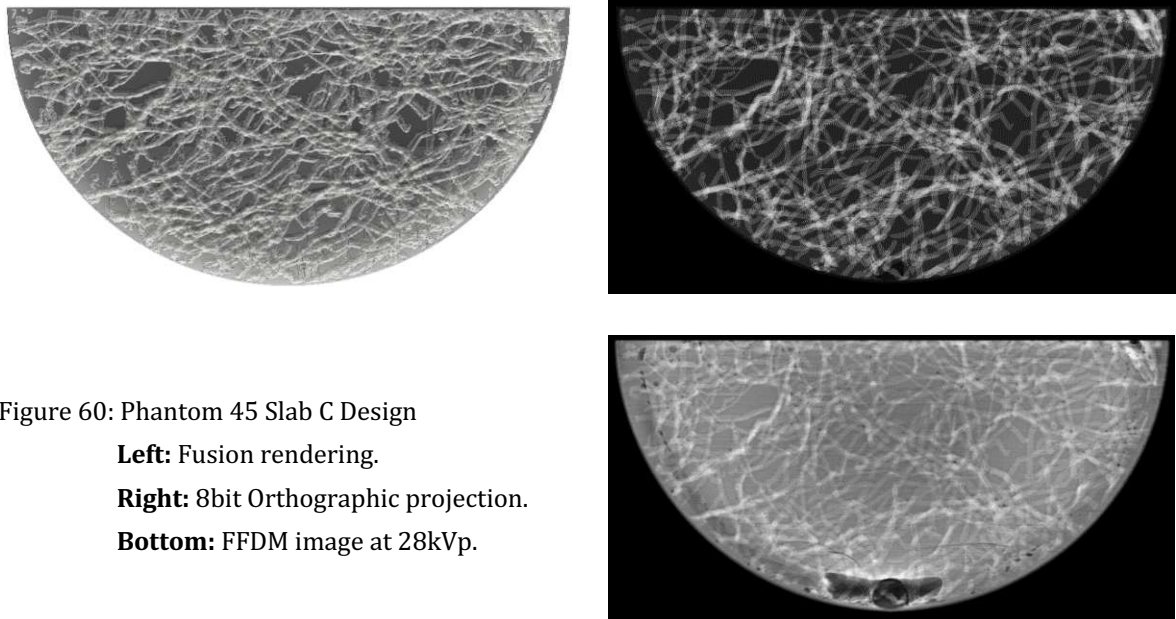


Figure 60: Phantom 45 Slab C Design

Left: Fusion rendering.

Right: 8bit Orthographic projection.

Bottom: FFDM image at 28kVp.

Design C represents a glandular structure volume of 48951mm^3 , based on a projection of 2 individual Ivy structures (Figure 60 left). The FFDM image was acquired at 28kVp, with 111mA tube current and 56mAs exposure (Figure 60 bottom). The contrast between PETG and paraffin wax is very good and allows a clear distinction of structural features and pattern matching. The centre exhibits the same dark area as in Slab A due to the air gap between the bent casing and the compression plate. Although less distinct, fine horizontal lines are spread across the whole FFDM image. Like in Slab A these are related to the adjacent filament layers which cause a fine ripple structure on the casing surface. The FFDM image of Slab C exhibits less scattered air pockets compared to Slab A. Two distinct air pockets can be seen in the 1st and 2nd quadrant towards the curved edge (Figure 61, yellow arrows), and especially in the 1st and 3rd quadrant along the curved edge as a dark rim (Figure 62 yellow arrows). The dark area around the infill hole indicates insufficient wax filling, but is less pronounced than in Slab A. Compared to Slab A and the CBM phantom slabs, Slab C has no high signal around the outer edge, and the curved edge-related fade is almost not visible compared to Slab A. In the 3rd and 4th quadrant, fine dark fissures are visible. These could imply air-filled cracks in the casing (Figure 62 pink). The 1st quadrant in Figure 61 (green) shows very fine features and complex structures in the FFDM image, that are clearly identifiable in the orthographic projection.

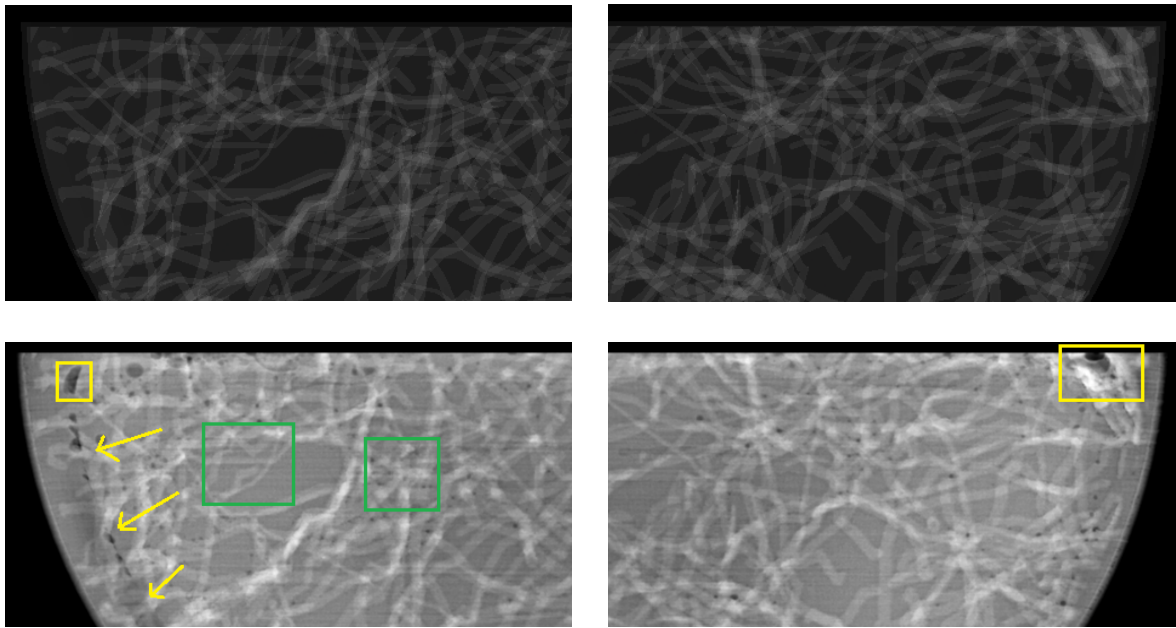


Figure 61: Slab C: 1st (left) and 2nd (right) quadrant comparison.

Top: 8bit orthographic projection.

Bottom: FFDM image. The yellow arrows in the 1st quadrant indicate a continuous air layer at the curved edge. The yellow rectangles show distinct air pockets at the top. Green shows very fine and complex features that were realized.

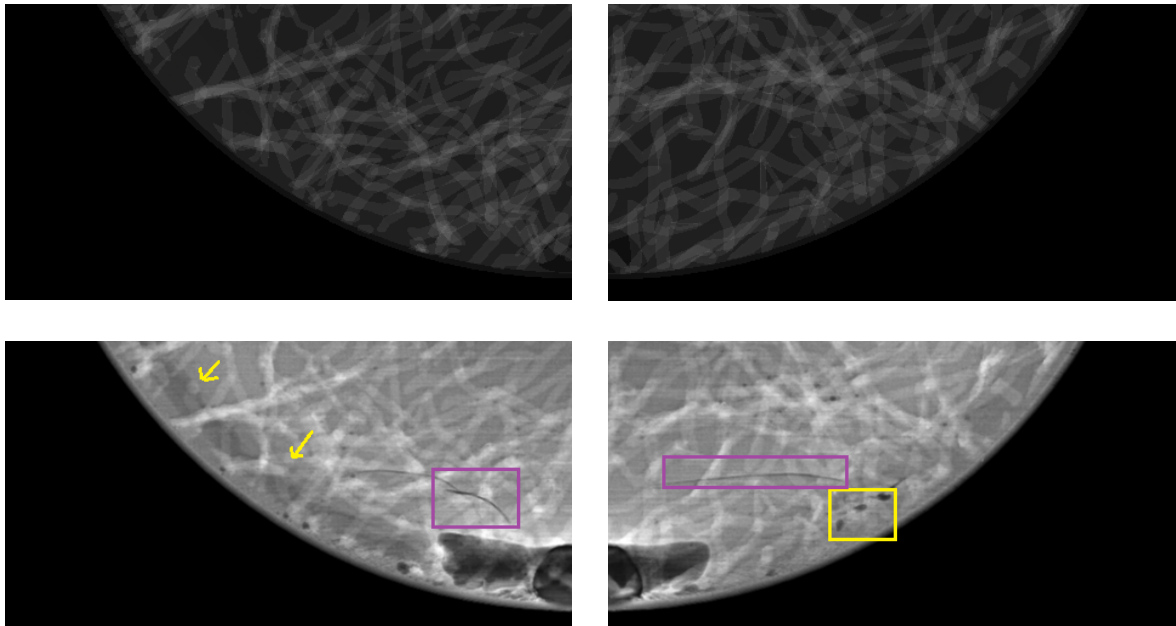


Figure 62: Slab C: 3rd (left) and 4th (right) quadrant comparison.

Top: 8bit orthographic projection.

Bottom: FFDM image. Yellow arrows in the 3rd and the yellow rectangle in the 4th quadrant refers to the continuous air layer and individual small air pockets. Pink rectangles show dark fissures which could be air filled cracks in the casing.

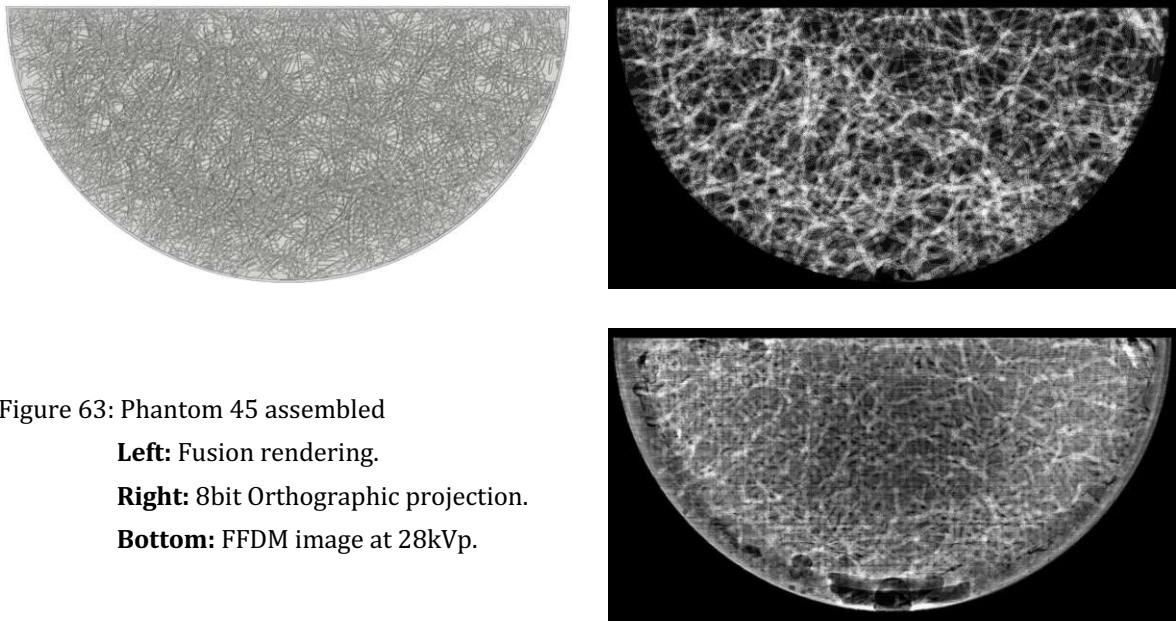


Figure 63: Phantom 45 assembled
Left: Fusion rendering.
Right: 8bit Orthographic projection.
Bottom: FFDM image at 28kVp.

The assembled Phantom 45 represents a glandular structure volume of 98998mm^3 , the sum of the individual glandular structures of Design A and Design C (Figure 63 left). The FFDM image was acquired at 28kVp, with 178mA tube current and 57mAs exposure (Figure 63 bottom). A shadow in the middle of the assembled Phantom 45 is clearly visible (Figure 63 bottom). It is caused by the two air gaps of the bent casings of Slab A and Slab C, in contact with the support plate and compression plate respectively (Figure 64, Figure 65 pink arrows). Further a grid pattern is spread across the whole FFDM image as a result of the uneven surface of Slab B (= 5mm structure plate). The central shadow and the overlaying grid pattern make a visual comparison of fine details difficult, especially towards the edges. However bigger structures and patterns are still recognizable in the FFDM image with respect to the orthographic projection (Figure 65, 4th quadrant, green). In the assembled state of Phantom 45, the overlay of fine air layers and small air pockets along the curved edges of Slab A and Slab C do not allow for a proper visual pattern comparison in that area (Figure 64, 1st quadrant, Figure 65, 3rd quadrant, yellow arrows and rectangles). Despite the shadow in the centre, a few fine and complex structure elements can roughly be distinguished and found in the orthographic projection (Figure 64, 2nd quadrant, green).

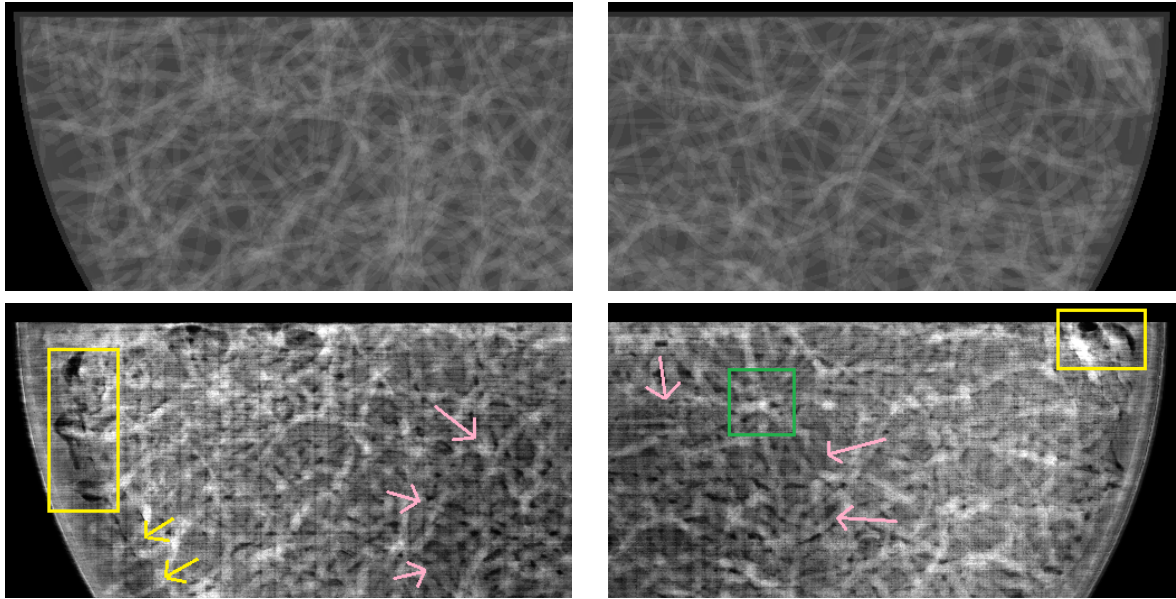


Figure 64: Phantom 45 stacked: 1st (left) and 2nd (right) quadrant comparison.

Top: 8bit orthographic projection.

Bottom: FFDM image. The 1st and 2nd quadrant show the outline of the central shadow caused by the air gap (pink arrows). Further individual bigger air pockets can be made out at the edges (yellow rectangles). In the 2nd quadrant (green) an example of a complex feature is given, that is very fine but can still be made out despite the visually impairing grid pattern and air gap shadows.

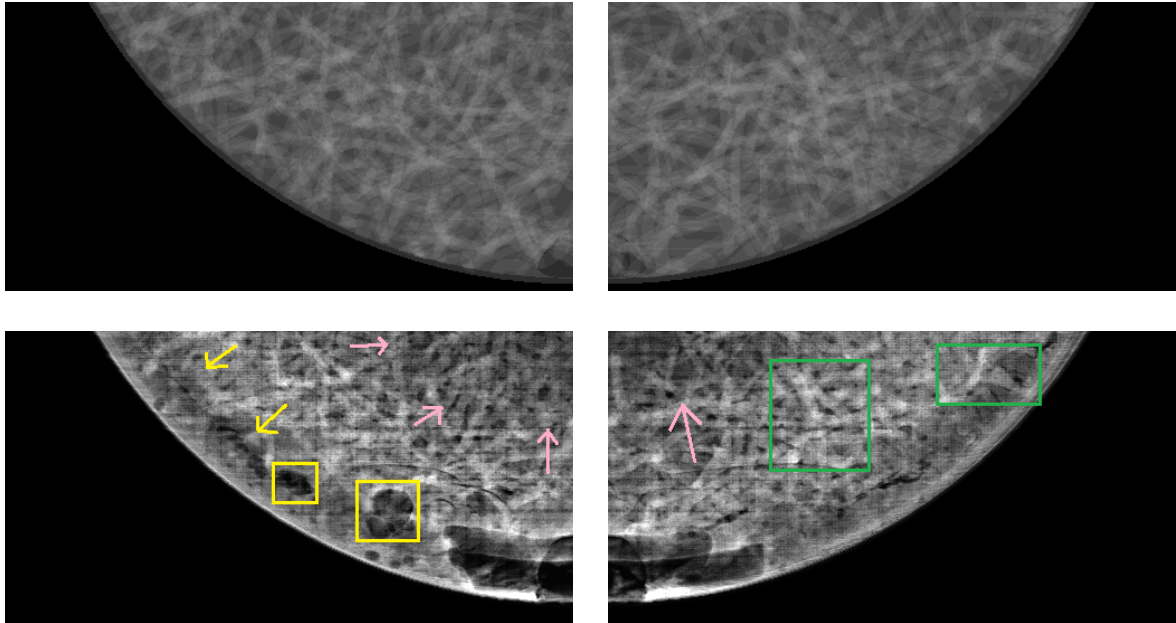


Figure 65: Phantom 45 stacked: 3rd (left) and 4th (right) quadrant comparison.

Top: 8bit orthographic projection.

Bottom: FFDM image. The 3rd quadrant shows the fine air layer (yellow arrows) around the edge and distinct air pockets (yellow rectangles). Further the outline of the central shadow is visible (pink arrows). The 4th quadrant shows two examples of structure features that can roughly be distinguished (green).

4 Discussion

Overall the realization of two assembled phantoms with fine glandular tissue-like structures succeeded. The contrast in the FFDM/DBT images between the glandular tissue-simulating and adipose tissue-imitating materials was good enough to distinguish individual patterns and fine details. This allowed to visually cross correlate and pattern-match the FFDM/DBT images with the orthographic projections of the initial CAD designs. In both assembled phantoms, and their individual slabs, the distinction of coarser and finer features in the FFDM/DBT images was possible and identifiable in the orthographic projection, and the majority of the respective inner structures could be realized by the printers. The print quality between the slab casings of the CBM phantom and Phantom 45 differs greatly. While the CBM phantom slabs (PLA) were completely plane considering both large surfaces (Topside, Bottomside), and fit very well together in the assembled state, the Phantom 45 (PETG) slabs exhibited warping related dents on the Topsides of Slab A and Slab C, and did not stack well in a assembled formation. The resulting air layers due to these dents were slightly visible on the single slab FFDM images, and extensively visible in the assembled Phantom 45 FFDM image. The heterogeneous surface ripples of the Slab A, Slab B and Slab C caused unwanted horizontal lines in case of Slab A and Slab C, and in the assembled state an additional black grid overlay due to Slab B. The filling process caused more individual air pockets in the CBM phantom, but bigger air layers and unevenly distributed adipose-tissue imitating material around the infill holes in Phantom 45. While the realization of a pseudo-glandular network via 3D-printing was a success in both approaches, several improvements considering printing material, the printing process and the filling of the slabs can increase the quality of the presented phantom designs significantly. This closing chapter will elaborate on issues during the manufacturing process and give development ideas for more refined models based on the same design concepts.

Printing, Material and Design Optimization: The printing process of the CBM phantom slabs with PLA on the V400 worked well, however the print bed adhesion would reduce significantly after several hours of printing. Despite precise layer deposition, the first attempt to print the middle slab of the CBM phantom (Slab #2) resulted in the half-completed print to be knocked off the print bed by the print head. The first layers of PLA in contact with the print bed as well as the brim had cooled and detached completely. In the subsequent printing attempts the brim lines and the first few centimeters of the print were fixed to the print bed with duct tape (Figure 66). This held the print steadily, and allowed for proper completion. PETG and *colorfabb_HT clear* [84], (PET based high temperature material for experimental prints) on the other hand showed a very consistent bed adhesion on the V400 spring steel print bed, but had the issue of strong warping effects during and after the printing process.

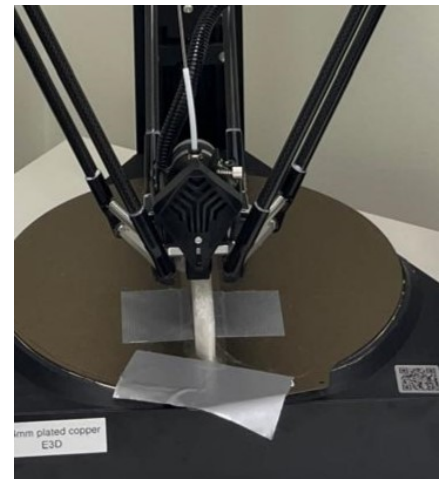


Figure 66: Adhesion improvement
with duct tape on V400

Warping: Two experimental attempts to print the CBM slabs with the *colorfabb_HT* filament resulted in massive warping, leading to the deformation and partial rupture of the completed slabs, due to the strong contraction forces (Figure 67). A lower, but still noticeable warping effect lead to the bent Topside of the finished Phantom 45 casings in Slab A and Slab C (Figure 43, Top Right). These slabs however were printed with a PETG filament (HDGlass FormFutura) on the Ultimaker S3. It is debatable whether the reduced warping effect can be assigned to the filament material or the semi-closed printing chamber in the Ultimaker S3, compared to the open print bed of the V400. 3D-printing community reviews of filaments with strong warping tendency conclude, that closed and heated printing chambers are ideal to deal with warping related print deformation, since the cooling down of the print is delayed and allows for the filament to solidify properly. This counteracts the contraction forces and prevents deformation. Another approach to tackle the warping issue lies in the design concept of the slabs. A wall thickness of 1,2mm, as was used in Phantom 45 and partly in the CBM phantom (Slab #1 and Slab #3), appears to be too thin and causes the casing to be unstable to withstand

even low warping forces. Future slab designs should have a wall thickness of at least 1,6mm, probably even 2mm to have a sturdy casing, which can withstand warping forces and thermal deformation better.

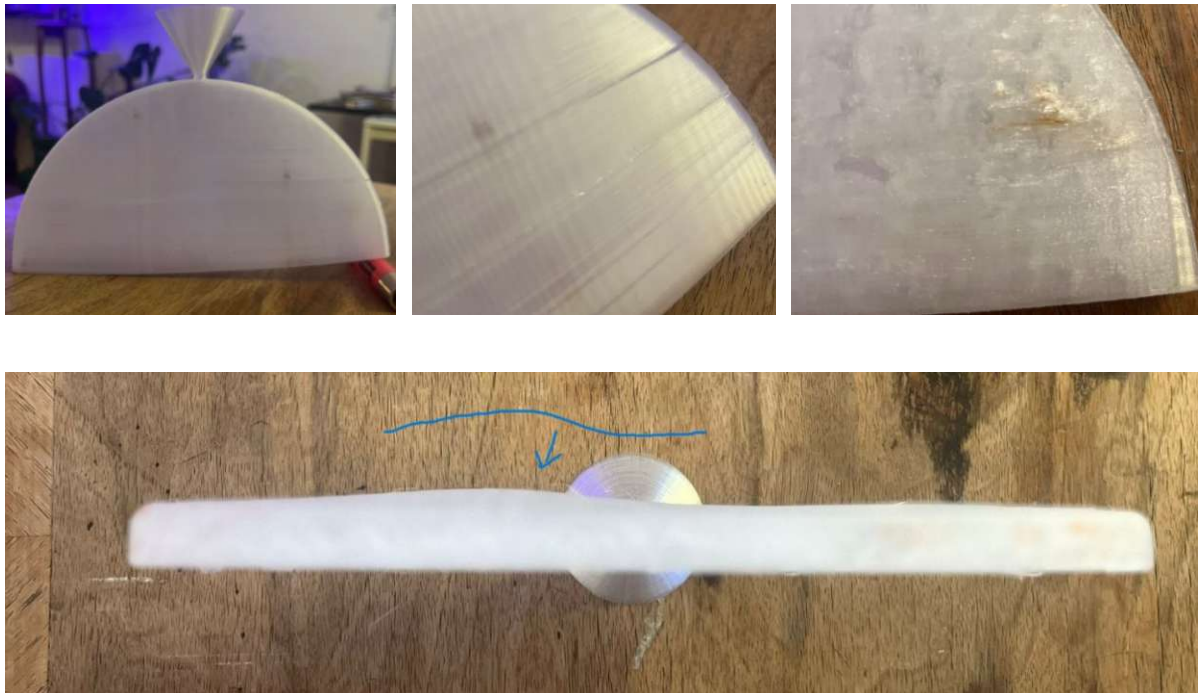


Figure 67: ColorFabb_HT experimental prints with an attached filling funnel for wax/oil.

Left: Massive warping on the chestwall side.

Middle: Ripping of Topside due to torsional warping forces.

Right: Overprinted caramel corn.

Bottom: Wave-like bending of Topside due to warping forces (blue arrow).

Phantom 45 Dual Extrusion Print: The Phantom 45 alternative design could ultimately not be realized due to strong warping effects of ABS, which was used as the adipose-tissue imitating material. The design concept would follow the same approach as the CBM phantom, meaning that a casing with a real 3D inner structure (Ivy structure printed with Tough PLA) would represent the glandular tissue, but instead of filling the intermediate space with oil or wax to mimic the adipose tissue, ABS would be printed to fill up the remaining void space. This was supposed to be realized with the Dual Extrusion feature of the Ultimaker S3. Unfortunately the strong ABS warping caused the print to bend upwards and detach from the glass print bed after the first couple of layers. It seems that the warping issue is indeed also a question of filament quality, since Varallo et al. [48] realized a similar design concept, upon which the dual extrusion

print approach of Phantom 45 is based, but did not mention any issues considering the printability of ABS. Varallo et al. also used the Ultimaker S3 printer in dual extrusion mode, yet with ABS filament by Ultimaker, while the approach in this thesis used ABS by FormFutura. A repetition of the dual extrusion print of Phantom 45 with the same filaments Varallo et al. used would be an intriguing experiment for the future.

Filament Drying: Some filament types, like PET, PETG (HDglass) and PET-related filaments (colorfabb_HT) showed the tendency to absorb moisture and cause bubbles during filament melting and extrusion. Crackling sounds and milky appearance of otherwise transparent filaments were good indicators for moisture in the material. A filament that has absorbed too much moisture can cause uneven and failed filament deposition. This, in turn causes uneven print surfaces and air inclusions, with the latter being especially problematic in imaging related purposes. Slab A of Phantom 45 was printed first on the Ultimaker S3 and showed a significantly worse surface structure in terms of homogeneity compared to Slab C, which was printed after. The difference was also visible in the FFDM images (Figure 57 bottom, Figure 60 bottom). Since the print settings and overall geometry of both slabs were identical, the difference in print quality can be attributed to the outer filament windings of the mounted filament spool, which were more exposed to moisture and therefore absorbed it more than the inner filament windings. Further due to moisture so-called *caramel corns* can form, which are residual filament accumulations, that can settle on and around the nozzle after failed deposition (Figure 67 Top Right). Due to the high nozzle temperature of usually +200°C these filament accumulations get burned and turn brown. After reaching a certain size they would drop into the print area and get stuck randomly on the print. When such caramel corn formations were observed, they were quickly removed by hand, but if left unattended they got printed over by the next layers, causing unwanted bumps in the final print. Therefore a thorough drying process of hygroscopic filaments is mandatory and was applied to all PET(G) related filaments after several printing issues. Drying the filament for three to six hours in a 60°C hot air oven with added desiccants like silica-gel packs can help to improve the filament quality greatly. Phantom 45 Slab A and Slab C could ultimately be printed without any caramel corns.

Print Refinement: Further adjustments of the printing process and applying additional postprocessing steps of the prints can improve the image quality significantly, especially considering the uniformity of surface texture. As could be seen with the FFDM images of the Phantom 45, the individual printed filament layers resulted in line structures covering the whole image (e.g.: Figure 58, bottom, 3rd quadrant, purple). These line structures appear on the FFDM image due to fine air gaps between adjacent layers of filament on the surface (ripples). For a more homogeneous surface texture, sanding paper could be used to remove height differences and potential air gaps. Subsequent decrease of the sanding paper grit during polishing would greatly increase the homogeneity and help to reduce the effect of line structures. Naturally this would only work on reachable surfaces, referring to the outside of the 3D-printed slabs. The grid structure (Figure 63 bottom, Figure 64 bottom) caused by the structure plate (Slab B) in the FFDM image of assembled Phantom 45, could be reduced greatly with the sanding method. However, it is important to consider the resulting heat and thermal effects on the respective filament material. The 3D-printing community advises a wet sanding approach to prevent potential deformation in heat sensitive materials. A different method to avoid the formation of air gaps during the print, is implemented into Cura Slicer with the selectable option: *Ironing*. After every completed layer, an additional very thin layer of filament will be placed on top, effectively remelting the last layer and hence cause a better closing of the creases. While increasing the printing times significantly, this is an interesting method for surfaces that cannot be reached for postprocessing, or for potential air gaps that are caused inside solid prints with 100% infill density. This issue of air gaps inside solid prints was apparent in the FFDM image of the dual extrusion test cube, printed with Tough PLA and ABS (Figure 35). Regular dotted lines and grid structures suggest fine air gaps between the adjacent layers, that are caused by the shrinkage of the printing material. Other possibilities to handle this issue is to increase the extrusion rate over 100% (105%,110%). Ma et al. [15] conducted several experiments in that regard to find the optimal extrusion rate for different FDM materials to get a fully solid print of 100% material, without any air gaps.

Filling Casings with Waxes and Oils. Fine air layers and air pockets could be observed in all wax and oil filled slabs in the CBM phantom and Phantom 45. This is an issue that complicates image analysis the most, be it merely visual or with imaging software. The formation of such air pockets can be reduced by pouring liquid oil or wax very slowly into the respective slab in a stepwise fashion, and by letting the wax/oil cool down very slowly in a prewarmed water bath or oven. Furthermore a gentle vibrating surface could slightly shake the slab during the solidification to help detach trapped air bubbles. A very effective method might be to keep the slab in a warm water bath which is equipped with an ultrasound generator during filling (but not during solidification). Here the softening temperature of the printing material must be considered, since it can be close to the melting point of wax (e.g.: PLA filament usually $\sim 58^{\circ}\text{C}$ HDT). However the shrinking process during cooling down can still cause fine gaps between wax/oil and the slab casing. These can be removed by several cycles of remelting and solidification since the wax/oil will eventually creep into the remaining gaps. Here the temperature should not be set too high or the wax/oil will reach a fully liquid state again. The experimental SLA prints of Phantom 45 Slab A were heated for too long which caused the wax to become completely liquid again and partly deforming the Slab casing in case of the ABS-like 3.0 resin printed slab. When cooling down and turning solid, several air pockets had formed which could not be removed anymore without having to reheat and drain the entire slab of all the wax, and then refill it again. In regard to design improvements for an easier filling process, the CBM phantom casing design could be closed in future versions and have three filling holes as part of the design spread across the chestwall side (Figure 68 Left).

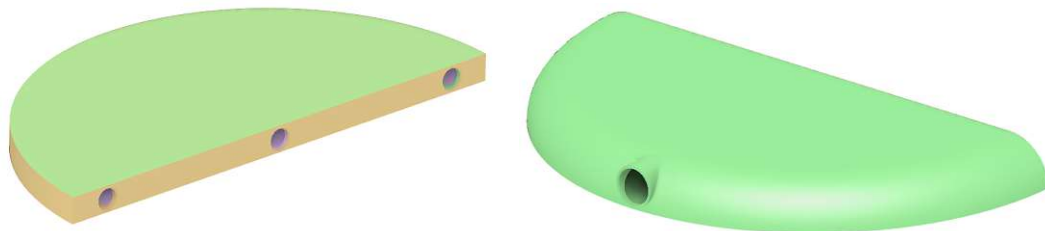


Figure 68: Future design concept for the filling holes for the CBM phantom (left) and Phantom 45 (right).

Alternating between all three holes during the filling process will improve the first distribution of the melted wax/oil and allows for an easier filling of the corners, which are prone to air gaps.

The drill holes then need to be closed properly, which was also an issue with the CBM phantom, which showed several unevenly filled drill holes in the FFDM and DBT images (Figure 49, Figure 52, Figure 55). Phantom 45 could be improved by adding an elevated filling neck (Figure 68 Right). This would allow for a complete filling of the slab and prevent big wax voids around the filling hole (Figure 59, Figure 62)

Future Phantom Design Concepts: The idea of Schopphoven et al. [52], about printing a solid breast model with a height profile positioned on top, influenced the approach that was taken with Phantom 45. The creation of the simulated glandular tissue pattern however differs in this thesis. An interesting concept, combining both approaches, would be to use raw clinical DICOM images, and load them as Texture files (.PNG) into Blender. With the presented height profile conversion procedure one could thereby create a real patient height profile-mesh and combine it with a casing. Then one could resize the resulting mesh according to the glandular/adipose tissue ratio, and ultimately fill the remaining volume with wax, oil, or some other adipose tissue equivalent material. Several height profile slabs based on raw clinical images could be combined to create new patterns. The arbitrary pattern-combination process would follow the same approach as with the combined 3D Ivy-Structure designs in the CBM phantom, but with a simpler printing procedure. The advantage of this method lies in the possibility to scale the height of the spikes according to the required glandular structure volume. This, in turn can come at the cost of resolution. In that regard measurements of the same pattern with varying maximum z-height of the height profile would be necessary to evaluate the lower boundaries below which the resolution loss becomes too big during the print process.

The concept by Varallo et al.[48], which suggests creating a slab-envelope representing the skin, could be combined with a double sided height profile slab that combines two patterns into one according to the required glandularity (Figure 69 Top). This could reduce the number of walls and allow for the remaining walls to be thicker and hence sturdier. In this concept a single hollow slab casing, representing a compressed breast, is designed with an open chestwall side. The inside of the casing would have a guide rail on the sides, which allows to plug in the height

profile structure, and fill the intermediate space with some adipose-tissue imitating material (wax, oil) (Figure 69, Bottom).

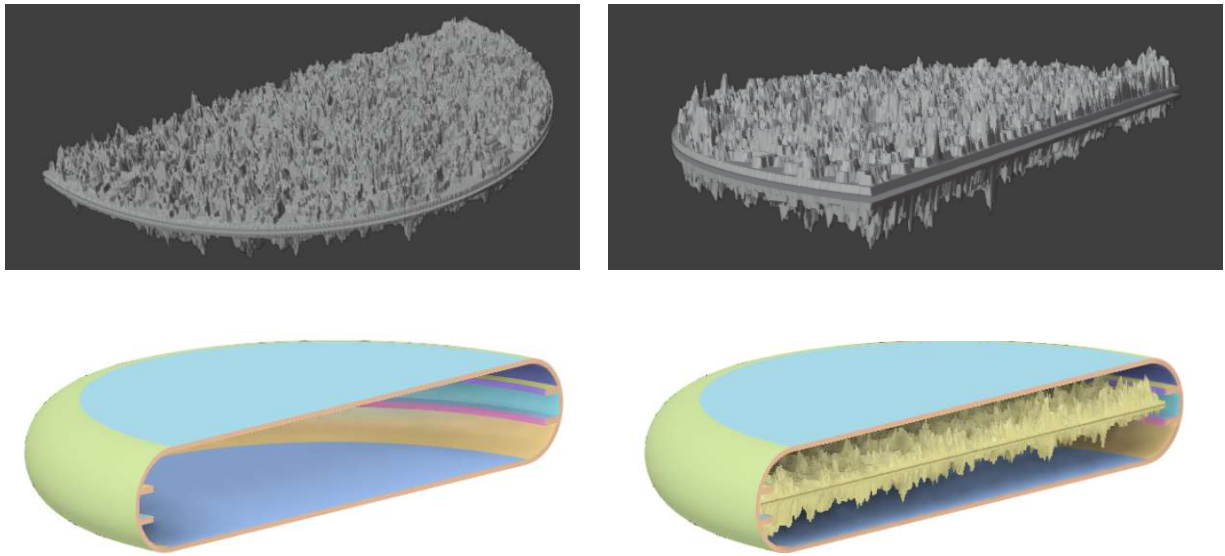


Figure 69: Concept of a double sided height profile (Top), and a casing envelop with guide rails (Bottom).

Limitations: While the realization of both design concepts was successful, it has to be kept in mind that they present merely a primitive two compartment model, simulating only glandular and adipose tissue. A more realistic approach would require several additional compartments, including skin, fibrous tissue, vascular and lymphatic tissue and the nerve tissue, all with their respective linear attenuation coefficients, hence different printing materials. This of course raises the question of printability, since especially the vascular and lymphatic tissue can have capillaries and vessels starting at 5-10 μm in diameter which is far below the average resolution limit of 20-50 μm of the used 3D printers in this thesis, FDM and SLA alike. Further this would require a 3D printer which can switch between several materials during the print. This could be an exciting and challenging task for refining and further developing the basic concept presented here.

Conclusion and Outlook

The scope of this thesis was to create a prototype of an assembled 3D-printed mammography phantom for further development and potential future calibration tasks and Quality Analysis of mammography machines. The phantom dimensions were purposely oversized to gain more experimental data. The geometric outline was influenced by the physical L2-model by Salomon et al. [55] and the initial concept by Cockmartin et al. [54] and Baneva et al. [59]. The symmetric assemblable-construction is similar to commercially available models like CIRS Modell 020 [44]. The basic phantom design was carried out in CAD Fusion by AutoDesk and Blender 4.2 with the Ivy-Generator Add-on. The CAM method of choice was Fused Deposition Modelling (FDM) with the printers Fusion V400 and UltimakerS3 and stereo lithography (SLA) with the Saturn 4 Ultra by Elegoo. The used filament materials PLA, PETG and ABS were chosen due to their similar linear attenuation properties in regard to glandular and adipose tissue in common mammography spectra as was shown in the work of Mettivier et al. [57] and Ivanov et al. [56]. Ultimately two design concepts have been successfully realized: the Three-Component Basic Model (CBM, 240x120x40mm, made of PLA) and Phantom 45 (240x120x45mm, made of PETG). The CBM phantom is comprised of three equally thick and rounded-off anthropomorphic plates, that roughly resemble a compressed breast during a Mammography screening. The inside of every plate is a random network of duct-like structures that are supposed to simulate the ducts of the glandular tissue network. The intermediate space was filled with an adipose tissue-imitating material (Coconut-oil). Phantom 45 consists of two thick anthropomorphic plates, and a thin structure plate with drilled holes for potential iodinated platelet inserts. On the inside of the anthropomorphic plates are height profile structures, which resemble an orthographic projection of a simulated glandular-tissue network. The intermediate space was filled with pure paraffin-wax. Both phantom designs were imaged at the Medical University Vienna – Central Hospital – Radiology and Nuclear medicine department on a Siemens Healthcare MAMMOMAT Revelation. FFDM images of the assembled phantoms and their individual anthropomorphic plates (slabs) were obtained at 27 and 28kVp respectively. Additionally a DBT of the CBM phantom with 26 views was conducted at 28kVp, with 41

reconstructed slices. The resulting FFDM/DBT images were visually compared with orthographic projections of the initial CAD design renderings for pattern-visibility and contrast between printing materials. The individual plates showed a good agreement in visual pattern-matching. Fine details, and complex branching structures could be clearly identified in the FFDM/DBT images and the respective orthographic projection of the design renderings. The skin -imitating surface of the anthropomorphic plates (slab casings) of Phantom 45 were bent towards the centre due to a warping issue that occurred during the printing process with PETG. These dents were visible as dark air pockets on the Mammography images. A visual analysis for the assembled CBM phantom was almost not possible due to its high level of internal structural complexity. This will require further analysis with various window-settings and other Imaging evaluation methods.

The results of this thesis show the technical feasibility of realizing 3D-printed breast models, that roughly mimic the parenchymal breast tissue in FFDM and DBT, with focus on the glandular duct system. While being primitive two-compartment prototypes, resembling only glandular and adipose tissue, further research on adding more compartments and structure complexity could improve the amount of realism in both phantom designs significantly. Experiments towards tissue-equivalent printing and filling materials, together with print refinement in postprocessing and proper volumetric projection renderings would drastically augment the resulting image quality and allow for a more realistic image appearance.

5 References

1. Autodesk. *Autodesk Fusion*. 02.02.2025]; Available from: <https://www.autodesk.com/products/fusion-360/overview?term=1-YEAR&tab=subscription>.
2. Foundation, B. *Blender 4.2*. 02.02.2025]; Available from: <https://www.blender.org/>.
3. Siemens Healthineers AG. [cited 2025 30.01.2025]; Available from: <https://www.siemens-healthineers.com/corporate-info>.
4. *The Osteoid*. 02.02.2025]; Available from: <https://competition.adesignaward.com/design.php?ID=34151>.
5. Evill, J. *Cortex*. 02.02.2025]; Available from: <https://www.evilldesign.com/cortex>.
6. Bandow, K., et al., *Low-intensity pulsed ultrasound (LIPUS) induces RANKL, MCP-1, and MIP-1beta expression in osteoblasts through the angiotensin II type 1 receptor*. *J Cell Physiol*, 2007. **211**(2): p. 392-8 DOI: 10.1002/jcp.20944.
7. Murphy, S.V. and A. Atala, *3D bioprinting of tissues and organs*. *Nat Biotechnol*, 2014. **32**(8): p. 773-85 DOI: 10.1038/nbt.2958.
8. Zopf, D.A., et al., *Bioresorbable airway splint created with a three-dimensional printer*. *N Engl J Med*, 2013. **368**(21): p. 2043-5 DOI: 10.1056/NEJMc1206319.
9. Mayer, H.F., A. Coloccini, and J.F. Vinas, *Three-Dimensional Printing in Breast Reconstruction: Current and Promising Applications*. *J Clin Med*, 2024. **13**(11) DOI: 10.3390/jcm13113278.
10. Giannopoulos, A.A., et al., *Applications of 3D printing in cardiovascular diseases*. *Nat Rev Cardiol*, 2016. **13**(12): p. 701-718 DOI: 10.1038/nrcardio.2016.170.
11. Sun, Z. and C. Wee, *3D Printed Models in Cardiovascular Disease: An Exciting Future to Deliver Personalized Medicine*. *Micromachines (Basel)*, 2022. **13**(10) DOI: 10.3390/mi13101575.
12. Wu, C.-A., et al., *Optimization of Computed Tomography Angiography Protocols for Follow-Up Type B Aortic Dissection Patients by Using 3D Printed Model*. *Applied Sciences*, 2021. **11**(15) DOI: 10.3390/app11156844.
13. Tino, R., et al., *A Systematic Review on 3D-Printed Imaging and Dosimetry Phantoms in Radiation Therapy*. *Technol Cancer Res Treat*, 2019. **18**: p. 1533033819870208 DOI: 10.1177/1533033819870208.
14. Filippou, V. and C. Tsoumpas, *Recent advances on the development of phantoms using 3D printing for imaging with CT, MRI, PET, SPECT, and ultrasound*. *Med Phys*, 2018. **45**(9): p. e740-60 DOI: 10.1002/mp.13058.
15. Ma, X., et al., *Classification of X-Ray Attenuation Properties of Additive Manufacturing and 3D Printing Materials Using Computed Tomography From 70 to 140 kVp*. *Front Bioeng Biotechnol*, 2021. **9**: p. 763960 DOI: 10.3389/fbioe.2021.763960.
16. NIST. *National Institute of Standards and Technology - U.S. Department of Commerce*. 02.02.2025]; Available from: <https://www.nist.gov/>.

17. NIST. *What are Imaging Phantoms?* 02.02.2025]; Available from: <https://www.nist.gov/physics/what-are-imaging-phantoms>.
18. DeWerd, L.A. and M. Kissick, *The Phantoms of Medical and Health Physics - Devices for Research and Development*. 2014: Springer DOI: 10.1007/978-1-4614-8304-5.
19. Radiology, T.A.C.o. *The American College of Radiology*. 02.02.2025]; Available from: <https://www.acr.org/>.
20. NIST. *NIST MRI Phantom*. 03.02.2025]; Available from: <https://www.nist.gov/programs-projects/quantitative-mri>.
21. phantomlab. *Magphan® 128 Distortion Phantom TDS*. 03.02.2025]; Available from: <https://www.phantomlab.com/magphan-adni>.
22. SNMMI. *Society of Nuclear Medicine & Molecular Imaging*. 03.02.2025]; Available from: <https://snmmi.org/Web/SNMMI-Home.aspx>.
23. Paul Segars, W. and B.M. Tsui, *MCAT to XCAT: The Evolution of 4-D Computerized Phantoms for Imaging Research: Computer models that take account of body movements promise to provide evaluation and improvement of medical imaging devices and technology*. Proc IEEE Inst Electr Electron Eng, 2009. **97**(12): p. 1954-1968 DOI: 10.1109/JPROC.2009.2022417.
24. Company, C.-M.M. *Jaszczak SPECT Phantom*. 03.02.2025]; Available from: <https://www.mirion.com/products/medical/nuclear-medicine-instrumentation/quality-assurance/phantoms/jaszczak-spect-phantom>.
25. Company, C.-M.M. *NEMA IEC PET Body Phantom Set™*. 03.02.2025]; Available from: <https://www.mirion.com/products/medical/nuclear-medicine-instrumentation/quality-assurance/phantoms/nema-iec-pet-body-phantom-set>.
26. Oates, C., *Ultrasound Technology for Clinical Practitioner*. 2023: Wiley DOI: 10.1002/9781119891581.
27. Leeds. *Leeds Test Objects*. 03.02.2025]; Available from: <https://leedstestobjects.com/>.
28. Objects, L.T. *TOR CDR Phantom*. 03.02.2025]; Available from: <https://leedstestobjects.com/index.php/phantom/tor-cdr/>.
29. Rodriguez Perez, S., et al., *Characterization and validation of the thorax phantom Lungman for dose assessment in chest radiography optimization studies*. J Med Imaging (Bellingham), 2018. **5**(1): p. 013504 DOI: 10.1117/1.JMI.5.1.013504.
30. phantomlab. *Catphan Phantom*. 03.02.2025]; Available from: <https://www.phantomlab.com/catphan-phantoms>.
31. RSD - Radiology Support Devices, I. *Alderson Radiation Therapy Phantom*. 03.02.2025]; Available from: <https://rsdphantoms.com/product/the-alderson-radiation-therapy-phantom/>.
32. Company, S.N.-M.M. *Motion Management QA Phantoms*. 03.02.2025]; Available from: <https://www.sunnuclear.com/products/motion-management-phantoms>.
33. *Core Radiology: A Visual Approach to Diagnostic Imaging*. 2 ed. 2021, Cambridge: Cambridge University Press DOI: DOI: 10.1017/9781108966450.
34. Cruz-Bastida, J.P., et al., *Modified ideal observer model (MIOM) for high-contrast and high-spatial resolution CT imaging tasks*. Med Phys, 2017. **44**(9): p. 4496-4505 DOI: 10.1002/mp.12404.

35. Debra M. Ikeda, K.K.M., *Breast Imaging The Requisites 1*. 2nd ed.: Elsevier.
36. Niknejad M, I.M., Murphy A, et al. *Mammography views*. 28 Jan 2025]; Reference article]. Available from: <https://radiopaedia.org/articles/15023>.
37. F, G., *Spiculated breast cancer, Case study*. Radiopaedia.org.
38. M, H., *Homogeneously dense breast tissue. Case study*. Radiopaedia.org.
39. RMK, M.A., et al., *Radiation dose from digital breast tomosynthesis screening - A comparison with full field digital mammography*. J Med Imaging Radiat Sci, 2020. **51**(4): p. 599-603 DOI: 10.1016/j.jmir.2020.08.018.
40. Jochelson, M.S., et al., *Bilateral contrast-enhanced dual-energy digital mammography: feasibility and comparison with conventional digital mammography and MR imaging in women with known breast carcinoma*. Radiology, 2013. **266**(3): p. 743-51 DOI: 10.1148/radiol.12121084.
41. Tollens, F., et al., *Cost-Effectiveness of MR-Mammography in Breast Cancer Screening of Women With Extremely Dense Breasts After Two Rounds of Screening*. Front Oncol, 2021. **11**: p. 724543 DOI: 10.3389/fonc.2021.724543.
42. Skaane, P., et al., *Comparison of digital mammography alone and digital mammography plus tomosynthesis in a population-based screening program*. Radiology, 2013. **267**(1): p. 47-56 DOI: 10.1148/radiol.12121373.
43. Radiology, T.A.C.o. *The Accreditation Process: Mammography*. 02.02.2025]; Available from: <https://accreditationsupport.acr.org/support/solutions/articles/11000070547-the-accreditation-process-mammography>.
44. Nuclear, S. *Model 020 BR3D Breast Imaging Phantom UG* 03.02.2025]; Available from: <https://support.sunnuclear.com/r/b867c8fd-3c88-45cb-a8c2-60e86eb85b9b>.
45. Brunner, C.C., et al. *Evaluation of Various Mammography Phantoms for Image Quality Assessment in Digital Breast Tomosynthesis*. in *Breast Imaging*. 2012. Berlin, Heidelberg: Springer Berlin Heidelberg.
46. phantomlab. *Tomophan DBT Phantom*. 03.02.2025]; Available from: <https://www.phantomlab.com/tomophan-phantom>.
47. Nuclear, S. *CESM Phantom Model 022*. 03.02.2025]; Available from: <https://www.sunnuclear.com/products/contrast-enhanced-spectral-mammography-phantom>.
48. Varallo, A., et al., *Fabrication of 3D printed patient-derived anthropomorphic breast phantoms for mammography and digital breast tomosynthesis: Imaging assessment with clinical X-ray spectra*. Phys Med, 2022. **98**: p. 88-97 DOI: 10.1016/j.ejmp.2022.04.006.
49. B.V., U. *UltimakerS3*. 02.02.2025]; Available from: <https://ultimaker.com/de/3d-printers/s-series/ultimaker-s3/>.
50. Michel, E. *beta metric*. 2025 03.02.2025]; Available from: <https://www.mathworks.com/matlabcentral/fileexchange/57420-beta-metric>.
51. Rossman, A.H., et al., *Three-dimensionally-printed anthropomorphic physical phantom for mammography and digital breast tomosynthesis with custom materials, lesions, and*

uniform quality control region. J Med Imaging (Bellingham), 2019. **6**(2): p. 021604 DOI: 10.1117/1.JMI.6.2.021604.

52. Schopphoven, S., et al., *Breast phantoms for 2D digital mammography with realistic anatomical structures and attenuation characteristics based on clinical images using 3D printing*. Phys Med Biol, 2019. **64**(21): p. 215005 DOI: 10.1088/1361-6560/ab3f6a.
53. Irnstorfer, N., et al., *An anthropomorphic phantom representing a prematurely born neonate for digital x-ray imaging using 3D printing: Proof of concept and comparison of image quality from different systems*. Sci Rep, 2019. **9**(1): p. 14357 DOI: 10.1038/s41598-019-50925-3.
54. Cockmartin, L., et al., *Design and application of a structured phantom for detection performance comparison between breast tomosynthesis and digital mammography*. Phys Med Biol, 2017. **62**(3): p. 758-780 DOI: 10.1088/1361-6560/aa5407.
55. Salomon, E., et al., *Technical note: Realization and uncertainty analysis for an adjustable 3D structured breast phantom in digital breast tomosynthesis*. Med Phys, 2023. **50**(8): p. 4816-4824 DOI: 10.1002/mp.16600.
56. Ivanov, D., et al., *Suitability of low density materials for 3D printing of physical breast phantoms*. Phys Med Biol, 2018. **63**(17): p. 175020 DOI: 10.1088/1361-6560/aad315.
57. Mettivier, G., et al., *Attenuation coefficient in the energy range 14-36 keV of 3D printing materials for physical breast phantoms*. Phys Med Biol, 2022. **67**(17) DOI: 10.1088/1361-6560/ac8966.
58. Boone, J.M., *Glandular Breast Dose for Monoenergetic and High-Energy X-ray Beams: Monte Carlo Assessement*. Radiology, 1999. **213**: p. 23-37.
59. Baneva, Y., et al., *Evaluation of a breast software model for 2D and 3D X-ray imaging studies of the breast*. Phys Med, 2017. **41**: p. 78-86 DOI: 10.1016/j.ejmp.2017.04.024.
60. Kontos, D., et al., *A new, open-source, multi-modality digital breast phantom*, in *Medical Imaging 2016: Physics of Medical Imaging*. 2016.
61. Bliznakova, K., et al., *BreastSimulator: A software platform for breast x-ray imaging research*. Journal of Biomedical Graphics and Computing, 2012. **2**(1) DOI: 10.5430/jbgc.v2n1p1.
62. Mettivier, G., et al., *Evaluation of the BreastSimulator software platform for breast tomography*. Phys Med Biol, 2017. **62**(16): p. 6446-6466 DOI: 10.1088/1361-6560/aa6ca3.
63. Elangovan, P., et al., *Design and validation of realistic breast models for use in multiple alternative forced choice virtual clinical trials*. Phys Med Biol, 2017. **62**(7): p. 2778-2794 DOI: 10.1088/1361-6560/aa622c.
64. NCCPM, N.C.-o.C.f.t.P.o.M.-. *OPTIMAM project*. 2011; Available from: <https://medphys.royalsurrey.nhs.uk/nccpm/>.
65. Zhengzhou ChaoKuo Electronic Technology Co., L. *FLSUN 3D Printers*. 02.02.2025]; Available from: <https://flsun3dprinter.en.ec21.com/>.
66. Europe, F. *V400*. 02.02.2025]; Available from: <https://eu.store.flsun3d.com/products/flsun-v400>.
67. Dance, D.R. and I. Sechopoulos, *Dosimetry in x-ray-based breast imaging*. Phys Med Biol, 2016. **61**(19): p. R271-R304 DOI: 10.1088/0031-9155/61/19/R271.

68. Cancer, I.-I.A.f.R.o. *Atlas of breast cancer early detection*. 02.02.2025]; Available from: https://screening.iarc.fr/atlasbreastdetail.php?Index=087&e=&utm_so.
69. ICRU - International Commission on Radiation Units and Measurements, I., *ICRU Report 46, Photon, Electron, Proton and Neutron Interaction Data for Body Tissues*.
70. Elegoo. *Saturn 4 Ultra*. 02.02.2025]; Available from: <https://eu.elegoo.com/de-at/products/saturn-4-ultra-12k-10inch-monochrome-lcd-resin-3d-printer>.
71. CBD-Tech. *Chitubox*. 02.02.2025]; Available from: <https://www.chitubox.com/en/index>.
72. Shenzhen Getech Technology Co., L. *PLA Transparent by Geeetech*. 02.02.2025]; Available from: <https://www.geeetech.com/3d-printer-supplies-filament-reprap-pla-1kgroll-transparency-p-1085.html>.
73. B.V., U. *Ultimaker PLA TDS*. 02.02.2025]; Available from: <https://um-support-files.ultimaker.com/materials/2.85mm/tds/PLA/Ultimaker-PLA-TDS-v5.00.pdf>.
74. FormFutura. *FormFutura HDglass TDS*. 02.02.2025]; Available from: <https://formfutura.com/datasheets/formfutura-tds-hdglass.pdf>.
75. FormFutura. *Easyfil ABS*. 05.02.2025]; Available from: <https://formfutura.com/datasheets/formfutura-tds-easyfilabs.pdf>.
76. Elegoo. *ABS-like Resin V3.0*. 02.02.2025]; Available from: <https://eu.elegoo.com/products/abs-like-resin-v3-0-colored-1kg-2kg?variant=47962804388116>.
77. PHROZEN TECH CO., L. *TR250LV High Temp 3D Printing Resin*. 02.02.2025]; Available from: <https://phrozen3d.com/products/tr250lv-high-temp-resin>.
78. Chemistry, C.C. *CAS RN: 8002-74-2 Hydrocarbon waxes chemical properties*. 02.02.2025]; Available from: https://commonchemistry.cas.org/detail?cas_rn=8002-74-2.
79. X3msnake. *Validation Matrix* 02.02.2025]; Available from: <http://thingiverse.com/thing:4707289>.
80. JetBrains. *PyCharm (Version 2023.2.1) [Computer software]*. 2025 05.02.2025]; Available from: <https://www.jetbrains.com/de-de/pycharm/>.
81. OpenAI. *ChatGPT (Feb 5 version) [Large language model]*. 2025 05.02.2025]; Available from: <https://chat.openai.com/>.
82. PineTools. *Split Image*. 02.02.2025]; Available from: <https://pinetools.com/split-image>.
83. Ltd, M. *microDicom*. 05.02.2025]; Available from: <https://www.microdicom.com/>.
84. colorfabb. *colorfabb_HT clear*. 05.02.2025]; Available from: <https://colorfabb.com/ht-clear>.